Master of Science Thesis

Semi-Analytical Modelling of VAT Laminates with Cut-Outs

Behaviour of Discontinuous Variable Stiffness Laminates Using Enriched Rayleigh-Ritz Method

T. A. Janssens

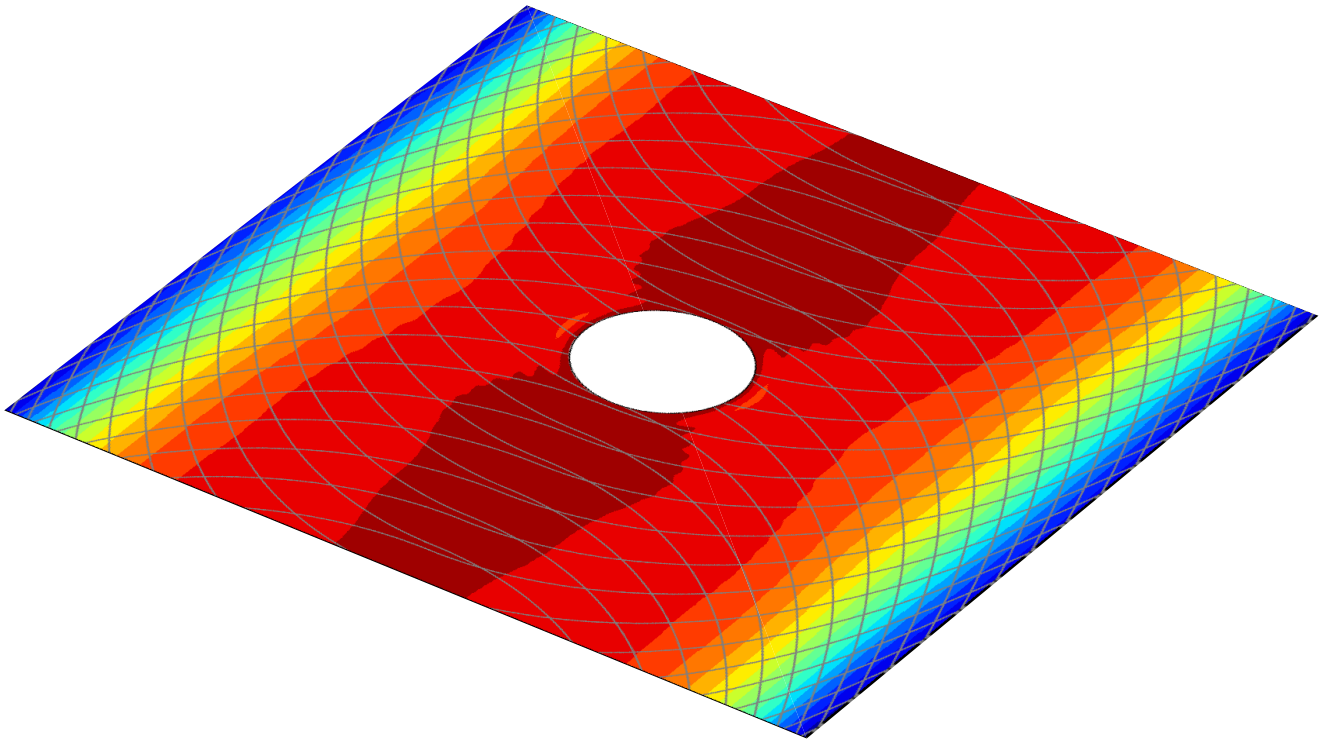

Faculty of Aerospace Engineering · Delft University of Technology

TU Delft Delft University of Technology

Semi-Analytical Modelling of VAT Laminates with Cut-Outs

Behaviour of Discontinuous Variable Stiffness Laminates Using Enriched Rayleigh-Ritz Method

Master of Science Thesis

For obtaining the degree of Master of Science in Aerospace Engineering
at Delft University of Technology

T. A. Janssens

7^{th} February 2020

Faculty of Aerospace Engineering · Delft University of Technology

Delft University of Technology
Faculty of Aerospace Engineering
Department of Aerospace Structures and Materials

GRADUATION COMMITTEE

Dated: 7^{th} February 2020

Chair holder:

Prof. Dr. Christos Kassapoglou

Committee members:

Dr.-Ing. Saullo G. P. Castro

Dr. Calvin Rans

Abstract

Using Variable Angle Tow (VAT) laminates, the stiffness and strength properties of laminates can be continuously varied to arrive at designs that outperform traditional straight fibre composite laminates in cases where the loads are distributed in a non-uniform manner. Cases of particular interest are laminates under buckling conditions or laminates containing cut-outs, for which VAT laminates have the ability to decrease concentration factors and increase buckling loads, thus having the ability to create more efficient designs.

With the aim of finding closed-form solutions or solutions with reduced computational cost, a semi-analytical analysis tool is developed which is able to determine the behaviour of VAT laminates with cut-outs. The method is based on finding the position of minimum energy using the Rayleigh-Ritz method. Due to the discontinuous nature of laminates with a cut-out, the approximation functions are enriched with additional functions to capture the behaviour near this discontinuity. In order to determine the energy functional derivatives across the domain of the laminate, Gauss-Legendre Quadrature numerical integration rules are applied to both rectangular and circular sections and the resultant energies are obtained by subtracting the integration on the cut-out domain from the rectangular domain. The approach mixes a stress-based approach to determine the in-plane pre-buckling stresses, and a displacement-based formulation to determine the buckling modes and eigenvalues. Minimising the energies yields the coefficients for the enriched stress-state and enriched displacement field. The model is set-up for balanced and symmetric laminates, thus decoupling the out-of-plane and in-plane behaviours. These components are verified with existing models in the literature and FE solutions, determining the behaviour of pristine VAT laminates and isotropic plates with cut-outs.

Upon successful verification, the components are combined to give the buckling behaviour. Furthermore, results from literature for a laminate including a square stiffening insert are used to verify the capabilities of the proposed model. These results have been extended further to circular stiffening insert to verify the capabilities of the proposed enriching trial functions.

Finally, a VAT laminate design is analysed where the capabilities of the proposed model, the proposed trial functions and VAT laminate designs are illustrated. For this case, the pre-buckling stresses and subsequent buckling behaviour are analysed for a VAT laminate with

a cut-out. The results are shown to be accurate in determining the axial load distribution and showed a decrease in stress concentrations surrounding the cut-out. This pre-buckling stress-state is used to determine the buckling behaviour and compared to the VAT laminate without cut-out.

Table of Contents

List of Figures

List of Tables

List of Abbreviations

VAT	Variable Angle Tow
TPE	Total Potential Energy
TCE	Total Complementary Energy
CLT	Classical Lamination Theory
FE/FEM	Finite Element / Finite Element Method
ERR	Enriched Rayleigh-Ritz
RHS	Right-Hand-Side
LHS	Left-Hand-Side

Acknowledgments

Firstly, I would like to thank my supervisor Dr.-Ing. Saullo Castro for his help, patience, understanding and advice. It has been a real pleasure to work with him and I enjoyed our meetings and conversations in which we would talk about the thesis, life in general and all opportunities that lie before me. With hindsight, it is a very fond memory where every time I would confront Saullo with a new problem in the thesis, his response would always be: "Oh, that's very interesting".

I must also thank Laura, who has helped me with all non-technical aspects of this thesis. My workplace and working conditions the past year have been very pleasant and I have her to thank for all this.

I would also like to thank all my friends and fellow students who made my long journey in Delft great:
Casper for all the sarcastic comments, coffee breaks, assignment brainstorm sessions and letting me make fun of your beard.
My officemates Eva, Stefano, Iñigo and Philip for the fun and motivating atmosphere we enjoyed in the office. Especially Stefano for teaching me how to truly enjoy coffee: "If it doesn't burn on the tongue, it isn't coffee".
My close friends and housemates, Dirk, Bob, Tom, Matthijs, Marijn, Eloy, Thomas, Yuup, Joppe, Thijs, Jan, Dimitri, Jort and Martijn. Thanks for all the good times, pizza lunches, coffee breaks, long dinners and beers. Thank you for giving me motivation and believing in me when I needed it. Most important of all, thank you for all the fun and laughter.

I would also like to thank my high-school maths teacher, Albert Peterse. During a period where I was failing maths badly at age 13, he did not give up and really went out of his way to help me. I hope this thesis proves his efforts inspire me to this day.

The past few months have been tough and have proven once more that family is the most important thing in life. It is without a doubt that I would be nowhere without them. I would like to thank my parents for supporting me emotionally, physically and, not unimportantly, financially to strive for the best. They allowed me to explore the world for myself, allowing me to make mistakes and were there for me when I inevitably did. I cannot thank you enough. I must also thank my brother Christopher who is always there for me. As a younger brother, it has certainly helped me to have a big brother set an example growing up, even at times where he was a bad example...

Finally, I would like to thank my girlfriend Daphne. When we first met, I was trying to find my way. With your help, I have found the path which has led to this thesis. Your love and support has motivated and guided me more than you know. The accomplishment of this thesis, and likely many more accomplishments to follow, I owe to you. Thank you so much.

Delft, University of Technology T. A. Janssens
7^{th} February 2020

In loving memory

Bart Janssens

⋆ *September 2, 2004* † *October 2, 2019*

Thank you for all the laughs, your positivity
and your mischievous look on life

Chapter 1

Introduction

The use of composite materials has become more widespread across the aerospace industry ever since one of the first applications on the Akaflieg Phöenix, a glider built in the late $1950's$. More recently, the Boeing Dreamliner became the first commercial aircraft where composite materials have been used for the primary structures such as the tail, wing and fuselage and composed of 50 weight% composite materials [1, 13].

It is well known that the use of fibre reinforced polymers, or composite materials, can yield structures with high strength/stiffness to weight ratios with respect to metallic structures. Plates made from these composite materials, referred to as laminates, are composed of multiple layers, or laminae, in which the fibre direction can be aligned in the directions where strength and stiffness are required. The laminate can be tailored to the design requirements. In traditional composites, this tailoring is done by varying the stacking and orientation of laminae for a laminate. This can be visualised in Fig. 1.2.

Restricting the design to straight fibres however, limits the potential of the fibre composite materials, for instance in cases where the stress distribution is not uniform. In such cases the strength and stiffness requirements may vary with the location on a single laminate. With a traditional layup design philosophy, the laminate will contain stiffness and strength even at locations where it might not be needed, i.e. additional unnecessary weight.

Varying the fibre orientation within a single ply will allow the designer to use even more of the potential provided by fibre composite materials. This application of Variable Angle Tow (VAT) laminates, also known as variable stiffness laminates, thus broadens the design space, allowing the designer to achieve better designs for a given application. Producing such laminates or structures was limited however by manufacturing techniques in the past. With the introduction of automated fibre placement, or tow-placement machines, the practical limitations mostly disappeared and such designs could be implemented.

Cases where the stress distribution is non-uniform can be found in several cases. Plates undergoing out-of-plane deformations, or plates containing cut-outs are examples which are encountered frequently in real-life applications. Cut-outs are a common feature in aerospace structures, with examples such as windows, inspection holes and holes for wires/cables. These

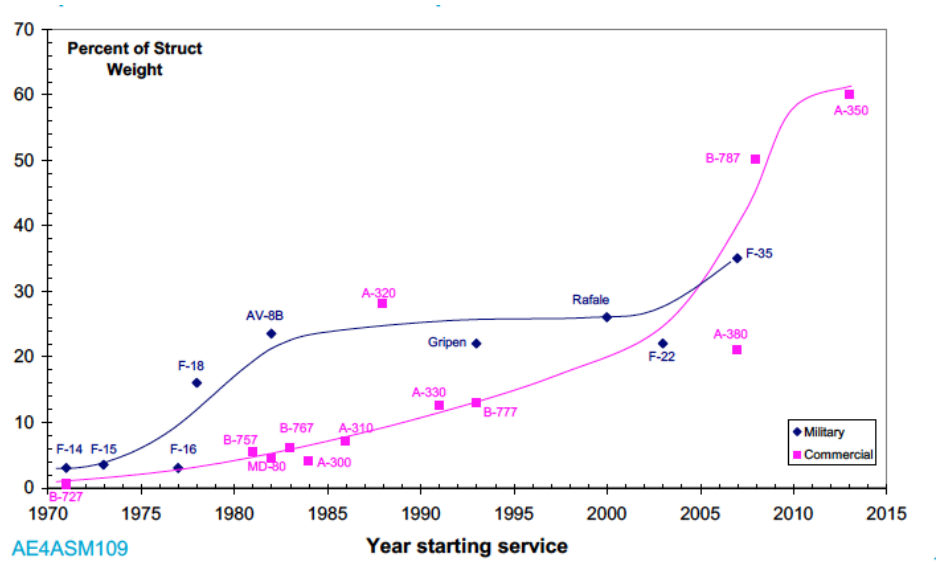

Figure 1.1: The increase in weight% of composite materials can be seen from this graph, image from [1].

cut-outs have an influence on the stress distribution in the structure, where the stresses will redistribute around a cut-out, leading to stress peaks around the cut-out and a general non-uniform stress distribution. When designing for a structure with a cut-out, it is of importance to know the effects of the presence, location and size of the cut-out. For traditional materials, e.g. metals such as aluminium, the effects of cut-outs have been studied for decades and are well understood. However, when analysing for structures with cut-outs, computationally and license-fee expensive finite element software is often used. Furthermore, while the behaviour for isotropic materials is well understood, the effects for composite materials are dependant on the specific layup used. When considering VAT laminates, with the fibre orientation varying throughout a single layer, the effects become more complicated again.

So, the effects of the cut-out location and size, and the added effect of using VAT laminates means that the design analysis becomes increasingly complex while also having an increased design space. While cut-outs are such a common feature of aerospace structures, having an efficient model to determine the effects of cut-outs is necessary. Such a method will save valuable time in the design process when trying to obtain a solution close to the optimum. This will lead to many benefits, such as lower development/design costs, lighter/more efficient designs, weight and subsequent fuel savings during the lifetime and overall reduction of the CO_2 emissions of aircraft.

The research question for this work is thus formulated:

Can an efficient model be developed to predict the mechanical behaviour of (VAT) laminates containing discontinuities such as cut-outs?

In the following chapters, a semi-analytical model is developed by analysing methods described by previous authors to develop a new model which is able to describe the structural behaviour of VAT laminates including cut-outs under in-plane loads, out-of-plane loads and stability

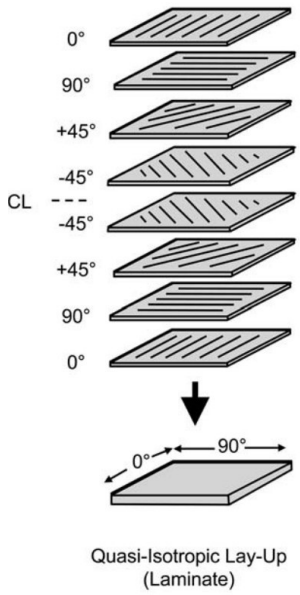

Figure 1.2: Multiple lamina of different fibre orientations make up a laminate.

behaviour such as buckling. In this work, the model is developed by setting up the analytical formulation for the Total Potential Energy (TPE) and Total Complementary Energy (TCE), mixing stress-based and displacement based approaches, and using a numerical approach to apply this formulation to a plate containing a cut-out. The Rayleigh-Ritz method is chosen to find the behaviour, where the assumed solutions are enriched with additional solution sets to capture the behaviour caused by the discontinuities e.g. the cut-out.

The set-up of the thesis is as such, first in Chapter 2 the work done by former authors will be reviewed where analytical, numerical and experimental approaches have been applied to VAT laminates or laminates with discontinuities such as cut-outs. In Chapter 3, a review of the Classical Lamination Theory (CLT) is given and the expressions for the TPE and TCE are derived. The Enriched Rayleigh-Ritz method and the numerical integration techniques are discussed in Chapter 3. In Chapter 4, the theory from Chapter 3 is applied for Out-of-Plane deflection load cases of plates and laminates when including a cut-out. In Chapter 5, the pre-buckling stress-state is determined using the TCE before determining the buckling behaviour in Chapter 6. In Chapter 7, the pre-buckling and buckling behaviours of a VAT laminate with a cut-out are determined to show the capabilities of the method developed in this thesis, as well as the increased potential of VAT laminates. In Chapter 8, some remarks are made with respect to the developed method and recommendations are made. Finally, in Chapter 9, concluding remarks are presented.

Chapter 2

Literature Study

This chapter presents an introduction into the relevant subjects for this thesis. Past work done regarding variable stiffness laminates is introduced in Section 2.1, as well as the various ways to obtain a variable stiffness laminate, i.e. discrete or continuously varying stiffness. Furthermore, work related to the analysis of laminates with cut-outs or other discontinuities is discussed in Section 2.2.

2.1 Variable Stiffness Laminates

In the early $90's$ the principle of variable stiffness was introduced. Around this time several authors published papers regarding the topic of variable stiffness laminates. To the author's knowledge, the first known reference of variable stiffness laminates was by Leissa & Martin in 1990, where the authors provided insight into advantages that could be obtained using variable stiffness designs [14]. Subsequently, in 1993, Biggers & Srinivasan presented work where a variable stiffness design is obtained by adding more unidirectional layers locally to influence the stiffness [2], shown in Fig. 2.1. Using this local stiffness increase, a buckling load increase of over 100% for thin laminates was achieved. This confirmed that increasing the stiffness near the edges of a laminate will increase the buckling load. This result is in line with the expectation, as the load tends to shift towards the edges of the laminate upon buckling. In work done by Gürdal & Olmedo, variable stiffness designs are based on the concept of fibre steering, or VAT, where the fibre orientation is allowed to change in a single lamina. The fibre angle is defined according a fibre path definition, which is discussed in more detail later. The authors used the Classical Lamination Theory to arrive at the differential equations for the laminate problem expression, thus using the ABD matrix coefficients. These coefficients are no longer constant for a VAT laminate however, but using the fibre path definitions can be expressed as a functions of the (x, y) position on the laminate. The differential equation problem was then solved using a software package called ELLPACK. The fibre path definition, touched upon earlier, is a definition of the angle of the fibre based on the (x, y) location on the laminate. In the work done by Gürdal & Olmedo, a linearly varying definition is used

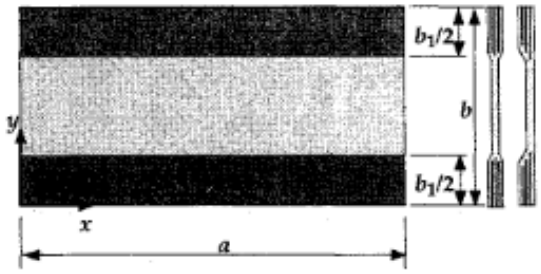

Figure 2.1: Layup of the laminate as presented by Biggers & Srinivasan [2].

with respect to the x-location, as shown in Eq. 2.1. In this expression, T_0 is the angle at the midpoint of the laminate and T_1 the angle at the ends of the laminate. For example, the case where $T_0 = 45°$ and $T_1 = 0°$ will yield a fibre path presented in Fig. 2.2.

$$\theta(x) = \frac{2(T_1 - T_0)}{a}x + T_0 \tag{2.1}$$

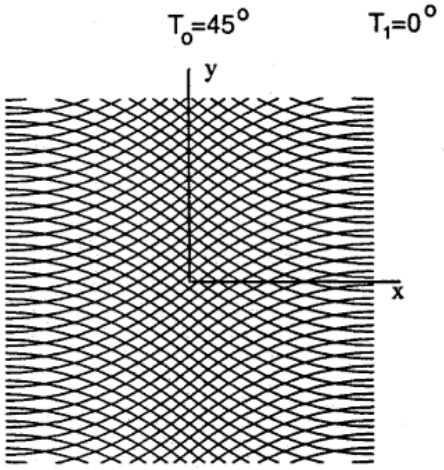

Figure 2.2: Fibre path for $T_0 = 45°$ and $T_1 = 0°$, using Eq. 2.1, image from [3]

As mentioned before, the laminate properties for VAT laminates are no longer constant across the laminate domain. As an example, in Fig. 2.3, the longitudinal stiffness is shown for the example laminate from Fig. 2.2.

In studies performed by Wu et al. [9], and later adopted by Guimaraes et al. [4] and Quadros and Hernandes [15], the fibre angle is defined according to Lagrange polynomials, shown in Eq. 2.2 where Φ_i is the ply reference angle and T_{mn} are the control angles in the reference points, as shown in Fig. 2.4 [4, 9, 15]. This non-linear fibre variation allows for more variations of the fibre path. In the study by Wu et al. [9], the authors state that that the number and position of the reference points T_{mn} can be arbitrary, but proper choices will accelerate the optimisation process and avoid possible entrapment in local minima. Moreover, the choice on the references points depends on the plate geometry, boundary conditions and applied

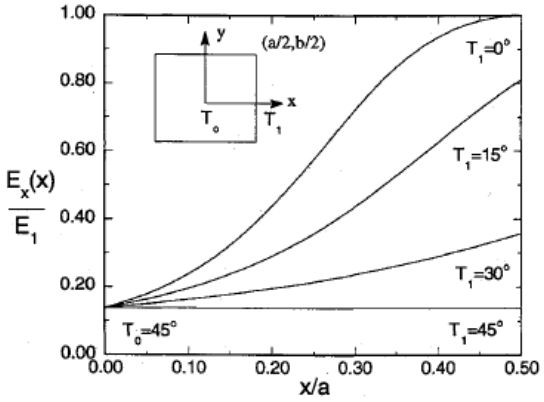

Figure 2.3: Normalised E_x modulus as a function of x/a for varying values of T_1, image from [3].

loadings. Finally, if the fibre angle is only allowed to vary along the x-axis, and only two reference points are used ($x = 0$, $x = a/2$) the expression reduces to the linear expression in Eq. 2.1 [9].

$$\theta(x, y) = \Phi_i + \sum_{m=0}^{M-1} \sum_{n=0}^{N-1} T_{mn} \prod_{m \neq i} \frac{x - x_i}{x_m - x_i} \prod_{n \neq j} \frac{y - y_j}{y_n - y_j} \tag{2.2}$$

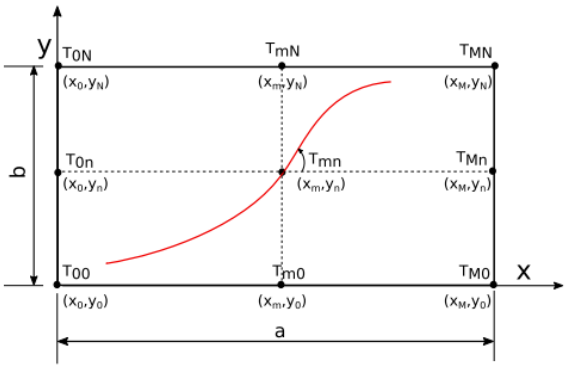

Figure 2.4: Fibre orientation according using Lagrange polynomials with reference points T_{mn}, image from [4]

In the aforementioned work by Wu et al. [9], the pre-buckling and buckling responses of VAT laminates are determined where the variable stiffness is obtained using to fibre path definitions as described above. The work consisted of using the Rayleigh-Ritz method to minimise the energy of the laminate, approximating the behaviour using trail functions adopted to adhere to the boundary conditions. The use of the Rayleigh-Ritz method combined with energy methods is discussed in more detail in Chapter 3. For the pre-buckling behaviour, or in-plane behaviour, the Airy stress formulation is used to reduce the amount of unknown from three expressions N_x, N_y and N_{xy} to one function. The Airy stress function is based on the thin-plate assumption, where the stresses through the thickness are considered constant,

thus $\partial/\partial z = 0$. Additionally, if no forces are exerted on the surface of the laminate, this assumption leads to the statement that $\tau_{xz} = \tau_{yz} = \sigma_z = 0$. Starting from the element equilibrium equations in Eq. 2.3, and integrating through the thickness yields the running loads N_x, N_y and N_{xy} $[force/distance]$, this will yield the updated equilibrium equations in Eq. 2.4.

$$\begin{aligned} \frac{\partial \sigma_x}{\partial x} + \frac{\partial \tau_{xy}}{\partial y} + \frac{\partial \tau_{xz}}{\partial z} &= 0 \\ \frac{\partial \tau_{xy}}{\partial x} + \frac{\partial \sigma_y}{\partial y} + \frac{\partial \tau_{yz}}{\partial z} &= 0 \\ \frac{\partial \tau_{xz}}{\partial z} + \frac{\partial \tau_{yz}}{\partial y} + \frac{\partial \sigma_z}{\partial z} &= 0 \end{aligned} \tag{2.3}$$

$$\begin{aligned} \frac{\partial N_x}{\partial x} + \frac{\partial N_{xy}}{\partial y} &= 0 \\ \frac{\partial N_{xy}}{\partial x} + \frac{\partial N_y}{\partial y} &= 0 \end{aligned} \tag{2.4}$$

The Airy stress function is one function, coupling the in-plane loads N_x, N_y and N_{xy} while adhering to the equilibrium in Eq. 2.4. The in-plane loads in terms of the Airy stress function Φ is defined in Eq. 2.5

$$N_x = \frac{\partial^2 \phi}{\partial y^2} \qquad N_y = \frac{\partial^2 \phi}{\partial x^2} \qquad N_{xy} = -\frac{\partial^2 \phi}{\partial x \partial y} \tag{2.5}$$

Using the energy method, the in-plane, out-of-plane and buckling behaviour are determined. However, as the laminate stiffness parameters are not constant due to the variable stiffness properties, solving the energy integrals over the domain of the laminate becomes more complicated. For this purpose, in the work by Wu et al., the integration is no longer performed analytically, but using a numerical integration scheme using Legendre polynomials [9]. This numerical integration scheme is explained in more detail in Section 3.3.2. The trial functions used are Legendre polynomials multiplied with a boundary condition forcing function to make sure the solution complies with the boundary conditions. The domain of the laminate is transformed from the Cartesian coordinates expressed in (x, y) to the natural coordinates (ξ, η). In this natural coordinate system, the laminate is transformed to have dimensions $\xi = [-1; 1], \eta = [-1; 1]$. The boundary conditions forcing function, $g(\xi, \eta)$ can be defined as in Eq. 2.6, with the coefficient k dependant on the boundary conditions. In terms of deflections, if $k_{i/j} = 0$, it implies the respective edge is free, when $k_{i/j} = 1$ edge will be simply supported and when $k_{i/j} = 2$ the edge will be clamped.

$$g(\xi, \eta) = (1 - \xi^2)^{k_i} \cdot (1 - \eta^2)^{k_j} \tag{2.6}$$

Another approach when designing for variable stiffness is the use of lamination parameters, as used by Setoodeh, Abdalla & Gürdal [16]. The lamination parameters are a different method of representing the stiffness properties in the classical lamination theory, and reduce the design variables considerably. The **A** matrix, containing nine coefficients, can be represented using

four lamination parameters. This approach will yield an optimum distribution in terms of these lamination parameters. However, this does not translate to a unique layup or fibre orientation angle. A fibre path, or blended layup design consisting of straight fibre patches, must then be found to yield the stiffness properties corresponding to the lamination parameters distribution. While this is possible, it is not straightforward. The work by Setoodeh et al. [17] and Khani et al. [18] used this approach for the design, production and testing of a wing skin panel containing a cut-out. The results showed increased performance in strength and upon failure showed failure at multiple locations, indicating an overall more efficient design. Due to the complexity of obtaining a layup or fibre orientation design however, lamination parameters will not be used in this thesis work.

Besides the in-plane and buckling considerations discussed so far, the out-of-plane behaviour is also considered in the work by Alhajahmad et al. [19]. In this work, a solution is obtained based on an analytic formulation for the pressure pillowing problem. A VAT laminate with no discontinuities is considered and subjected to a normal distributed pressure force, such as in a pressurised fuselage. Alhajahmad et al. used the linear varying fibre path definitions as defined by Gürdal & Olmedo [3], besides also expanding to fibre path formulations based on Lobatto polynomials. Rather than using the Airy stress function, a formulation is based on the in plane displacements u, v and w, approximation functions were taken for all three displacements. As the problem here considers multiple unknowns in a single problem definition, three separate equilibrium equations are obtained. These three equations were reduced to a single non-linear equation by using the linearity of two of the equations. Using this approach, Alhajahmad was able to trace the equilibrium load deflection path and determine the unknown coefficients relating to the approximations for u, v and w.

2.2 Analyses Including Discontinuities

In the cases described above, the cases mostly referred to pristine laminates. In many cases, the analysis is focussed on buckling conditions, when the load distributions are no longer uniform over the laminate. Similarly, the load distribution in a plate is not uniform when the plate is no longer pristine, but contains a discontinuity such as a cut-out. Cut-outs are a very common feature in aerospace design, it is thus not a surprise that a lot of research is done on the subject. This topic was already briefly introduced in the work by Setoodeh et al. and Khani et al. where a wing skin panel with a cut-out was produced and tested [17, 18, 20].

The analysis for a composite plate when it contains a circular cut-out has been covered analytically in the past, such as the work by Lekhnitski in 1969 [21], where a complex domain formulation is used. The complex coordinate z is a function of the x and y locations, $z = x + iy$, and z becomes the main variable for the solution function. Furthermore, the solution procedure uses the Airy stress function to reduce the number of unknowns and introduces two coefficients describing the stiffness distribution of the laminate, the angularity and directionality. The angularity (a) and directionality (r) are shown in Eq. 2.7. These coefficients can not be considered constant for a VAT laminate. This, combined with other aspects in the analysis procedure yield that the method is not easily applicable for VAT laminates.

$$r = \sqrt{\frac{S_{22}}{S_{11}}} \qquad ; \qquad a = \frac{1}{2}\left(\frac{2S_{12} + S_{66}}{S_{11}}\right) \tag{2.7}$$

In work by Kassapoglou [5], energy methods combined with the Rayleigh-Ritz method are used to determine the in-plane stress field and buckling point of laminates with concentric layups, where a central located patch of the laminate consists of a different layup, as shown in Fig. 2.5. One of the special cases mentioned is where the concentric layup extends to the laminate edges, thus creating a case similar to that presented by Biggers & Srinivasan discussed earlier [5].

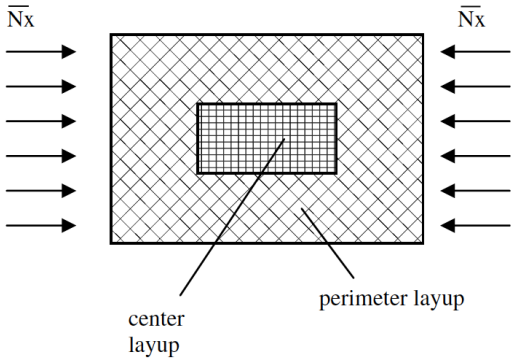

Figure 2.5: Illustration of the concentric layups. Image taken and adapted from [5].

The work by Kassapoglou considers the laminate under uniform compressive load at the edges, as can be seen from Fig. 2.5. Trial functions in the form of series solutions are input into the complementary energy equations and the energy is subsequently minimised to find the solution according to the Rayleigh-Ritz method. Rather than using the Airy stress function, three separate functions for N_x, N_y and N_{xy} are used, but each multiplied with a common unknown coefficient and set up thus that they comply with the equilibrium for thin plates, from Eq. 2.4. The trial functions used are shown in Eq. 2.8 [5].

$$\begin{aligned} N_x &= \overline{N_x} + \sum_{m=1}^{M}\sum_{n=1}^{N} H_{mn}\left\{cos(2m\pi\xi) - 1\right\} cos(2n\pi\eta) \\ N_y &= \frac{b^2}{a^2}\sum_{m=1}^{M}\sum_{n=1}^{N} \frac{m^2}{n^2} H_{mn} cos(2m\pi\xi)\left\{cos(2n\pi\eta) - 1\right\} \\ N_{xy} &= \frac{b}{a}\sum_{m=1}^{M}\sum_{n=1}^{N} \frac{m}{n} H_{mn} sin(2m\pi\xi) sin(2n\pi\eta) \end{aligned} \tag{2.8}$$

The trial functions in Eq. 2.8 are for a laminate under uniform compression load $\overline{N_x}$. As both the outer domain and the concentric domain consist of rectangular sections, Kassapoglou was able to set up analytic formulations for the energy integrals and solve for the in-plane loading. The results are shown in Fig. 2.6 for a laminate with a stiffer inner layup, plotting the normalised axial load from the center of the laminate towards the edge.

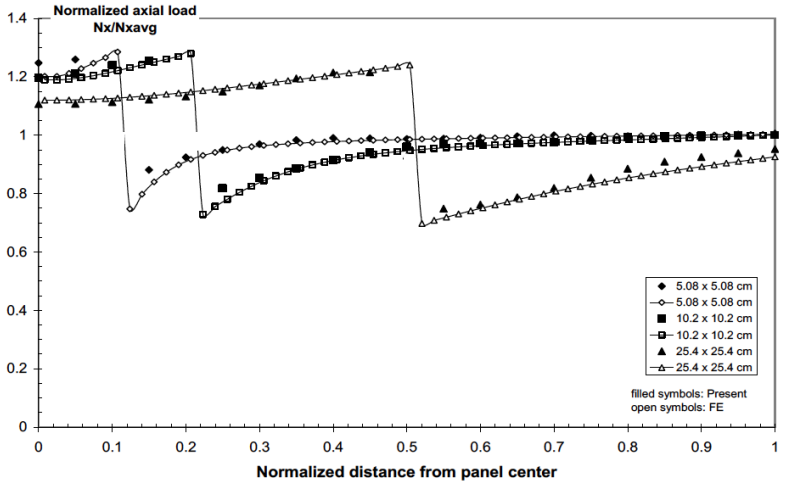

Figure 2.6: Axial load N_x from panel center outwards. Results and figure from [5].

It is also suggested by Kassapoglou that the center layup could consist of an empty layup, or cut-out effectively. In previous work by Papadopoulos & Kassapoglou where the laminate is loaded by shear, this is presented and buckling values are compared to those obtained with FEM software, seen in Fig. 2.7 [6].

In Fig. 2.7, the lines show matching behaviour, albeit with some discrepancies. When the

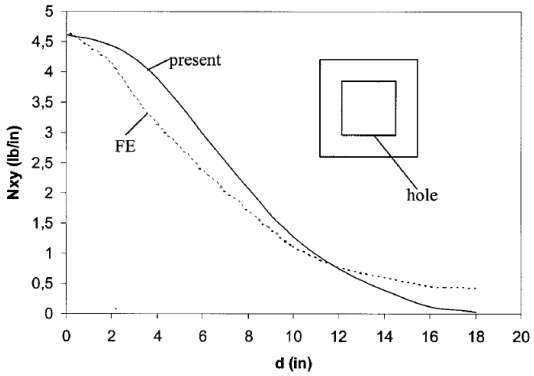

Figure 2.7: The buckling values for a constant stiffness laminate with a concentric cut-out, image from [6].

cut-out section increases, Papadopoulos & Kassapoglou explain the deviation is likely due to artificial stiffness of the Finite Element Method (FEM) elements close to the edges, as they are increasingly small. However, when the cut-out is smaller the error is accepted as the worst deviation is at 16%, but no explanation is given. A possible explanation could be that this deviation is due to the fact that the in-plane load distribution is no longer constant when the laminate contains a cut-out, while in the work by Papadopoulos it appears this assumption is made for simplicity in the calculations.

As the presence of a discontinuity such as a cut-out creates a load redistribution, variable stiffness designs are of high interest. One of the first approaches to improve a design for a laminate including a cut-out when subjected to in-plane loading was performed by Yau &

Chou [7]. Using an experimental approach, they inserted a metal pin into a woven fabric before curing the laminate, and as such moulded a hole into the material. This moulded hole showed fibres flowing around the hole, as can be seen in Fig. 2.8, yielding a continuously changing stiffness. In this study it was shown that the moulded hole specimens showed improved in-plane strength over drilled hole specimens. A difference can also be seen from the fracture of the specimens in Fig. 2.9. The improvement in strength can be seen in the bar charts in Fig. 2.10 for both epoxy and PEEK specimens with drilled and moulded holes.

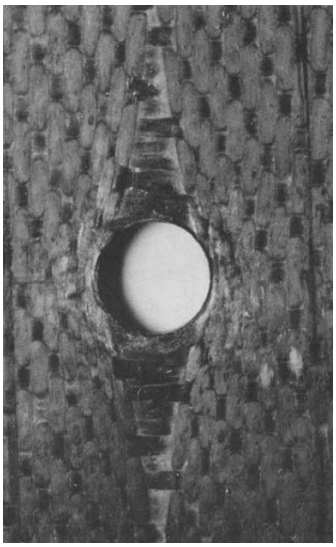

Figure 2.8: Moulded hole in fabric composite, image from [7].

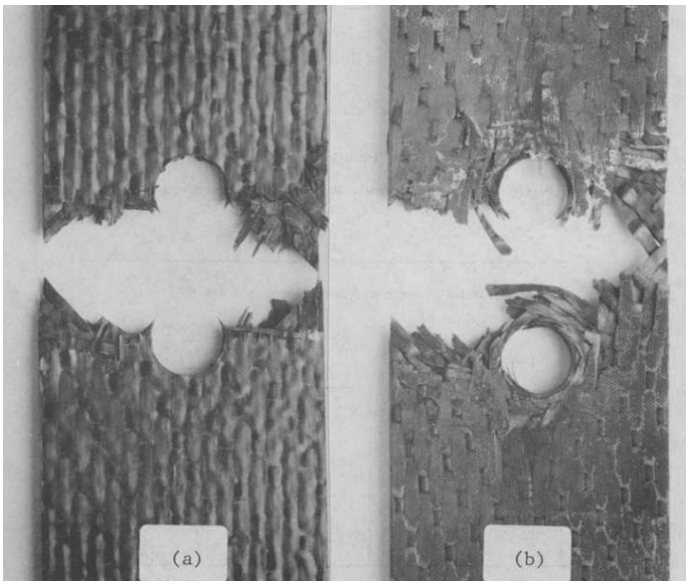

Figure 2.9: the fracture of specimen (a) composite specimen with drilled hole and (b) a moulded hole, image from [7].

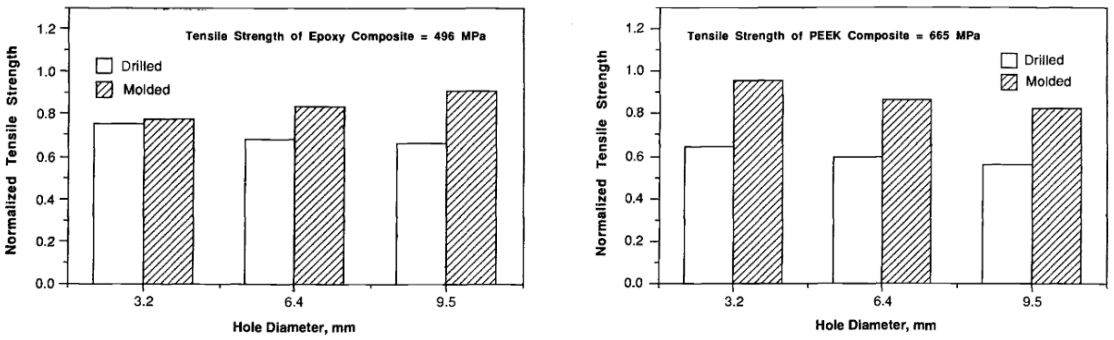

(a) Epoxy strength comparison

(b) Peek strength comparison

Figure 2.10: Strength comparison of epoxy and peek specimens moulded hole specimens w.r.t. drilled hole specimens, images from [7].

Rather than using an experimental approach, Hyer & Charette performed research into the fibre orientation around cut-outs using the finite element method and separating the domain around the hole into smaller discrete segments [22]. In each of the segments the principle stress directions were determined for an axial tension loading. The design goal was to have the fibres in each segment align with these principle stresses. In a follow up study, Hyer & Lee used a similar approach of dividing the domain into separate regions, with straight fibres within each region, but now optimised w.r.t. the buckling load [8]. These sections are represented as in Fig. 2.11a.

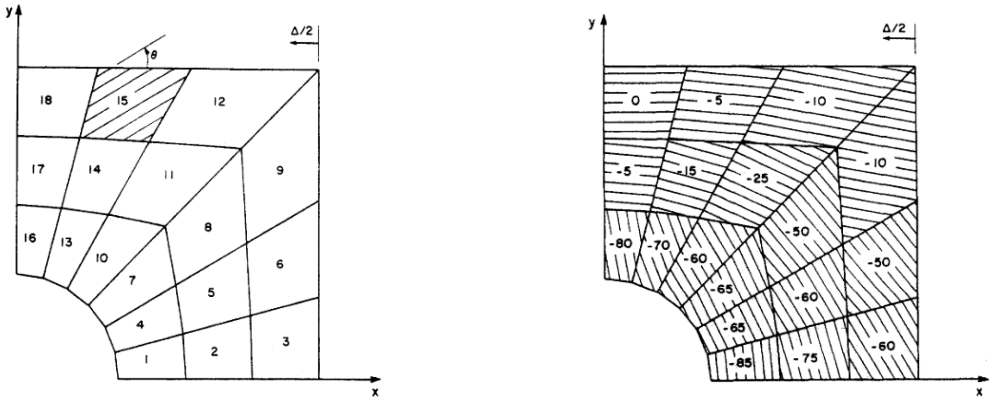

(a) **(b)**

Figure 2.11: Region definition and fibre orientations for an improvement in buckling, images from [8].

They found that several regions showed little sensitivity between fibre orientation and buckling load, and other regions showed high sensitivity. An example of the sensitivity plots showing low and high sensitivity can be found in Fig. 2.12. From these plots we can see the low sensitivity corresponds to the regions $1, 2, 3$, while the high sensitivity regions correspond to the regions $16, 17, 18$. Thus, the regions closer to the edge of the laminate have a larger influence on the buckling load than those along the center height of the laminate. This result thus agrees with that obtained by Biggers & Srinivasan [2]. Continuing the study, a gradient

search technique was used to determine the optimum fibre angle for each section to produce the best design. The angles found using this technique showed good agreement with the angles found in the sensitivity analysis, with the exception of the regions that showed little sensitivity. This can be explained by the low sensitivity of those regions, as the buckling load does not vary greatly with a change in angle, the gradient search technique has trouble finding a well defined minimum. The fibre orientations per region when optimised for buckling can be seen in Fig. 2.11b. Within these studies, no care is taken to account for the manufacture ability, as the fibre orientation difference of adjacent segments can be large. Such a layup would likely only be suitable for hand-layup techniques.

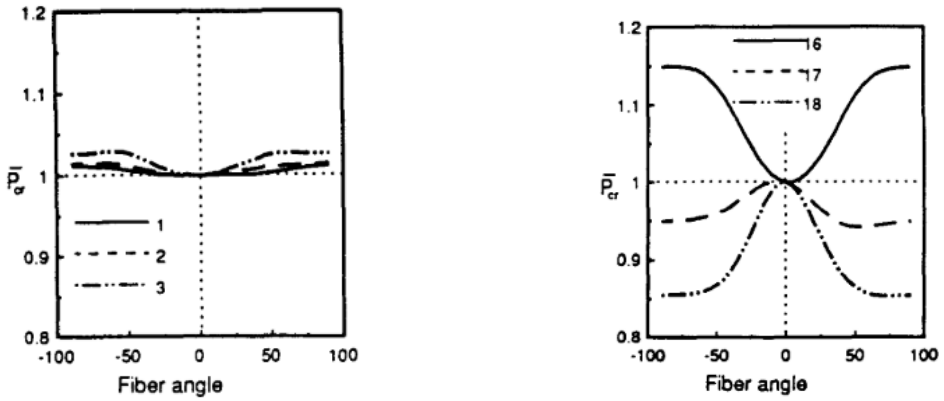

(a) **(b)**

Figure 2.12: Normalised buckling load vs fibre angle for regions (a) 1, 2, 3 and (b) 16, 17, 18, images from [8].

Chapter 3

Methodology

In this chapter, the methodology used for the development of the model is shown. First, in Section 3.1 the Classical Lamination Theory (CLT) is reviewed before deriving the governing equations using energy methods in Section 3.2, followed by the Rayleigh-Ritz solution method. Up to that point all equations are presented in their general formulation, e.g. without mention of discontinuities. Finally in Section 3.3, a cut-out is introduced and the Enriched Rayleigh-Ritz (ERR) and the numerical integration scheme are introduced in Sections 3.3.1 and 3.3.2.

3.1 Classical Lamination Theory

Composite materials are of an anisotropic nature, meaning that the stiffness in each direction can be different. In three dimensions, the engineering stresses and strains can be related through the generalised stress-strain relations for anisotropic materials, or Hooke's law. The coordinate system used in this section is shown in Fig. 3.1, where the x and y axis are aligned with the in-plane edges and the z is directed perpendicular out-of-plane to the plate surface, with zero at the plate midplane.

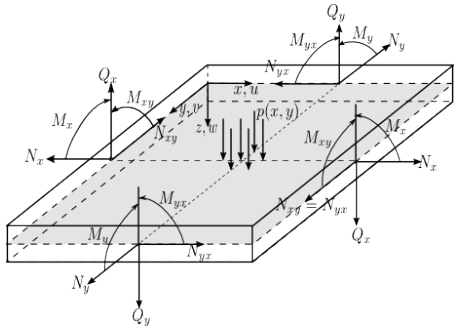

Figure 3.1: Resulting forces of a plate. Image from[1].

[1] https://en.wikiversity.org/wiki/User:Egm6936.s09/Curling_of_paper_sheet_using_shell_theory{#}Large_deformation_theory. Accessed on 6/11/2018

The general Hooke's law, shown in Eq. 3.1, shows all coefficients coupling all stresses and strains in the (x, y, z), or Cartesian, coordinates.

$$\begin{Bmatrix} \sigma_x \\ \sigma_y \\ \sigma_z \\ \tau_{yz} \\ \tau_{xz} \\ \tau_{xy} \end{Bmatrix} = \begin{bmatrix} E_{11} & E_{12} & E_{13} & E_{14} & E_{15} & E_{16} \\ E_{21} & E_{22} & E_{23} & E_{24} & E_{25} & E_{26} \\ E_{31} & E_{32} & E_{33} & E_{34} & E_{35} & E_{36} \\ E_{41} & E_{42} & E_{43} & E_{44} & E_{45} & E_{46} \\ E_{51} & E_{52} & E_{53} & E_{54} & E_{55} & E_{56} \\ E_{61} & E_{62} & E_{63} & E_{64} & E_{65} & E_{66} \end{bmatrix} \begin{Bmatrix} \epsilon_x \\ \epsilon_y \\ \epsilon_z \\ \gamma_{yz} \\ \gamma_{xz} \\ \gamma_{xy} \end{Bmatrix} \tag{3.1}$$

The elasticity tensor **E** from Eq. 3.1 is of a symmetric nature, i.e. $E_{ij} = E_{ji}$. Furthermore, when considering materials with two planes of symmetry, or orthotropic materials, the coupling terms between normal and shear stresses are zero, see Eq. 3.2.

$$E_{14} = E_{15} = E_{16} = E_{24} = E_{25} = E_{26} = E_{34} = E_{35} = E_{36} = 0 \tag{3.2}$$

Finally, for orthotropic bodies, shear stresses in one plane do not cause shear strains in the other planes.

$$E_{45} = E_{46} = E_{56} = 0 \tag{3.3}$$

The elasticity tensor **E**, simplified for orthotropic materials, then becomes:

$$\begin{Bmatrix} \sigma_x \\ \sigma_y \\ \sigma_z \\ \tau_{yz} \\ \tau_{xz} \\ \tau_{xy} \end{Bmatrix} = \begin{bmatrix} E_{11} & E_{12} & E_{13} & 0 & 0 & 0 \\ E_{21} & E_{22} & E_{23} & 0 & 0 & 0 \\ E_{31} & E_{32} & E_{33} & 0 & 0 & 0 \\ 0 & 0 & 0 & E_{44} & 0 & 0 \\ 0 & 0 & 0 & 0 & E_{55} & 0 \\ 0 & 0 & 0 & 0 & 0 & E_{66} \end{bmatrix} \begin{Bmatrix} \epsilon_x \\ \epsilon_y \\ \epsilon_z \\ \gamma_{yz} \\ \gamma_{xz} \\ \gamma_{xy} \end{Bmatrix} \tag{3.4}$$

The elasticity tensor, or stiffness matrix, in Eq. 3.4 is also referred to in literature with the notation **C**. The inverse of this matrix, the so-called compliance matrix, referred to by the notation **S**, with the constitutive equation shown in Eq. 3.5. So, the stiffness matrix **C** and compliance matrix **S**, supposedly for simplicity.

$$\begin{Bmatrix} \epsilon_x \\ \epsilon_y \\ \epsilon_z \\ \gamma_{yz} \\ \gamma_{xz} \\ \gamma_{xy} \end{Bmatrix} = \begin{bmatrix} S_{11} & S_{12} & S_{13} & 0 & 0 & 0 \\ S_{21} & S_{22} & S_{23} & 0 & 0 & 0 \\ S_{31} & S_{32} & S_{33} & 0 & 0 & 0 \\ 0 & 0 & 0 & S_{44} & 0 & 0 \\ 0 & 0 & 0 & 0 & S_{55} & 0 \\ 0 & 0 & 0 & 0 & 0 & S_{66} \end{bmatrix} \begin{Bmatrix} \sigma_x \\ \sigma_y \\ \sigma_z \\ \tau_{yz} \\ \tau_{xz} \\ \tau_{xy} \end{Bmatrix} \tag{3.5}$$

For plates and composite laminates, the thickness of the laminate is much smaller compared to the other laminate dimensions. In such cases the laminate can be assumed to be in a state of plane stress. The out-of-plane stresses in a plane stress state are negligible compared to the in-plane stresses.

$$\sigma_z = \tau_{yz} = \tau_{xz} = 0 \tag{3.6}$$

In this plane-stress state, the consitutive relations can be reduced further, leading to the relations in Eqs. 3.7 and 3.8, where the matrix on the right-hand-side of Eq. 3.7 is known as the **Q** matrix. This relation is valid for a composite ply or laminate if, and only if, the coordinate system is orthotropic. For a composite ply this would imply the coordinate system having either the $x-$ or $y-$axis coincide with the fibre direction. If this is not the case, the matrix entries in Eq. 3.7 which are zero, would be non-zero to account for the coupling effects.

$$\begin{Bmatrix} \sigma_x \\ \sigma_y \\ \tau_{xy} \end{Bmatrix} = \begin{bmatrix} Q_{xx} & Q_{xy} & 0 \\ Q_{xy} & Q_{yy} & 0 \\ 0 & 0 & Q_{ss} \end{bmatrix} \begin{Bmatrix} \epsilon_x \\ \epsilon_y \\ \gamma_{xy} \end{Bmatrix} \tag{3.7}$$

$$\begin{aligned} Q_{xx} &= \frac{E_x}{(1-\nu_{xy}\nu_{yx})} \\ Q_{xy} &= \frac{\nu_{xy}E_y}{(1-\nu_{xy}\nu_{yx})} \\ Q_{yy} &= \frac{E_y}{(1-\nu_{xy}\nu_{yx})} \\ Q_{ss} &= G_{xy} \end{aligned} \tag{3.8}$$

As mentioned before, the **Q** matrix is valid when the coordinate system of a ply is aligned with the fibre orientations in that ply. If this is not the case, i.e. the fibres are under an angle, the **Q** matrix will change. In reference literature this procedure is explained thoroughly, so only the final expression for the rotated matrix, $\overline{\mathbf{Q}}$, will be shown and the corresponding transformation matrix, **T**.

$$\overline{\mathbf{Q}} = \mathbf{T}^{-1}\mathbf{Q}\mathbf{T}^{-\mathbf{T}} = \begin{bmatrix} \overline{Q}_{11} & \overline{Q}_{12} & \overline{Q}_{16} \\ \overline{Q}_{12} & \overline{Q}_{22} & \overline{Q}_{26} \\ \overline{Q}_{16} & \overline{Q}_{26} & \overline{Q}_{66} \end{bmatrix} \tag{3.9}$$

With the transformation matrix **T**:

$$T = \begin{bmatrix} cos^2(\theta) & sin^2(\theta) & 2sin(\theta)cos(\theta) \\ sin^2(\theta) & cos^2(\theta) & -2sin(\theta)cos(\theta) \\ -sin(\theta)cos(\theta) & sin(\theta)cos(\theta) & cos^2(\theta) - sin^2(\theta) \end{bmatrix} \tag{3.10}$$

In practice for laminates, the force and moment resultants are used more often than the stresses. These resultants can be obtained by integrating through the thickness of a laminate, indicated with h, see Eq. 3.11. These resultants are thus in units of force or moment per unit length of the laminate, and are also referred to as running loads.

$$
\begin{aligned}
N_x &= \int_{-h/2}^{h/2} \sigma_x dz & M_x &= \int_{-h/2}^{h/2} \sigma_x z dz \\
N_y &= \int_{-h/2}^{h/2} \sigma_y dz & M_y &= \int_{-h/2}^{h/2} \sigma_y z dz \\
N_{xy} &= \int_{-h/2}^{h/2} \tau_{xy} dz & M_{xy} &= \int_{-h/2}^{h/2} \tau_{xy} z dz
\end{aligned} \tag{3.11}
$$

To compute these integrals, Eqs. 3.7 and 3.9 can be used. The entries for the strain vector must then be defined. The standard Kirchoff assumptions for plate theory are used, where the plane sections remain plane and perpendicular to the neutral axis under bending loads. For the strain vector entries two components of the strain are differentiated, the mid-plane strains and the strains due to the bending curvatures. These curvature strains are assumed to vary linearly throughout the thickness of the laminate and are zero at the neutral axis which is assumed to be at the mid-point through the thickness. The entries for the strain vector are thus defined as in Eq. 3.12. As the stiffnesses in each ply are constant, but may vary from ply to ply, these integrals become summations over the plies in the laminate.

$$
\begin{aligned}
\epsilon_{xx} &= \epsilon_{x0} + z \cdot \kappa_x \\
\epsilon_{yy} &= \epsilon_{y0} + z \cdot \kappa_y \\
\gamma_{xy} &= \gamma_{xy0} + z \cdot \kappa_{xy}
\end{aligned} \tag{3.12}
$$

Computing the integrals will then yield the relations between the in-plane running loads N_x, N_y, N_{xy}, M_x, M_y, M_{xy} and the strains and curvatures from Eq. 3.12. Starting with the relation between the in-plane running loads in Eq. 3.13. As can be seen in Eq. 3.13, the integration of the stiffness over the laminate thickness becomes a summation of the stiffness per ply, where h_k is the thickness per ply in the laminate.

$$
\begin{Bmatrix} N_x \\ N_y \\ N_{xy} \end{Bmatrix} = \int_{-h/2}^{h/2} \begin{Bmatrix} \sigma_x \\ \sigma_y \\ \tau_{xy} \end{Bmatrix} dz = \sum_{k=1}^{N} \int_{h_k} \begin{Bmatrix} \sigma_x \\ \sigma_y \\ \tau_{xy} \end{Bmatrix}_k dz \tag{3.13}
$$

In Eq. 3.13, the relations from Eqs. 3.9 and 3.12 can be input. Again, the integral of the laminate thickness becomes a summation of the integral over each ply thickness h_k.

$$
\begin{Bmatrix} N_x \\ N_y \\ N_{xy} \end{Bmatrix} = \sum_{k=1}^{N} \int_{h_k} \overline{\mathbf{Q}}_k \boldsymbol{\epsilon} dz = \sum_{k=1}^{N} \int_{h_k} \begin{bmatrix} \overline{Q}_{11} & \overline{Q}_{12} & \overline{Q}_{16} \\ \overline{Q}_{12} & \overline{Q}_{22} & \overline{Q}_{26} \\ \overline{Q}_{16} & \overline{Q}_{26} & \overline{Q}_{66} \end{bmatrix} (\boldsymbol{\epsilon}^{\mathbf{0}} + z\boldsymbol{\kappa}) dz \tag{3.14}
$$

Then, separating the contributions due to the membrane strains and the curvature strains, Eq. 3.16 is obtained.

$$
\begin{Bmatrix} N_x \\ N_y \\ N_{xy} \end{Bmatrix} = \sum_{k=1}^{N} \int_{h_k} \begin{bmatrix} \overline{Q}_{11} & \overline{Q}_{12} & \overline{Q}_{16} \\ \overline{Q}_{12} & \overline{Q}_{22} & \overline{Q}_{26} \\ \overline{Q}_{16} & \overline{Q}_{26} & \overline{Q}_{66} \end{bmatrix} \boldsymbol{\epsilon}^{\mathbf{0}} dz + \sum_{k=1}^{N} \int_{h_k} \begin{bmatrix} \overline{Q}_{11} & \overline{Q}_{12} & \overline{Q}_{16} \\ \overline{Q}_{12} & \overline{Q}_{22} & \overline{Q}_{26} \\ \overline{Q}_{16} & \overline{Q}_{26} & \overline{Q}_{66} \end{bmatrix} z\boldsymbol{\kappa} dz \tag{3.15}
$$

$$\begin{Bmatrix} N_x \\ N_y \\ N_{xy} \end{Bmatrix} = \begin{bmatrix} A_{11} & A_{12} & A_{16} \\ A_{12} & A_{22} & A_{26} \\ A_{16} & A_{26} & A_{66} \end{bmatrix} \boldsymbol{\epsilon^0} + \begin{bmatrix} B_{11} & B_{12} & B_{16} \\ B_{12} & B_{22} & B_{26} \\ B_{16} & B_{26} & B_{66} \end{bmatrix} \boldsymbol{\kappa} \tag{3.16}$$

Where **A** is the membrane stiffness matrix and **B** is the extension-bending coupling matrix. The components of the **A** and **B** matrix are defined as shown in Eqs. 3.17 and 3.18.

$$\mathbf{A} = \sum_{k=1}^{N} \int_{h_k} \overline{\mathbf{Q}}_k dz = \sum_{k=1}^{N} \overline{\mathbf{Q}}_k (z_k - z_{k-1}) \tag{3.17}$$

$$\mathbf{B} = \sum_{k=1}^{N} \int_{h_k} \overline{\mathbf{Q}}_k z dz = \sum_{k=1}^{N} \overline{\mathbf{Q}}_k \frac{1}{2} (z_k^2 - z_{k-1}^2) \tag{3.18}$$

An analogous procedure can be followed to obtain the relations between the running moment loads, which can be seen from Eqs. 3.19 through 3.22.

$$\begin{Bmatrix} M_x \\ M_y \\ M_{xy} \end{Bmatrix} = \int_{-h/2}^{h/2} \begin{Bmatrix} \sigma_x \\ \sigma_y \\ \tau_{xy} \end{Bmatrix} z dz = \sum_{k=1}^{N} \int_{h_k} \begin{Bmatrix} \sigma_x \\ \sigma_y \\ \tau_{xy} \end{Bmatrix}_k z dz \tag{3.19}$$

$$\begin{Bmatrix} M_x \\ M_y \\ M_{xy} \end{Bmatrix} = \sum_{k=1}^{N} \int_{h_k} \overline{\mathbf{Q}}_k \boldsymbol{\epsilon} z dz = \sum_{k=1}^{N} \int_{h_k} \begin{bmatrix} \overline{Q}_{11} & \overline{Q}_{12} & \overline{Q}_{16} \\ \overline{Q}_{12} & \overline{Q}_{22} & \overline{Q}_{26} \\ \overline{Q}_{16} & \overline{Q}_{26} & \overline{Q}_{66} \end{bmatrix} (\boldsymbol{\epsilon^0} + z\boldsymbol{\kappa}) z dz \tag{3.20}$$

$$\begin{Bmatrix} M_x \\ M_y \\ M_{xy} \end{Bmatrix} = \sum_{k=1}^{N} \int_{h_k} \begin{bmatrix} \overline{Q}_{11} & \overline{Q}_{12} & \overline{Q}_{16} \\ \overline{Q}_{12} & \overline{Q}_{22} & \overline{Q}_{26} \\ \overline{Q}_{16} & \overline{Q}_{26} & \overline{Q}_{66} \end{bmatrix} \boldsymbol{\epsilon^0} z dz + \sum_{k=1}^{N} \int_{h_k} \begin{bmatrix} \overline{Q}_{11} & \overline{Q}_{12} & \overline{Q}_{16} \\ \overline{Q}_{12} & \overline{Q}_{22} & \overline{Q}_{26} \\ \overline{Q}_{16} & \overline{Q}_{26} & \overline{Q}_{66} \end{bmatrix} z^2 \boldsymbol{\kappa} dz \tag{3.21}$$

$$\begin{Bmatrix} M_x \\ M_y \\ M_{xy} \end{Bmatrix} = \begin{bmatrix} B_{11} & B_{12} & B_{16} \\ B_{12} & B_{22} & B_{26} \\ B_{16} & B_{26} & B_{66} \end{bmatrix} \boldsymbol{\epsilon^0} + \begin{bmatrix} D_{11} & D_{12} & D_{16} \\ D_{12} & D_{22} & D_{26} \\ D_{16} & D_{26} & D_{66} \end{bmatrix} \boldsymbol{\kappa} \tag{3.22}$$

Where the definition for the **D** matrix is given in Eq. 3.23.

$$\mathbf{D} = \sum_{k=1}^{N} \int_{h_k} \overline{\mathbf{Q}}_k z^2 dz = \sum_{k=1}^{N} \overline{\mathbf{Q}}_k \frac{1}{3} (z_k^3 - z_{k-1}^3) \tag{3.23}$$

Combining these relations, the **ABD** matrix is obtained, Eq. 3.24, relating the forces and moments to the mid-plane strains and curvatures.

$$\begin{Bmatrix} N_x \\ N_y \\ N_{xy} \\ M_x \\ M_y \\ M_{xy} \end{Bmatrix} = \begin{bmatrix} A_{11} & A_{12} & A_{16} & B_{11} & B_{12} & B_{16} \\ A_{12} & A_{22} & A_{26} & B_{12} & B_{22} & B_{26} \\ A_{16} & A_{26} & A_{66} & B_{16} & B_{26} & B_{66} \\ B_{11} & B_{12} & B_{16} & D_{11} & D_{12} & D_{16} \\ B_{12} & B_{22} & B_{26} & D_{12} & D_{22} & D_{26} \\ B_{16} & B_{26} & B_{66} & D_{16} & D_{26} & D_{66} \end{bmatrix} \begin{Bmatrix} \epsilon_{x0} \\ \epsilon_{y0} \\ \gamma_{xy0} \\ \kappa_x \\ \kappa_y \\ \kappa_{xy} \end{Bmatrix} \tag{3.24}$$

Coming back to the assumption made earlier, that the neutral axis of the laminate is positioned at the mid-point through the thickness. If this assumption is true, and the laminate is said to be symmetric, the **B** matrix is zero. In the case where the assumption is false, and the distribution of stiffness (ply orientations) above and below the mid-point is not symmetric, this translates to a non-zero **B** matrix. For symmetric laminates:

$$\begin{bmatrix} \mathbf{A} & \mathbf{B} \\ \mathbf{B} & \mathbf{D} \end{bmatrix} = \begin{bmatrix} A_{11} & A_{12} & A_{16} & 0 & 0 & 0 \\ A_{12} & A_{22} & A_{26} & 0 & 0 & 0 \\ A_{16} & A_{26} & A_{66} & 0 & 0 & 0 \\ 0 & 0 & 0 & D_{11} & D_{12} & D_{16} \\ 0 & 0 & 0 & D_{12} & D_{22} & D_{26} \\ 0 & 0 & 0 & D_{16} & D_{26} & D_{66} \end{bmatrix} \tag{3.25}$$

In this work, only symmetric laminates will be considered. This implies that the behaviour for the in-plane strains, $\boldsymbol{\epsilon}^{\mathbf{0}}$, and curvatures $\boldsymbol{\kappa}$ are decoupled and can be considered separately in the the analysis. This is with the exception for buckling behaviour, where non-linear strains are considered to determine the stability behaviour of the laminate.

When considering variable stiffness laminates, the approach taken in this work is adopted from the work by Gürdal [3]. The values of the **ABD** matrix are then no longer valid for an entire laminate, as is the case for conventional composite laminates, but are a function of the position on the laminate. Written in mathematical terms, this means:

$$\begin{bmatrix} \mathbf{A} & \mathbf{B} \\ \mathbf{B} & \mathbf{D} \end{bmatrix} = \begin{bmatrix} \mathbf{A}(x,y) & \mathbf{B}(x,y) \\ \mathbf{B}(x,y) & \mathbf{D}(x,y) \end{bmatrix} \tag{3.26}$$

3.2 Governing Equations using Energy Methods

In this section, the governing equations used in this work are derived. The method chosen is using the energy methods, as it is a robust method when exact solutions are difficult to obtain. Due to the nature of the problem in this work, where the laminate has a cut-out, minimising the energy stored in the system to obtain an approximate solution is a powerful solution. Two principles of energy minimisation are of interest, the minimum potential energy and minimum complementary energy [1]. Both methods will be used, the principle of minimum potential energy for the out-of-plane behaviour and the principle of minimum complementary energy for the in-plane behaviour of the laminate. Since the derivations are analogous, only one will be shown here.

3.2.1 Energy Methods

The energy methods start from defining the total energy in a body. According to the principle of virtual work, the increment of work done on a body equals the increment of internal energy stored in the body. If the total energy is defined as the difference between the internal energy and the work done by external forces, this can be expressed as shown in Eq. 3.27 [1]. Where

the Total Potential Energy is expressed as the summation of the internal energy, or strain energy U, and the potential energy V, or negative of external work. The goal is to find the point where the TPE is at a minimum, i.e. its derivative to be equal to zero. To obtain this expression, the strain and potential energy expressions need to be derived.

$$\Pi = U + V \tag{3.27}$$

The definition for the strain energy can be expressed as the summation of all products of stresses and corresponding strains.

$$U = \frac{1}{2}\iiint_V \{\sigma_x\epsilon_x + \sigma_y\epsilon_y + \sigma_z\epsilon_z + \tau_{xy}\gamma_{xy} + \tau_{xz}\gamma_{xz} + \tau_{yz}\gamma_{yz}\}\, dx\ dy\ dz$$

Where the integration is over the entire volume V of the body. For a plate, this can be reduced by applying the Kirchhoff assumptions and neglecting the deformation along the thickness through the plate ($\gamma_{xz} = \gamma_{yz} = \epsilon_z = 0$).

$$U = \frac{1}{2}\iiint_V \{\sigma_x\epsilon_x + \sigma_y\epsilon_y + \tau_{xy}\gamma_{xy}\} dx\ dy\ dz \tag{3.28}$$

Substituting Eqs. 3.12 into this expression yields the following expression.

$$U = \frac{1}{2}\iiint_V \{\sigma_x(\epsilon_{x0} + z\kappa_x) + \sigma_y(\epsilon_{y0} + z\kappa_y) + \tau_{xy}(\gamma_{xy0} + z\kappa_{xy})\} dx\ dy\ dz \tag{3.29}$$

Integration through the thickness gives yields the expression in terms of the running forces and moments. The integral then is no longer over the volume V, but over the area domain Ω.

$$U = \frac{1}{2}\iint_\Omega \{(N_x\epsilon_{x0} + M_x\kappa_x) + (N_y\epsilon_{y0} + M_y\kappa_y) + (N_{xy}\gamma_{xy0} + M_{xy}\kappa_{xy})\}\, dx\ dy \tag{3.30}$$

This can be expanded further by using the Eqs. 3.24. Collecting terms gives the energy expression in Eq. 3.31. Note that in the case of VAT laminates, the A, B and D matrix values are also functions of x and y, although here it is omitted for legibility.

$$\begin{aligned} U = {} & \frac{1}{2}\iint_\Omega \begin{Bmatrix} A_{11}\epsilon_{x0}^2 + 2A_{12}\epsilon_{x0}\epsilon_{y0} + 2A_{16}\epsilon_{x0}\gamma_{xy0} \\ +A_{22}\epsilon_{y0}^2 + 2A_{26}\epsilon_{y0}\gamma_{xy0} + A_{66}\gamma_{xy0}^2 \end{Bmatrix} dx\ dy \\ & + \iint_\Omega \begin{Bmatrix} B_{11}\ \epsilon_{x0}\kappa_x + B_{12}(\epsilon_{y0}\kappa_x + \epsilon_{x0}\kappa_y) + B_{16}\ (\gamma_{xy0}\kappa_x + \epsilon_{x0}\kappa_{xy}) \\ +B_{22}\ \epsilon_{y0}\kappa_y + B_{26}(\gamma_{xy0}\kappa_y + \epsilon_{y0}\kappa_{xy}) + B_{66}\ \gamma_{xy0}\kappa_{xy} \end{Bmatrix} dx\ dy \\ & + \frac{1}{2}\iint_\Omega \begin{Bmatrix} D_{11}\ \kappa_x^2 + 2D_{12}\ \kappa_x\kappa_y + 2D_{16}\ \kappa_x\kappa_{xy} \\ +D_{22}\ \kappa_y^2 + 2D_{26}\ \kappa_y\kappa_{xy} + D_{66}\ \kappa_{xy}^2 \end{Bmatrix} dx\ dy \end{aligned} \tag{3.31}$$

To obtain the governing equations as a function of the unknown displacements, the expressions for the mid-plane strains $\epsilon_{x0}, \epsilon_{y0}, \gamma_{xy0}$ and the curvatures κ_x, κ_y and κ_{xy} must be defined. The

linear strain-displacement equations are used, as seen in Eq. 3.32, where u, v and w denote the displacement in x, y and z direction respectively.

$$\begin{aligned} \epsilon_{x0} &= \frac{\partial u}{\partial x} & \kappa_x &= -\frac{\partial^2 w}{\partial x^2} \\ \epsilon_{y0} &= \frac{\partial v}{\partial y} & \kappa_y &= -\frac{\partial^2 w}{\partial y^2} \\ \gamma_{xy0} &= \frac{\partial u}{\partial y} + \frac{\partial v}{\partial x} & \kappa_{xy} &= -2\frac{\partial^2 w}{\partial x \partial y} \end{aligned} \tag{3.32}$$

Filling in the expression from Eq. 3.32, the final expression for the internal energy of a laminate is obtained in terms of displacements u, v and w.

$$\begin{aligned} U = \frac{1}{2}\iint_\Omega \begin{Bmatrix} A_{11}\left(\frac{\partial u}{\partial x}\right)^2 + 2A_{12}\frac{\partial u}{\partial x}\frac{\partial v}{\partial y} + 2A_{16}\frac{\partial u}{\partial x}\left(\frac{\partial u}{\partial y} + \frac{\partial v}{\partial x}\right) \\ +A_{22}\,\frac{\partial v}{\partial y}^2 + 2A_{26}\,\frac{\partial v}{\partial y}\left(\frac{\partial u}{\partial y} + \frac{\partial v}{\partial x}\right) + A_{66}\left(\frac{\partial u}{\partial y} + \frac{\partial v}{\partial x}\right)^2 \end{Bmatrix} dx\ dy \\ -\iint_\Omega \begin{Bmatrix} B_{11}\frac{\partial u}{\partial x}\frac{\partial^2 w}{\partial x^2} + B_{12}\left(\frac{\partial v}{\partial y}\frac{\partial^2 w}{\partial x^2} + \frac{\partial u}{\partial x}\frac{\partial^2 w}{\partial y^2}\right) + B_{16}\left[\left(\frac{\partial u}{\partial y} + \frac{\partial v}{\partial x}\right)\frac{\partial^2 w}{\partial x^2} + 2\frac{\partial u}{\partial x}\frac{\partial^2 w}{\partial x \partial y}\right] \\ +B_{22}\frac{\partial v}{\partial y}\frac{\partial^2 w}{\partial y^2} + B_{26}\left[\left(\frac{\partial u}{\partial y} + \frac{\partial v}{\partial x}\right)\frac{\partial^2 w}{\partial y^2} + 2\frac{\partial v}{\partial y}\frac{\partial^2 w}{\partial x \partial y}\right] + 2B_{66}\left(\frac{\partial u}{\partial y}\frac{\partial v}{\partial x}\right)\frac{\partial^2 w}{\partial x \partial y} \end{Bmatrix} dx\ dy \\ +\frac{1}{2}\iint_\Omega \begin{Bmatrix} D_{11}\left(\frac{\partial^2 w}{\partial x^2}\right)^2 + 2D_{12}\,\frac{\partial^2 w}{\partial x^2}\frac{\partial^2 w}{\partial y^2} + 4D_{16}\,\frac{\partial^2 w}{\partial x^2}\frac{\partial^2 w}{\partial x \partial y} \\ +D_{22}\left(\frac{\partial^2 w}{\partial y^2}\right)^2 + 4D_{26}\frac{\partial^2 w}{\partial y^2}\frac{\partial^2 w}{\partial x \partial y} + 4D_{66}\left(\frac{\partial^2 w}{\partial x \partial y}\right)^2 \end{Bmatrix} dx\ dy \end{aligned} \tag{3.33}$$

In Eq. 3.33 the decoupled parts of the energy equation can be seen. The first part is dependent on the **A** matrix values and the in-plane displacement only. The second part shows the coupling of the in-plane displacements u and v, and the out-of-plane displacement w combined with the **B** matrix values. Finally, the last part shows only the out-of-plane displacements combined with the **D** matrix values. As stated before, in this work only symmetric laminates with zero **B** matrix will be considered, and thus the in-plane and out-of-plane behaviours can be decoupled. This also entails that the in-plane and out-of-plane problems can be solved separately, thus avoiding the problem encountered by Alhajahmad, where a non-linear system of unknowns needed to be solved [19].

The potential energy, or negative of the external work, is the combination of the forces on the body and the corresponding deformations. A complete overview of the potential energy is shown in Eq. 3.34, where $p_{[x,y,z]}$ denote distributed loads (force per area) on the corresponding plate surface and the N, Q and M loads correspond to the running loads [force/moment per length] as shown in Fig. 3.1.

$$
\begin{aligned}
V = &- \iint_{\Omega} p_x u + p_y v + p_z w \; dx \; dy \\
&- \int_0^b \left[N_x u + N_{xy} v + Q_x w - M_x \left(\frac{\partial w}{\partial x} \right) \right]_{x=0}^{x=a} dy \\
&- \int_0^a \left[N_{xy} u + N_y v + Q_y w - M_y \left(\frac{\partial w}{\partial y} \right) \right]_{y=0}^{y=b} dx
\end{aligned}
\tag{3.34}
$$

3.2.2 Rayleigh-Ritz Method

The Rayleigh-Ritz method is a well known method for solving problems using the energy method. The method consists of applying an approximation solution, or trial function or shape function, in the form of an infinite series function multiplied with unknown coefficients. The workings of the method have been covered in many textbooks such as Megson [23], and will thus be reviewed here only briefly.
The solution approximation function, out-of-plane deflection w in this example, must comply with the boundary conditions for the problem considered. The function can then be used in the expression for the TPE such as the last term of 3.33. In the case of a solution for the out-of-plane deflection of a simply supported plate, the solution approximation can look like shown in Eq. 3.35, where the K_{mn} are the unknown coefficients.

$$
w(x,y) = \sum_{n=1}^{N} \sum_{m=1}^{M} K_{mn} \; sin\left(\frac{m\pi x}{a} \right) \; sin\left(\frac{n\pi y}{b} \right) \tag{3.35}
$$

The objective is to find the position of minimum TPE. However, the expression for the deflection still contains the unknown coefficients K_{mn} in this example. The solution procedure is to find the minimum by differentiating with respect to these unknown coefficients and set the result to zero.

$$
\frac{\partial \Pi}{\partial K_{mn}} = \frac{\partial U}{\partial K_{mn}} + \frac{\partial V}{\partial K_{mn}} = 0 \tag{3.36}
$$

In this manner, the same amount of equations is obtained as unknown coefficients are taken for the approximation, such that this square system can be solved. The reduced expressions for the strain energy U and potential energy V must be input into Eq. 3.36 and the solution can thus be found which complies with the condition of minimum total potential energy. When using solution approximations for deflections such as the out-of-plane deflection example above, the TPE is used and will be elaborated more in Chapter 4. When using solution approximations for the stress-state, the TCE is used. This will be elaborated more in Chapter 5.

3.3 Introducing the Cut-Out

When considering a cut-out in a plate, two things change with respect to the previous theory. First of all, the approximation functions as shown in Eq. 3.35 can no longer capture the deflection behaviour as the plate will show a modified behaviour close to the cut-out. Second, the integration of the energy functions U and V can no longer be done analytically as for a continuous domain. For these two problems, two solutions are proposed in the next sections. The use of the Enriched Rayleigh-Ritz method for the approximation functions and the use of a numerical integration scheme. This integration method also provides solutions for the analysis of VAT laminates, as the $\mathbf{A}$ and $\mathbf{D}$ matrices also become functions of x and y.

3.3.1 Enriched Rayleigh-Ritz Method

The Rayleigh-Ritz method relies on expanding the number of terms in the series solution until convergence is obtained. Convergence can be defined when the error of the model solution w.r.t. the exact solution is below a certain threshold, or when adding an extra term to the series solution does not change the model solution significantly. Furthermore, besides convergence, the set of approximation functions chosen should suit the expected result, e.g. the stress-state or displacement field. If the chosen set of approximation functions is not correct, the number of terms can be increased indefinitely without improving the approximation. This is especially true for plates with discontinuities where, for example, the deflection of a plate is influenced locally due to the presence of a discontinuity such as a cut-out. In such cases, many terms might be required to obtain convergence assuming the approximation functions are capable of capturing these local effects in the plate. To overcome these issues, the Enriching Rayleigh-Ritz (ERR) method is proposed, which is introduced in the work of Huang, Leissa & Li [24] and in the work by Milazzo, Benedetti & Gulizzi [25]. There, the Rayleigh-Ritz method is used while using multiple series solution functions to solve for the vibration of cracked plates. In this procedure, in addition to the standard solutions for out-of-plane displacement of a plate, additional solution series are added to account for the behaviour close to the crack. These functions are named in the work by Milazzo as 'enriching' functions, hence the name for the method. Using the ERR method, additional series solutions can be added to capture the behaviour due to discontinuities in order to reduce the number of terms required for convergence. The use of the ERR method can allow an engineer to model local effects on a laminate more accurately while using less terms with respect to using the general solution series which may need many terms to capture this local behaviour. It also provides a method to deal with the local effects in laminates when dealing with cut-outs, as will be the focus in this work.
To illustrate the procedure, a single term for the strain energy will be expanded using the ERR, as shown in Eq. 3.37. The expression for the strain energy will normally include material properties, but they are excluded here for legibility. The strain energy example consists of the second derivative with respect to x of the function Φ^2. The function Φ in this example consists of three series solution functions, denoted by ϕ_1, ϕ_2 and ϕ_3. The notation of derivatives from hereon is used as $\phi_{,xx}$ rather than $\frac{\partial^2 \phi}{\partial x^2}$, for legibility.

$$U_{example} = \frac{1}{2} \iint_{\Omega} \Phi^2_{,xx}(x, y) \; dxdy \tag{3.37}$$

$$\Phi(x,y) = \sum_{i}^{I}\sum_{j}^{J} A_{ij}\cdot\phi_{1_{ij}}(x,y) + \sum_{m}^{M}\sum_{n}^{N} B_{mn}\cdot\phi_{2_{mn}}(x,y) + \sum_{p}^{P}\sum_{q}^{Q} C_{pq}\cdot\phi_{3_{pq}}(x,y) \tag{3.38}$$

In order to minimise the strain energy, the expression is derived with respect tot the unknown coefficients A_{ij}, B_{mn} and C_{pq}. This leads to the expressions in Eq. 3.39.

$$\begin{aligned}
\frac{\partial U}{\partial A_{ij}} &= \iint_{\Omega} \Phi_{,xx}\cdot\frac{\partial \Phi_{,xx}}{\partial A_{ij}}\ dxdy \\
\frac{\partial U}{\partial B_{mn}} &= \iint_{\Omega} \Phi_{,xx}\cdot\frac{\partial \Phi_{,xx}}{\partial B_{mn}}\ dxdy \\
\frac{\partial U}{\partial C_{pq}} &= \iint_{\Omega} \Phi_{,xx}\cdot\frac{\partial \Phi_{,xx}}{\partial C_{pq}}\ dxdy
\end{aligned} \tag{3.39}$$

In the expressions from Eq. 3.39, the $\Phi_{,xx}$ expressions are those containing all terms from all functions from Eq. 3.38, e.g. all A_{ij}, B_{mn} and C_{pq} terms. The terms $\frac{\partial \Phi_{,xx}}{\partial A_{ij}}$, $\frac{\partial \Phi_{,xx}}{\partial B_{mn}}$ and $\frac{\partial \Phi_{,xx}}{\partial C_{pq}}$ refer only to that specific term with respect to which the derivative is taken and is thus equal to the value of $\phi_{1_{ij}}$, $\phi_{2_{mn}}$ and $\phi_{3_{pq}}$ respectively. This provides a square system of equations with an equal amount of unknowns and functions, and can thus be solved. When entering the functions provided from Eq. 3.38, the system for this example would take the form as shown in Eq. 3.40.

$$\begin{Bmatrix} \frac{\partial U}{\partial A_{ij}} \\ \frac{\partial U}{\partial B_{mn}} \\ \frac{\partial U}{\partial C_{pq}} \end{Bmatrix} = \iint_{\Omega} \begin{bmatrix} \phi_{1_{ij,xx}}\cdot\phi^{\mathbf{T}}_{1_{ij,xx}} & \phi_{2_{mn,xx}}\cdot\phi^{\mathbf{T}}_{1_{ij,xx}} & \phi_{3_{pq,xx}}\cdot\phi^{\mathbf{T}}_{1_{ij,xx}} \\ \phi_{1_{ij,xx}}\cdot\phi^{\mathbf{T}}_{2_{mn,xx}} & \phi_{2_{mn,xx}}\cdot\phi^{\mathbf{T}}_{2_{mn,xx}} & \phi_{3_{pq,xx}}\cdot\phi^{\mathbf{T}}_{2_{mn,xx}} \\ \phi_{1_{ij,xx}}\cdot\phi^{\mathbf{T}}_{3_{pq,xx}} & \phi_{2_{mn,xx}}\cdot\phi^{\mathbf{T}}_{3_{pq,xx}} & \phi_{3_{pq,xx}}\cdot\phi^{\mathbf{T}}_{3_{pq,xx}} \end{bmatrix} \begin{Bmatrix} A_{ij} \\ B_{mn} \\ C_{pq} \end{Bmatrix} dxdy \tag{3.40}$$

$$\begin{Bmatrix} \frac{\partial U}{\partial A_{ij}} \\ \frac{\partial U}{\partial B_{mn}} \\ \frac{\partial U}{\partial C_{pq}} \end{Bmatrix} = [\mathbf{K}] \begin{Bmatrix} A_{ij} \\ B_{mn} \\ C_{pq} \end{Bmatrix}$$

Deriving the strain energy with respect to the unknown coefficients this yields a matrix in Eq. 3.40, which will contain the material and structural properties of the laminate, and is thus referred to as the constitutive stiffness matrix, $\mathbf{K}$. The entries of the stiffness matrix will be of the size as described in Eq. 3.41. The entries which are not on the diagonal show the coupling between the different functions ϕ_1, ϕ_2 and ϕ_3, indicating their interaction.

$$\text{Size of } \mathbf{K} \text{ entries} = \begin{bmatrix} (IJ)\times(IJ) & (IJ)\times(MN) & (IJ)\times(PQ) \\ (MN)\times(IJ) & (MN)\times(MN) & (MN)\times(PQ) \\ (PQ)\times(IJ) & (PQ)\times(MN) & (PQ)\times(PQ) \end{bmatrix} \tag{3.41}$$

Similarly, for the potential energy, V, this process can be done to provide a vector containing the applied loading, or force vector $\mathbf{F}$ for the case of a uniform applied pressure force, p_z.

$$V = -\iint_{Area} p_z \cdot \Phi(x,y)\ dxdy$$

$$\frac{\partial V}{\partial A_{ij}} = -p_z \iint_{\Omega} \frac{\partial \Phi}{\partial A_{ij}}\ dxdy$$
$$\frac{\partial V}{\partial B_{mn}} = -p_z \iint_{\Omega} \frac{\partial \Phi}{\partial B_{mn}}\ dxdy$$
$$\frac{\partial V}{\partial C_{pq}} = -p_z \iint_{\Omega} \frac{\partial \Phi}{\partial C_{pq}}\ dxdy$$

$$\{\mathbf{F}\} = \begin{Bmatrix} \frac{\partial V}{\partial A_{ij}} \\ \frac{\partial V}{\partial B_{mn}} \\ \frac{\partial V}{\partial C_{pq}} \end{Bmatrix} = -p_z \iint_{\Omega} \begin{Bmatrix} \phi_{1_{ij}} \\ \phi_{2_{mn}} \\ \phi_{3_{pq}} \end{Bmatrix}\ dxdy \tag{3.42}$$

3.3.2 Gauss-Legendre Quadrature: Numerical Integration

As mentioned before, a numerical integration scheme will allow the the use of the energy method on domains including a cut-out. The approach taken is quite straightforward, where the energy matrices U and V for the plate with a cut-out are determined by calculating the energies for the pristine plate and for the cut-out section. Then, the resultant energies are obtained by subtracting the integration on the cut-out domain from the integration on the pristine domain. This is illustrated in Fig. 3.2 or in Eq. 3.43 with Ω the domain of the plate containing a cut-out.

$$\iint_{\Omega} f(x,y)\ dx\ dy = \iint_{Pristine} f(x,y)\ dx\ dy - \iint_{Cut-Out} f(x,y)\ dx\ dy \tag{3.43}$$

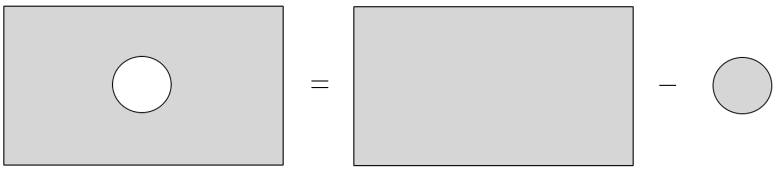

Figure 3.2: Illustration of the straightforward summation procedure.

The integration scheme used to determine the integrals on the right-hand-side (RHS) of Eq. 3.43 is the same as used by Wu et al. [9], the Gauss-Legendre Quadrature method. This numerical method states that the value at one or more discrete points on the domain multiplied with certain weights equals the continuous integral over the entire domain. The mathematical expression is shown in Eq. 3.44 with w_i, w_j the weights for the corresponding

x_i, y_j locations. In order to determine and use generic locations and weights, the domain is translated into natural coordinates (ξ, η) with interval $[-1, 1]$.

$$\iint_{Domain} f(x,y)\ dx\ dy \approx \sum_{i}^{N}\sum_{j}^{M}\ w_i w_j\ f(x_i, y_j) \tag{3.44}$$

The objective is to determine the locations and weights of these integration points for both the rectangular pristine plate domain and the circular cut-out domain.

Rectangular Domain

For a rectangular domain, transforming the laminate coordinates from (x, y) into the natural coordinates (ξ, η) is straightforward. A laminate with dimensions $x = [0; a], y = [0; b]$ in Cartesian coordinates will be transformed to a laminate with dimensions $\xi = [-1; 1], \eta = [-1; 1]$ in natural coordinates. This transformation is according to Eq. 3.45

$$\begin{aligned} \xi &= \frac{2x}{a} - 1 \\ \eta &= \frac{2y}{b} - 1 \end{aligned} \tag{3.45}$$

The question remains, at which discrete points (x_i, y_j) must the function be evaluated and what weights correspond to those points? This is illustrated using an example determining the integral of a generic third-order polynomial on domain a to b by evaluating the function at two points multiplied with a certain weighting factor, shown in the expression in Eq. 3.46. There are now four unknowns, w_1, w_2, x_1 and x_2. If the generic third-order polynomial takes the form shown in Eq. 3.47, the exact integral on domain a to b can be determined relatively easy as shown in Eq. 3.48.

$$\int_a^b f(x)dx = w_1 f(x_1) + w_2 f(x_2) \tag{3.46}$$

$$f(x) = c_0 + c_1 x + c_2 x^2 + c_3 x^3 \tag{3.47}$$

$$\int_a^b f(x)dx = c_0(b-a) + c_1\left(\frac{b^2-a^2}{2}\right) + c_2\left(\frac{b^3-a^3}{3}\right) + c_3\left(\frac{b^4-a^4}{4}\right) \tag{3.48}$$

The expression for $f(x)$ in Eq. 3.47 can be inserted into the RHS of Eq. 3.46. Collecting the terms multiplied with the unknown constants c_0 to c_3 will yield the expression in Eq. 3.49.

$$\begin{aligned} &w_1 f(x_1) + w_2 f(x_2) = \\ &\qquad c_0(w_1 + w_2) + c_1(w_1 x_1 + w_2 x_2) + c_2(w_1 x_1^2 + w_2 x_2^2) + c_3(w_1 x_1^3 + w_2 x_2^3) \end{aligned} \tag{3.49}$$

If it is required that the RHS of Eqs. 3.48 and 3.49 are equal, and requiring that this must be true for every generic third-order polynomial, the terms multiplied with the random coefficients c_0 to c_3 in both expressions must be equal. This gives four equations with four unknowns, which will allow the determination of the discrete points x_1, x_2 and their corresponding weights w_1, w_2.

This method is a well known numerical integration method using the Legendre polynomials rather than the polynomial in Eq. 3.47 applied on a natural coordinate system ranging from $[-1, 1]$ for which the Legendre polynomials are defined. This yields the weights and locations as tabulated in Table 3.1 for number of evaluation points up to three. The method is shown to be accurate for any polynomial function given that N points are used for a polynomial function of order $(2N - 1)$.

Table 3.1: Weight and locations for the Gauss-Legendre quadrature.

N	Weights	Locations
1	1, 1	± 0.57735
2	0.555, 0.888, 0.555	-0.77459, 0, 0.77459
3	0.652, 0.347, 0.347, 0.652	± 0.33998, ± 0.86113

Extending this method to 2D domains is relatively straightforward. The steps taken from Eq. 3.46 to 3.49 can be repeated for the $y-$axis to obtain the expression in Eq. 3.44 where the w_i and w_j are the weights for the x and y respectively, which can be found in table 3.1 for the rectangle with domain $\xi = [-1, 1], \eta = [-1, 1]$.

In Fig. 3.3, the Gauss points are plotted for a 2D example with equal amount of evaluation points for the ξ and η axes. It can be seen that the evaluation points of the Gaussian quadrature have a higher density closer to the edges of the domain.

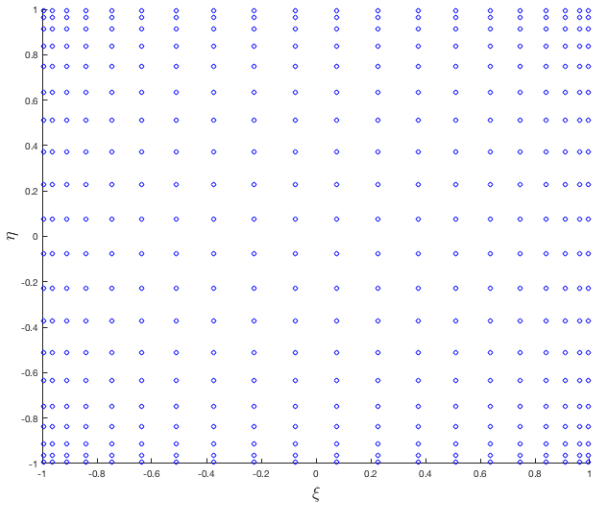

Figure 3.3: The quadrature points projected in the natural coordinates (ξ, η) taking 20 sampling points per axis, 400 sampling points in total.

Circular Domain

Applying the Gauss-Legendre quadrature numerical integration over a circular domain requires some further transformation. Shivaram [26] presented a method for the numerical integration over a quarter unit circle. This method will be repeated here, but now for the full circle.

The integral of an arbitrary function $f(x, y)$ over a unit circle is written as in Eq. 3.50.

$$\begin{aligned} I &= \iint_{\Omega} f(x,y)dx\ dy \\ &= \int_0^1 \int_0^{\sqrt{1-x^2}} f(x,y)dy\ dx \\ &= \int_0^1 \int_0^{\sqrt{1-y^2}} f(x,y)dx\ dy \end{aligned} \tag{3.50}$$

From Shivaram [26], the definitions for the coordinates in the (r, θ) coordinate system are obtained in Eq. 3.51.

$$\begin{aligned} r &= \left(\frac{b-a}{2}\right)\xi + \left(\frac{b+a}{2}\right) \\ \theta &= \left(\frac{\beta-\alpha}{a}\right)\eta + \left(\frac{\beta+\alpha}{2}\right) \end{aligned} \tag{3.51}$$

Where $a = 0$, $b = R$, the radius of the circle, $\alpha = 0$ and $\beta = 2\pi$ for the full circle. The value of the β here deviates from the work by Shivaram as in this work the full circle is used. Filling this in for the expressions in Eq. 3.51, Eq. 3.52 is obtained.

$$\begin{aligned} r &= \frac{R(\xi+1)}{2} \\ \theta &= \pi(\eta+1) \end{aligned} \tag{3.52}$$

Then, inserting the expression from Eq. 3.52 into the definitions for x and y yields Eq. 3.53.

$$\begin{aligned} x = r\ cos\theta &= \frac{R(\xi+1)}{2} cos\left(\pi[\eta+1]\right) \\ y = r\ sin\theta &= \frac{R(\xi+1)}{2} sin\left(\pi[\eta+1]\right) \end{aligned} \tag{3.53}$$

The expression from Eq. 3.53 can be inserted into the integral from Eq. 3.50 to give Eq. 3.54.

$$\begin{aligned} I &= \int_0^1 \int_0^{\sqrt{1-y^2}} f(x,y)dx\ dy \\ &= \int_{-1}^1 \int_{-1}^1 f\left[x(\xi,\eta), y(\xi,\eta)\right]\ J\ d\xi\ d\eta \end{aligned} \tag{3.54}$$

Where J, the Jacobian, is defined as stated in Eq. 3.55.

$$J = \begin{vmatrix} \frac{\partial x}{\partial \xi} & \frac{\partial y}{\partial \xi} \\ \frac{\partial x}{\partial \eta} & \frac{\partial y}{\partial \eta} \end{vmatrix} = \frac{R^2(\xi+1)\pi}{4} \tag{3.55}$$

Going back to the formulation of the Gauss-Legendre formulation, combining Eqs. 3.44, 3.53, 3.54 and 3.55, the integral can be written as:

$$\begin{aligned} I &= \int_{-1}^{1}\int_{-1}^{1} f\left[\frac{R(\xi+1)}{2}cos\left(\pi[\eta+1]\right), \frac{R(\xi+1)}{2}sin\left(\pi[\eta+1]\right)\right]\frac{R^2(\xi+1)\pi}{4}d\xi\ d\eta \\ &= \sum_{i=1}^{n}\sum_{j=1}^{n}\frac{R^2(\xi+1)\pi}{4}w_i w_j f\left[x(\xi_i,\eta_j), y(\xi_i,\eta_j)\right] \end{aligned} \tag{3.56}$$

Where (ξ_i, η_j) are the Gaussian points and $w_i w_j$ the corresponding weights from Table 3.1. Following the steps from Shivaram [26], the expression is rewritten into Eqs. 3.57 and 3.58. The coordinates ξ and η now denote the number of points in the radial and circumferential directions around the origin center in the natural coordinate system. When n points are taken in either direction, the total number of points N in Eq. 3.57 is $n \times n$.

$$I = \sum_{k}^{N=n\times n} a_k f(x_k, y_k) \tag{3.57}$$

Where:

$$\begin{aligned} a_k &= \frac{R^2(\xi+1)\pi}{4}w_i w_j \\ x_k &= \frac{R(\xi+1)}{2}cos\left(\pi[\eta+1]\right) \\ y_k &= \frac{R(\xi+1)}{2}sin\left(\pi[\eta+1]\right) \end{aligned} \tag{3.58}$$

These Gaussian quadrature points can be seen in Fig. 3.4. It can be seen that the quadrature points again seem to have a bias towards the edges of the domain, in this case the edges are at $\theta = 0$ and $r = R$.

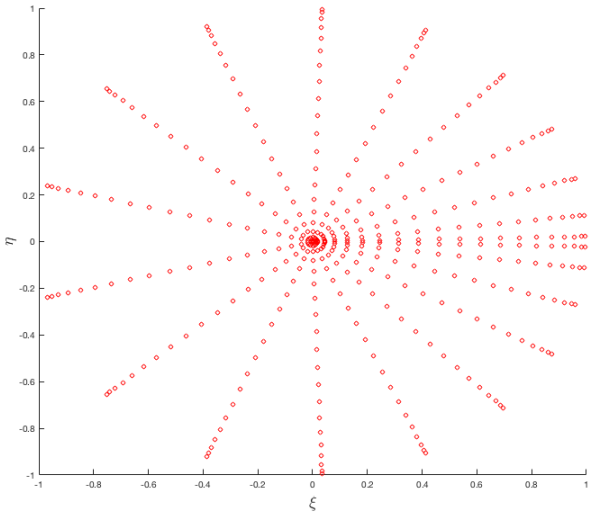

Figure 3.4: The (r, θ) quadrature points projected in the (ξ, η) plane. 20 Sampling points taken per axis, 400 sampling points in total.

As an illustration, these points can be transformed back into x, y coordinates for a plate with a central located hole with dimensions $a = 10$, $b = 5$ and $R = 2$, as visualised in Fig. 3.5.

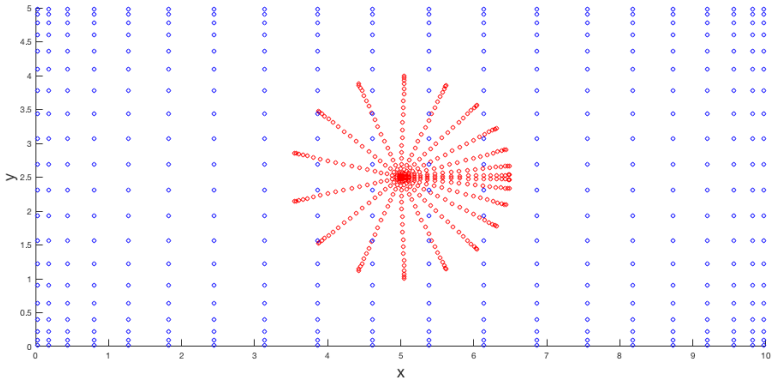

Figure 3.5: Quadrature points plotted into x, y coordinates for a plate with $a = 10$, $b = 5$ (a unit-less example) and a central located hole with $R = 1.5$.

In summary, the Gaussian quadrature points allow for numerical integration, given that enough integration points are chosen to approach the exact solution for the integral. Thus all components in the energy integral which are a functions of (x, y) must be considered, including the material properties in the **ABD** matrix for a VAT laminate.

Chapter 4

Out-of-Plane Behaviour

In this chapter, the out-of-plane analysis is presented. In this chapter, the out-of-plane behaviour is determined for plates and lamintes under simply-supported conditions. First, the relevant equations are presented in Section 4.1, starting from the governing equations derived in Section 3.2.1. Second, the trial functions used for the out-of-plane deflection are presented in Section 4.2. Third, the application of all the theory and analysis is presented using a flowchart in Section 4.3. Finally, the results are presented for applications of pristine isotropic plates, pristine VAT laminates and isotropic plates with cut-outs in Section 4.4.

4.1 Governing Equations

In Section 3.2.1, the complete formulations for the strain energy and the potential energy are given by Eqs. 3.33 and 3.34 respectively. For an out-of-plane problem formulation, the in-plane terms in the strain energy can be removed as no stretching of the mid-plane is assumed, thus $\frac{\partial u}{\partial x}, \frac{\partial v}{\partial y}$ are zero. All terms for the in-plane and out-of-plane coupling, e.g. the terms related to the B_{ij} values, are zero due to the symmetric layup assumption, and thus zero **B** matrix values. This yields Eq. 4.1 for the strain energy.

$$U = \frac{1}{2}\iint_{\Omega} \begin{Bmatrix} D_{11}\left(\frac{\partial^2 w}{\partial x^2}\right)^2 + 2D_{12}\,\frac{\partial^2 w}{\partial x^2}\frac{\partial^2 w}{\partial y^2} + 4D_{16}\,\frac{\partial^2 w}{\partial x^2}\frac{\partial^2 w}{\partial x \partial y} \\ +D_{22}\left(\frac{\partial^2 w}{\partial y^2}\right)^2 + 4D_{26}\frac{\partial^2 w}{\partial y^2}\frac{\partial^2 w}{\partial x \partial y} + 4D_{66}\left(\frac{\partial^2 w}{\partial x \partial y}\right)^2 \end{Bmatrix} dx\ dy \tag{4.1}$$

In the case where only a uniform pressure load p_z is applied to the surface of the laminate, the expression for the potential energy, Eq. 3.34, can also be reduced. As there are no loads applied on the laminate besides the distributed load p_z normal to the laminate surface, the potential energy reduces to Eq. 4.2.

$$V = -\iint_{\Omega} p_z \cdot w\ dxdy \tag{4.2}$$

4.2 Trial Functions

For the out-of-plane deflection, the trial functions herein developed consist of the standard solutions used for pristine plates, shown previously in Eq. 3.35, and two enriching functions. The enriching functions are based on the functions used by Huang et al. [24] and Milazzo et al. [25], where radial positions are used w.r.t. the crack tips and full Fourier terms. Taking inspiration from those functions and after several attempts, the final enriching functions are presented in Eqs. 4.3, 4.4, 4.5 and 4.6. During the process of finding the functions presented in Eqs. 4.5 and 4.6 the functions were checked for compliance with imposed criteria. These criteria included that the value of the functions should increase with decreasing radial distance, r, and should be able to describe fluctuations around the circumference position, θ. Furthermore, the convergence of the entries for the $\mathbf{K}$ matrix and $\mathbf{F}$ was checked with increasing number of integration points. The coefficients A_{ij} and B_{mn} are not to be confused with the material properties from the $\mathbf{ABD}$ matrix, these letters were chosen in alphabetical order, starting at A for no particular reason.

$$w = w_1(x,y) + w_2(x,y) + w_3(x,y) \tag{4.3}$$

$$w_1(x,y) = \sum_{i=1}^{I}\sum_{j=1}^{J} A_{ij}\ sin\left(\frac{i\pi x}{a}\right)\ sin\left(\frac{j\pi y}{b}\right) \tag{4.4}$$

$$w_2(x,y) = g_w(\xi,\eta)\cdot\left\{\sum_{m=1}^{M}\sum_{n=0}^{N} B_{mn}\cdot(1-r)^m\cdot cos(n\theta)\right\} \tag{4.5}$$

$$w_3(x,y) = g_w(\xi,\eta)\cdot\left\{\sum_{m=1}^{M}\sum_{n=1}^{N} C_{mn}\cdot(1-r)^m\cdot sin(n\theta)\right\} \tag{4.6}$$

$$g_w(x,y) = (1-\xi^2)\cdot(1-\eta^2)$$

In the enriching functions in Eq. 4.5 and 4.6, the result is guaranteed to be zero at the outer edges by means of the boundary condition forcing function, g_w. This function is previously shown in Eq. 2.6 and is applied here with $k_{i/j} = 1$ to adhere to simply supported boundary conditions.
Related to the starting point for m, n of function w_2 corresponding to the B_{mn} coefficients, when $m = 0, n = 0$ the function would be equal to 1 and the outcome would equal the boundary forcing function. To prevent this, the starting point is taken as $m = 1$. Similarly, for function w_3 corresponding to the C_{mn} coefficients, the starting point for n is taken as 1, as at $n = 0$, the solution of the function is zero and will lead to a singular strain energy matrix as the value for $C_{m,n=0}$ would be undetermined.

For the current load case, where only a uniform pressure p_z is applied to the laminate surface, the result when entering the w into the strain and potential energy functions will yield the system in Eq. 4.7. The matrix $[K]$ and vector $\{F\}$ are a result from the integrations of the strain energy and potential energy formulation respectively. These entries are composed using Eqs. 3.40 and 3.42 from Section 3.3.1. Thus the unknown coefficients A_{ij}, B_{mn} and C_{mn} can be determined.

$$[\mathbf{K}] \begin{Bmatrix} A_{ij} \\ B_{mn} \\ C_{mn} \end{Bmatrix} = \{\mathbf{F}\} \tag{4.7}$$

4.3 Code Architecture & Flowchart

In this section, the various sections of the theory are presented in the flowchart in Fig. 4.1 to illustrate the procedure as it was programmed using Python in this thesis.

4.4 Results

In this section, the results will be shown for the deflection of three plates under the normal distributed pressure load. First an isotropic plate and VAT laminate without cut-outs will be considered as a means of verification. Furthermore, an isotropic plate will be considered with a cut-out. For this case including a cut-out, a comparison will be made between the amount of terms required to obtain convergence with and without the enriching terms.

4.4.1 Isotropic Plate: Pristine Plate

The first case considered is an isotropic aluminium plate without any discontinuities such as cut-outs. To compare the results from the model presented in this thesis, the Navier analytic method is used. The plate dimensions used, $a \times b$, are 254×254 [mm] with a 1 [mm] thickness. The material properties are $E = 71$ [GPa], $\nu = 0.33$. The applied loading is a unit pressure of 1 [Pa] normal to the plate surface.

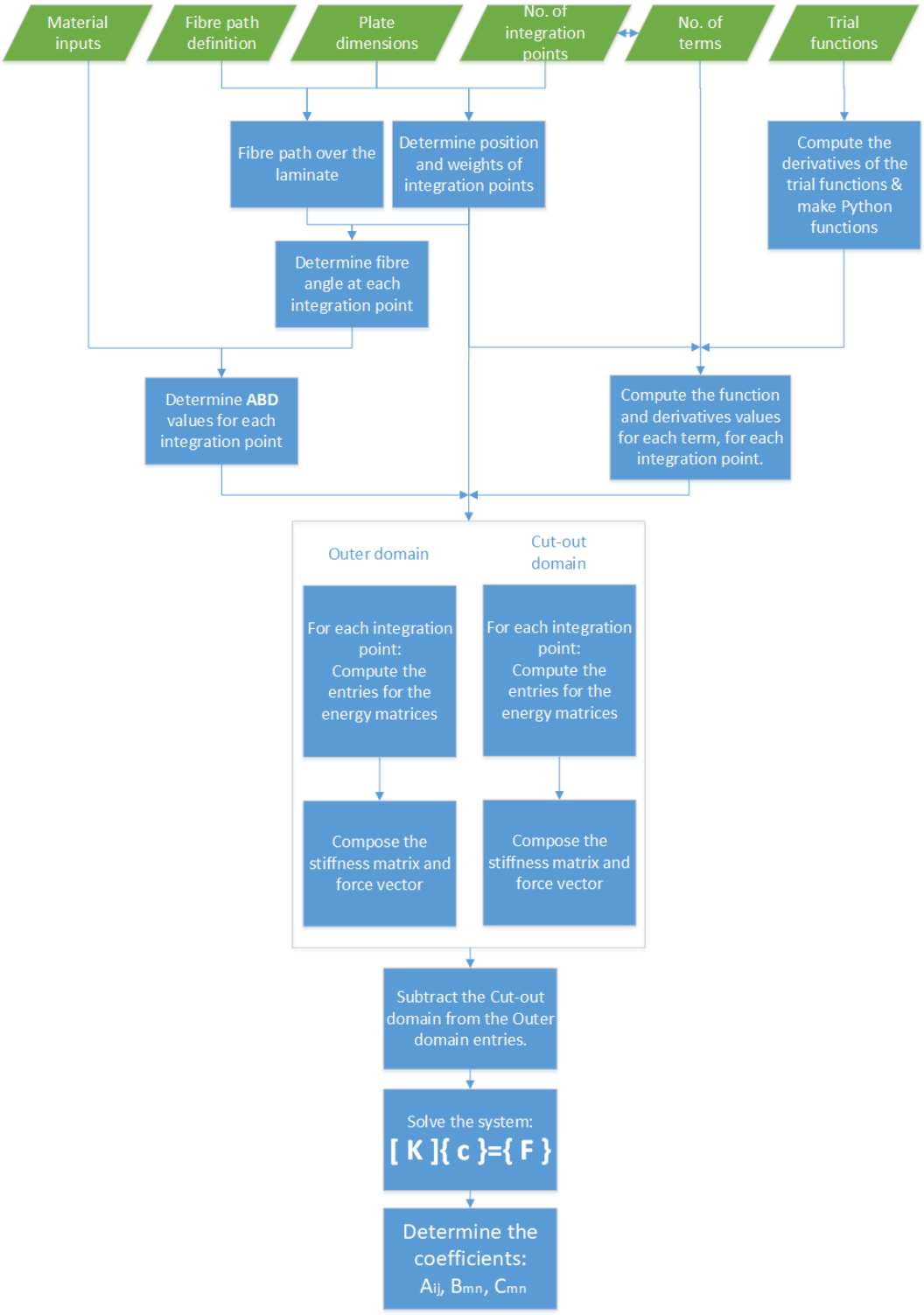

Figure 4.1: Flowchart describing the processes taken in the Python model, each process consists of an implementation of the theory.

The contour plots of the deflections by the Navier method and the present method can be seen in Fig. 4.2. Then, for a more detailed view, the deflection is plotted in 2D along the x-axis at $y = b/2$, which can be seen in Fig. 4.3.

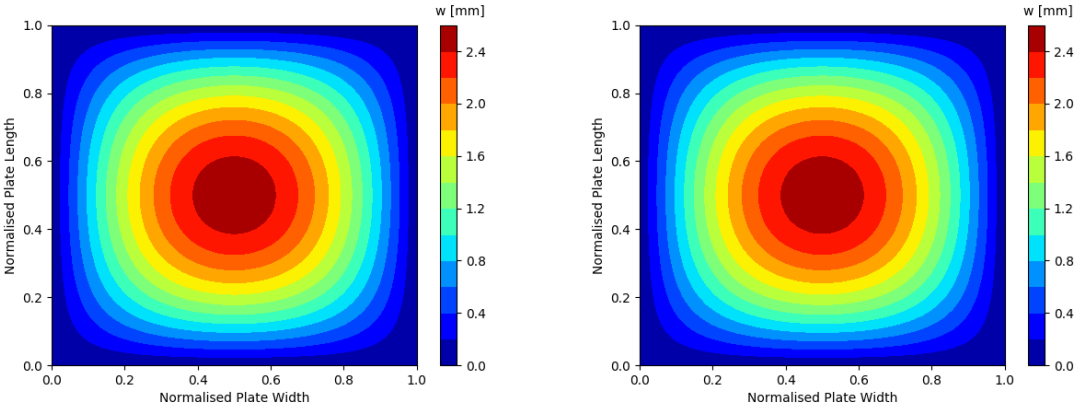

(a) Semi-Analytical Model **(b)** Navier Method

Figure 4.2: Deflection results for a pristine isotropic plate. (a) Results obtained using the present model, (b) results obtained using the Navier Method.

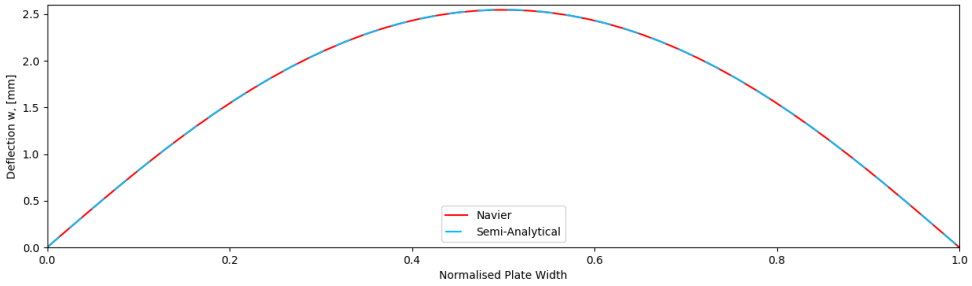

Figure 4.3: Deflection plot of solid isotropic plate. Deflection along x with y constant at $b/2$.

The results can be seen to be in excellent agreement. The results are obtained using only the standard solutions, Eq. 4.4, with $I = J = 6$.

4.4.2 VAT Laminate: Pristine Plate

The next case entails a VAT laminate with a linearly varying fibre path according to the fibre path definition in Eq. 2.1. The fibre angle at the vertical edges, i.e. at normalised plate width $= 0$ and $= 1$, is 0 degrees, thus $T_1 = 0$. The angle at the plate center is 45 degrees, thus $T_0 = 45$. The fibre path can be seen in Fig. 4.4 and the observant reader will note that the path is the same of that shown in Fig. 2.2.
The material properties used are $E_1 = 181$ [GPa], $E_2 = 10.273$ [GPa], $G_{12} = 7.1705$ [GPa], $\nu_{12} = 0.28$ and the lamina thickness $t = 0.127$ [mm]. The laminate has dimensions $a = b = 254$ [mm] and is loaded by a unit pressure of 1 [Pa] normal to its surface. To ensure the VAT

laminate is symmetric and balanced, it is composed of four layers $[\pm\phi(x,y)]_s$. While this will yield a very thin laminate of 0.508 [mm] and it does not comply with the 10% rule, it is only meant as a means of verification and not as a practical application.

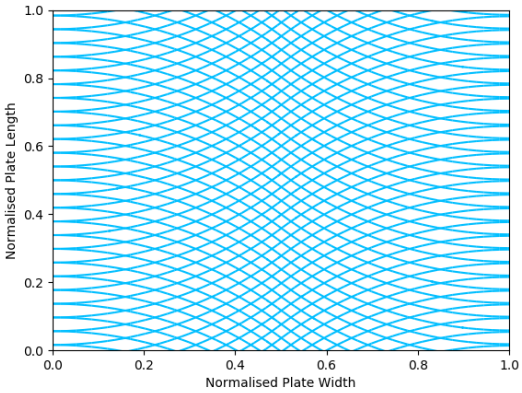

Figure 4.4: Fibre path for $T_0 = 45°$ and $T_1 = 0°$.

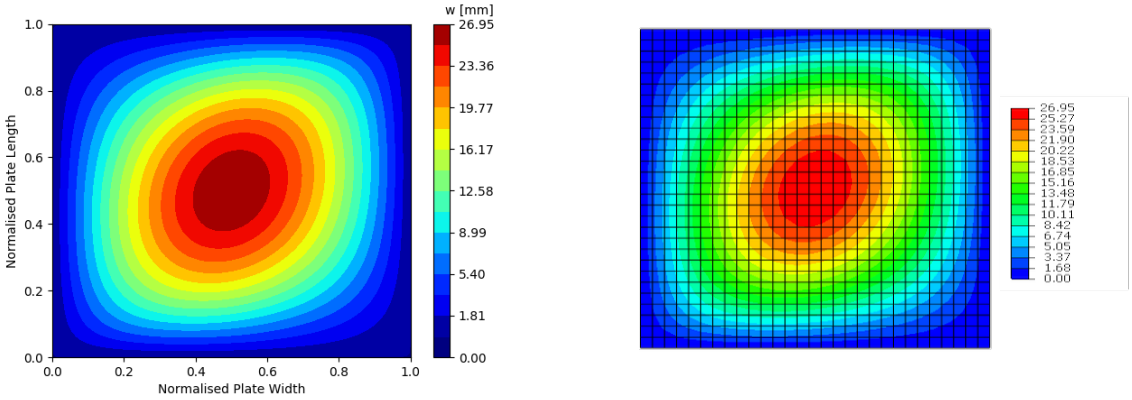

(a) Semi-Analytical **(b)** ABAQUS

Figure 4.5: Deflection results for the VAT plate from Fig. 4.4.

Again, the results are in excellent agreement with ABAQUS. The deflection in this case is obtained using only the standard functions in Eq. 4.4 with $I = J = 10$.

Often, when determining analytical formulations for the out-of-plane behaviour of composite laminates, the bending-twisting coupling terms, D_{16} and D_{26}, are neglected. The semi-analytical approach in this thesis includes these coupling terms with ease so asymmetric results are also included in the solutions. As an example, for the VAT laminate described above the deflection is determined both when including the coupling terms and when neglecting them. The results in Fig. 4.6 show that when neglecting the coupling terms, the result is symmetric similar to the result from an isotropic plate. However, when including the coupling terms, it shows that the solution of minimum potential energy is asymmetric.

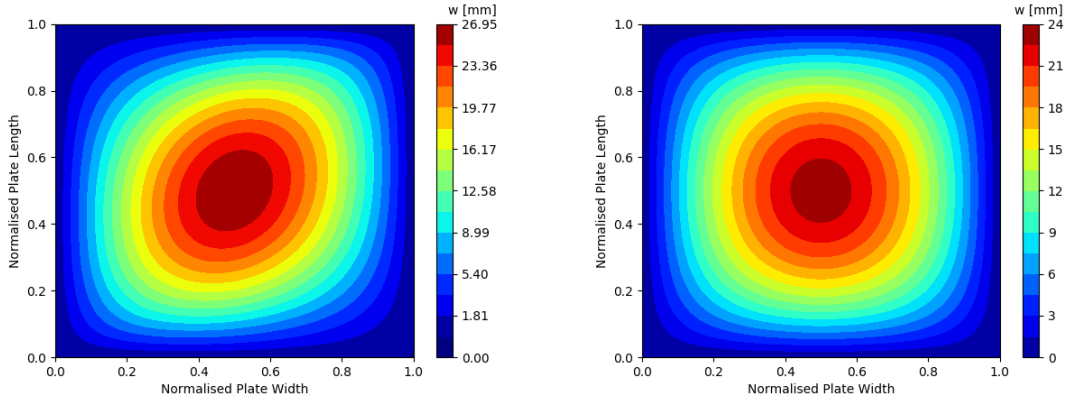

(a) Including D_{16}, D_{26} **(b)** Neglecting D_{16}, D_{26}

Figure 4.6: Deflection results for the VAT plate from Fig. 4.4 showing the consequence of neglecting the coupling terms.

4.4.3 Isotropic Plate: Including Cut-out

Here the deflection results will be shown for an isotropic plate where the plate contains a central located circular hole. The plate dimensions and material properties are the same as those in Section 4.4.1. The plate contains a central located hole circular hole with a radius of 25 [mm]. Here also the enriching functions, Eqs. 4.5 and 4.6, are added. The results from the semi-analytical model are compared to those obtained from the ABAQUS FE software. The results are shown in Fig. 4.7. In Fig. 4.8 again a 2D plot of the deflection along the $x-$axis is plotted along $y = b/2$.

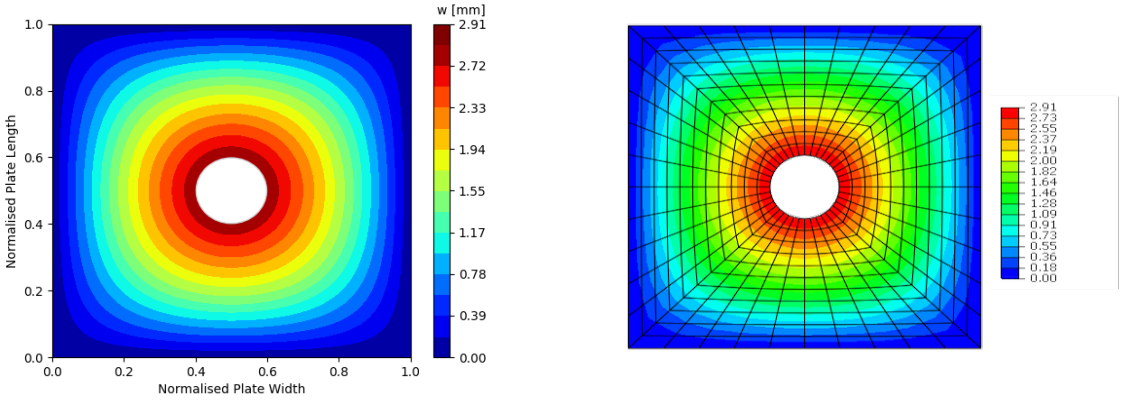

(a) Present model **(b)** ABAQUS

Figure 4.7: Results for an isotropic plate with a central located circular cut-out. Present semi-analytical model vs. ABAQUS finite element software.

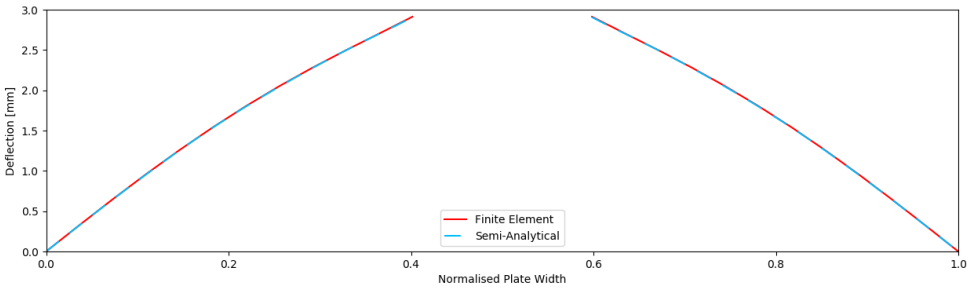

Figure 4.8: Deflection plot of a isotropic plate with circular cut-out. Deflection along x with y constant at $b/2$.

The results from Fig. 4.7 are obtained using both the standard and enriching functions, with $I = J = 6$, $M = 10$ and $N = 0$. In this particular case with a central located hole, the circumferential terms apparently are not required for good convergence. As a consequence, the value of the w_3 functions is always zero due to the sinus term and the system is increased by only 10 degrees of freedom with respect to a plate with no cut-out. More details concerning the convergence behaviour of the method are shown in Appendix A.1.

Number of Terms Required

As mentioned in the above section for the standard functions $I = J = 6$ yields 36 functions, or 36 degrees of freedom, the amount of coefficients to be determined. When using the enriching functions, 10 additional functions are added to find a solution for a total of 46 degrees of freedom.
Here a solution for the plate with a cut-out is approximated using only the standard functions in order to determine if they are able to capture the localised behaviour and determine the amount of terms required to do so. In Fig. 4.9 three plots are shown where different number of terms for the standard solutions are taken. Note that all of these use well over the 46 terms in the enrichment solution without obtaining the same level of agreement with the FE solution.

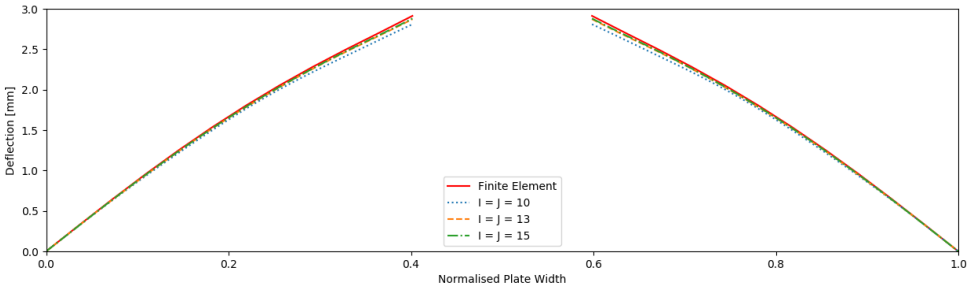

Figure 4.9: Deflection of a isotropic plate using only the standard functions in Eq. 4.4. Using 100, 169 and 225 terms respectively.

Chapter 5

In-Plane Behaviour

In this chapter, the details for the in-plane analysis are presented in a similar fashion as the previous chapter. First, the relevant equations are presented in Section 5.1. However, rather than using the Total Potential Energy as used in Section 3.2.1 the Total Complementary Energy will be used. Second, the trial functions used for the in-plane analysis are presented in Section 5.2. Third, the procedure is visualised in a flowchart in Section 5.3. Finally in Section 5.4, results of various verification cases obtained from literature are showed as well as results for a isotropic plate, VAT laminate and isotropic plate with a circular cut-out.

5.1 Governing Equations

In Section 3.2.1, the strain and potential energy expressions are derived using the TPE, or in terms of the unknowns displacements u, v and w. In this chapter, the TCE will be used to derive the energy expressions. Using the TCE rather than the TPE means that rather than having approximation functions for the displacements u, v and w, the in-plane loads N_x, N_y and N_{xy} must be approximated. Using the Airy stress function the system can then be reduced to a single unknown function to be approximated. Deriving the expression for the strain energy using the TCE is analogous to that derived in section 3.2.1, but rather than using the **ABD** to expand Eq. 3.30, the inverse of the **ABD** is used, indicated by the lowercase letters, the **abd** matrix. With a zero **B** matrix, the in-plane and out-of-plane behaviour can again be decoupled and the strain energy for the in-plane behaviour can be expressed as shown in Eq. 5.1.

$$\begin{aligned} U = &\frac{1}{2}\iint_{\Omega}\left\{a_{11}N_x^2 + 2a_{12}N_xN_y + 2a_{16}N_xN_{xy} + a_{22}N_y^2 + 2a_{26}N_yN_{xy} + a_{66}N_{xy}^2\right\}dx\ dy \\ &+\frac{1}{2}\iint_{\Omega}\left\{d_{11}M_x^2 + 2d_{12}M_xM_y + 2d_{16}M_xM_{xy} + d_{22}M_y^2 + 2d_{26}M_yM_{xy} + d_{66}M_{xy}^2\right\}dx\ dy \end{aligned} \tag{5.1}$$

The load case considered in this chapter is a uni-axial compressive load. The potential energy thus consists of the components from Eq. 3.34 containing N_x.

$$V = -\int_0^b [N_x u]_{x=0}^{x=a} \, dy \tag{5.2}$$

Using the Airy stress function in this analysis yields several advantages. The Airy stress function relates the in-plane loads N_x, N_y and N_{xy} to a single function as shown in Eq. 2.5 and complies with the equilibrium conditions in Eq. 2.4 by definition. Eqs. 2.4 and 2.5 are repeated below for convenience. Another advantage using the Airy stress functions is reducing the number of unknown functions in the energy functional to a single function, thus reducing the size of the system.

$$N_x = \frac{\partial^2 \Phi}{\partial y^2} \qquad N_y = \frac{\partial^2 \Phi}{\partial x^2} \qquad N_{xy} = -\frac{\partial^2 \Phi}{\partial x \partial y}$$

$$\frac{\partial N_x}{\partial x} + \frac{\partial N_{xy}}{\partial y} = 0$$

$$\frac{\partial N_{xy}}{\partial x} + \frac{\partial N_y}{\partial y} = 0$$

The strain energy expression from Eq. 5.1 can be reduced as the stretching and bending parts are decoupled and the in-plane loads can be rewritten in terms of the Airy function to obtain Eq. 5.3.

$$\begin{aligned} U = \frac{1}{2} \iint_A \Big\{ & a_{11} \cdot \Phi_{,yy}^2 + 2a_{12} \cdot \Phi_{,yy} \cdot \Phi_{,xx} - 2a_{16} \cdot \Phi_{,yy} \cdot \Phi_{,xy} + \\ & + a_{22} \cdot \Phi_{,xx}^2 - 2a_{26} \cdot \Phi_{,xx} \cdot \Phi_{,xy} + a_{66} \cdot \Phi_{,xy}^2 \Big\} \, dxdy \end{aligned} \tag{5.3}$$

Similarly, for the potential energy, V, the N_x term is replaced by the Airy stress function.

$$V = -\int_0^b [\Phi_{,yy} \cdot u]_{x=0}^{x=a} \, dy \tag{5.4}$$

Depending on the load case under consideration, the amount of sets of trial functions is chosen. In the case analysed by Kassapglou [5], the laminate was loaded with a uni-axial compressive force. In the work by Wu et al. [9], the VAT laminates were compressed using a uniform compressive displacement. In this thesis, both cases will be examined as both works are used for verification. When considering an applied displacement at the outer vertical edges, the load distribution along these edges will be non-uniform due to the variable stiffness, either due to VAT or the presence of a cut-out. This load distribution is unknown and is approximated using an added set of trial functions, Φ_0. According to the boundary conditions, visualised in Fig. 5.1, N_{xy0} is zero at the vertical edges. This is not necessarily the case for N_y, but the behaviour for N_y near the edges should follow from the choice of trial functions for the entire domain. So the Φ_0 functions are added only to comply with the edge compressive load N_{x0}. They are thus only related to the edge load N_{x0}, i.e. $\Phi_{0,yy} \neq 0$ and $\Phi_{0,xx} = \Phi_{0,xy} = 0$. As the

Φ_0 function only relates to the N_{x0} distribution along the vertical edges, it is only a function of y.

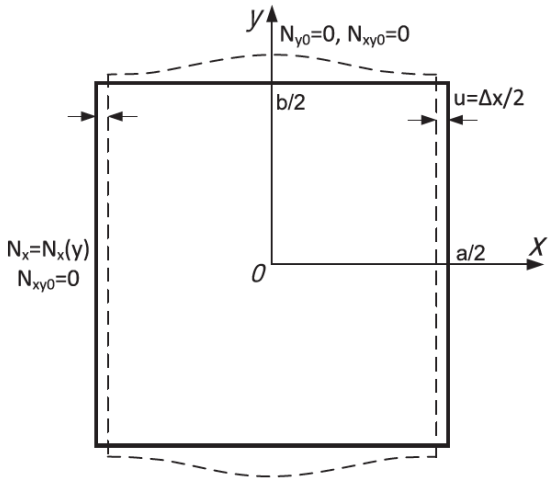

Figure 5.1: The geometry and boundary conditions for the in-plane loading situation, image taken and adapted from [9].

5.2 Trial Functions

Now, trail functions must be chosen for the Airy stress function, Φ. In this thesis, four sets of trial functions are chosen, as shown in Eq. 5.5.

$$\Phi(x,y) = \Phi_0(y) + \Phi_1(x,y) + \Phi_2(x,y) + \Phi_3(x,y) \tag{5.5}$$

Where Φ_0 describes the applied force distribution along the vertical edges of the laminate. Functions Φ_1, Φ_2 and Φ_3 are chosen to describe the behaviour of the plate over the entire domain. As the Φ_0 function is used to comply with the N_{x0} distribution at the vertical edges, the Φ_1, Φ_2 and Φ_3 functions should yield a zero N_x at the vertical edges, while N_y is not necessarily zero. For the transverse edges, the opposite is true. As the transverse edge are allowed to deform freely, they are stress free ($N_{y0} = N_{xy0} = 0$), but N_x is not necessarily zero. In the case of a cut-out, the trial functions should account for the stress-free state at the cut-out edges. The normal stress and tangential shear stress with respect to the cut-out edge should yield a zero result. The sets of trial functions must be chosen with these boundary conditions in mind.
From the literature, the trial functions are chosen so satisfy the natural boundary conditions at the outer edges, but no cut-outs are present and thus no attention is given to the natural boundary conditions at the cut-out edges. This problem was not encountered in Chapter 4, where displacement-based formulations are used with the TPE rather than stress-based formulations with the TCE. The displacement-based formulations only require the trial functions to comply with geometric boundary conditions.
To overcome this problem, the natural boundary conditions at the cut-out edges are elaborated

and conditions are set up for which the trial functions must comply. These conditions are written in detail in Appendix D. However, no trial functions or boundary condition forcing function was found which could comply with the conditions. A different approach is taken, where the thickness of the cut-out region is reduced so that the cut-out region becomes sufficiently weak that is does not carry any load, but still contains material forcing the numerical model to comply with the equilibrium conditions.
The trial functions discussed below thus do not account for the cut-out edges, and only comply with the outer boundary natural boundary conditions.

5.2.1 Legendre Polynomials

For the Φ_0 and Φ_1 functions, the procedure by Wu et al. is adopted, where Legendre polynomials are used. According to Wu, Legendre polynomials are capable to capture local behaviour due to the non-periodic nature of the successive polynomials in contrast to trigonometric functions [9]. Legendre polynomials are defined in the natural coordinates (ξ, η) and are defined as shown in Eq. 5.6. The first 6 terms of the Legendre polynomials are shown in Fig. 5.2.

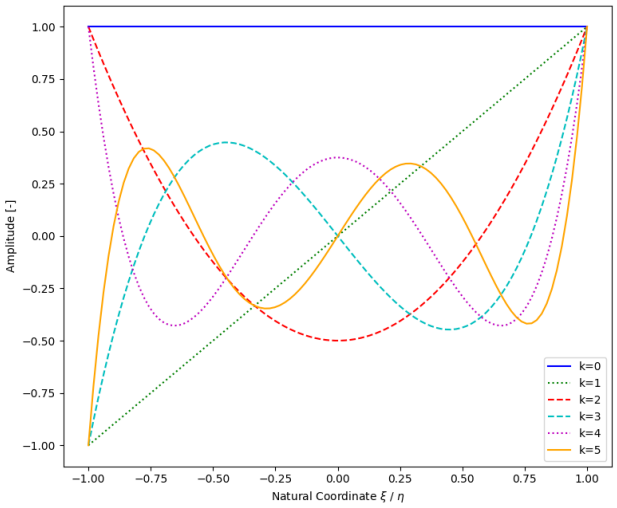

Figure 5.2: First 6 Legendre polynomials plotted in the natural coordinate system (ξ, η).

$$\xi = \frac{2x}{a} - 1 \;\; ; \;\; \eta = \frac{2y}{b} - 1$$

$$\begin{gathered} L_0 = 1, \quad L_1 = \xi, \quad L_2 = \frac{1}{2}(3\xi^2 - 1) \\ (n+1) \cdot L_{n+1} = (2n+1) \cdot \xi \cdot L_n - n \cdot L_{n-1} \end{gathered} \tag{5.6}$$

It has been mentioned that at the vertical edges, the Φ_0 functions only describe the N_{x0} behaviour, e.g. $\Phi_{0,yy}$. Since the functions $\Phi_{0,xx}$ and $\Phi_{0,xy}$ are zero by definition, only the $\Phi_{0,yy}$ functions need to be defined. The series solution is presented in Eq. 5.7.

$$N_{x0} = \Phi_{0_{,yy}} = \sum_{k=0}^{K} c_k \cdot \phi_{0,yy} = \sum_{k=0}^{K} c_k \cdot L_k(y) \tag{5.7}$$

Where L_k are the Legendre polynomials, which are multiplied by unknown coefficients c_k. This definition thus complies with $\Phi_{0,xx}$ and $\Phi_{0,xy}$ being equal to zero. From Fig. 5.2, the first term in the Legendre series solution is a constant. The case where a uniform load is applied rather than a displacement is thus recovered if only a single term is used for Φ_0 function.
The Φ_1 functions are composed of Legendre polynomials also, but now over the (ξ, η) domain. To comply with the stress free conditions described previously and shown in Fig. 5.1, they are multiplied with a boundary condition forcing function. This procedure is again similar to that shown in Chapter 4 and in Eq. 2.6. The Legendre polynomials are multiplied as shown in Eq. 5.8, and the final expression for Φ_1 in Eq. 5.9.

$$\begin{aligned} X_i &= (1-\xi^2)^2 \cdot L_i(\xi) \\ Y_j &= (1-\eta^2)^2 \cdot L_j(\eta) \end{aligned} \tag{5.8}$$

$$\Phi_1 = \sum_{i=0}^{I} \sum_{j=0}^{J} A_{ij} \cdot X_i(\xi) \cdot Y_j(\eta) \tag{5.9}$$

5.2.2 Enriching Trial Functions

Finally, the trial functions Φ_2 and Φ_3 are added with the aim of describing the behaviour surrounding the cut-out. They thus represent the enriching functions in this chapter. These functions varying with respect to the variables r and θ, similar to the enriching functions in Chapter 4. Rather than using a power function for r, here trigonometric series are used for both variables. The Φ_2 and Φ_3 functions are shown in Eqs. 5.10 and 5.11 and similar to the Φ_1 functions, they are multiplied by a boundary condition function, g_ϕ.

$$\Phi_2 = g_\phi(\xi, \eta) \cdot \sum_{m=0}^{M} \sum_{n=0}^{N} B_{mn} \cdot cos(m\pi r) \cdot cos(n\theta) \tag{5.10}$$

$$\Phi_3 = g_\phi(\xi, \eta) \cdot \sum_{m=1}^{M} \sum_{n=1}^{N} C_{mn} \cdot sin(m\pi r) \cdot sin(n\theta) \tag{5.11}$$

$$g_\phi(\xi, \eta) = (1-\xi^2)^2 \cdot (1-\eta^2)^2$$

With the expressions for Φ_0, Φ_1, Φ_2 and Φ_3 defined, these can be input into Eqs. 5.3 and 5.4. The system can then be minimised with respect to the unknown coefficients, set equal to zero

and subsequently solved for the coefficients. The approach as described in section 3.3.1 is followed. Furthermore, both the expressions for U and V also contain Φ_0 with the values of c_k related to the applied displacement. To determine the c_k, the TCE must also be minimised for these coefficients to obtain a system where again there are an equal amount of equations as there are unknowns. Referring back to the assembly of the stiffness matrix in Eq. 3.40, this will be expanded with the minimisation with respect to the coefficients c_k. The system will take the form shown in Eq. 5.12.

$$\begin{bmatrix} \mathbf{K} & \mathbf{K_C} \\ \mathbf{K_C}^T & \mathbf{C} \end{bmatrix} \begin{Bmatrix} \varphi \\ \mathbf{c} \end{Bmatrix} = \begin{Bmatrix} \mathbf{0} \\ \mathbf{Px0} \end{Bmatrix} \tag{5.12}$$

Where the $\mathbf{K}$ entry is the result from the term $\phi_{i\neq 0} \cdot \phi_{i\neq 0}^T$ and resembles the matrix from Eq. 3.40, the $\mathbf{K_C}$ entry is the result from the terms $\phi_{0,yy} \cdot \phi_{(i\neq 0)}^T$ and the $\mathbf{C}$ entry is the results from the term $\phi_{0,yy} \cdot \phi_{0,yy}^T$. On the RHS the vector $\mathbf{Px0}$ is the result from the $\phi_{0,yy}$ terms in the potential energy Eq. 5.4. The vector on the LHS contains the coefficients, where φ resembles the coefficients A_{ij}, B_{mn} and C_{mn}, and $\mathbf{c}$ resembles the coefficients c_k.
For the full derivation of these expressions, see Appendix B.

5.3 Code Architecture & Flowchart

Using the theory described in the previous sections, a solution can be found for plates and (VAT) laminates, with or without cut-outs. In this section a flowchart is used to illustrate how the various sections of theory are incorporated into the final Python-code model. The flowchart can is shown in Fig. 5.3.

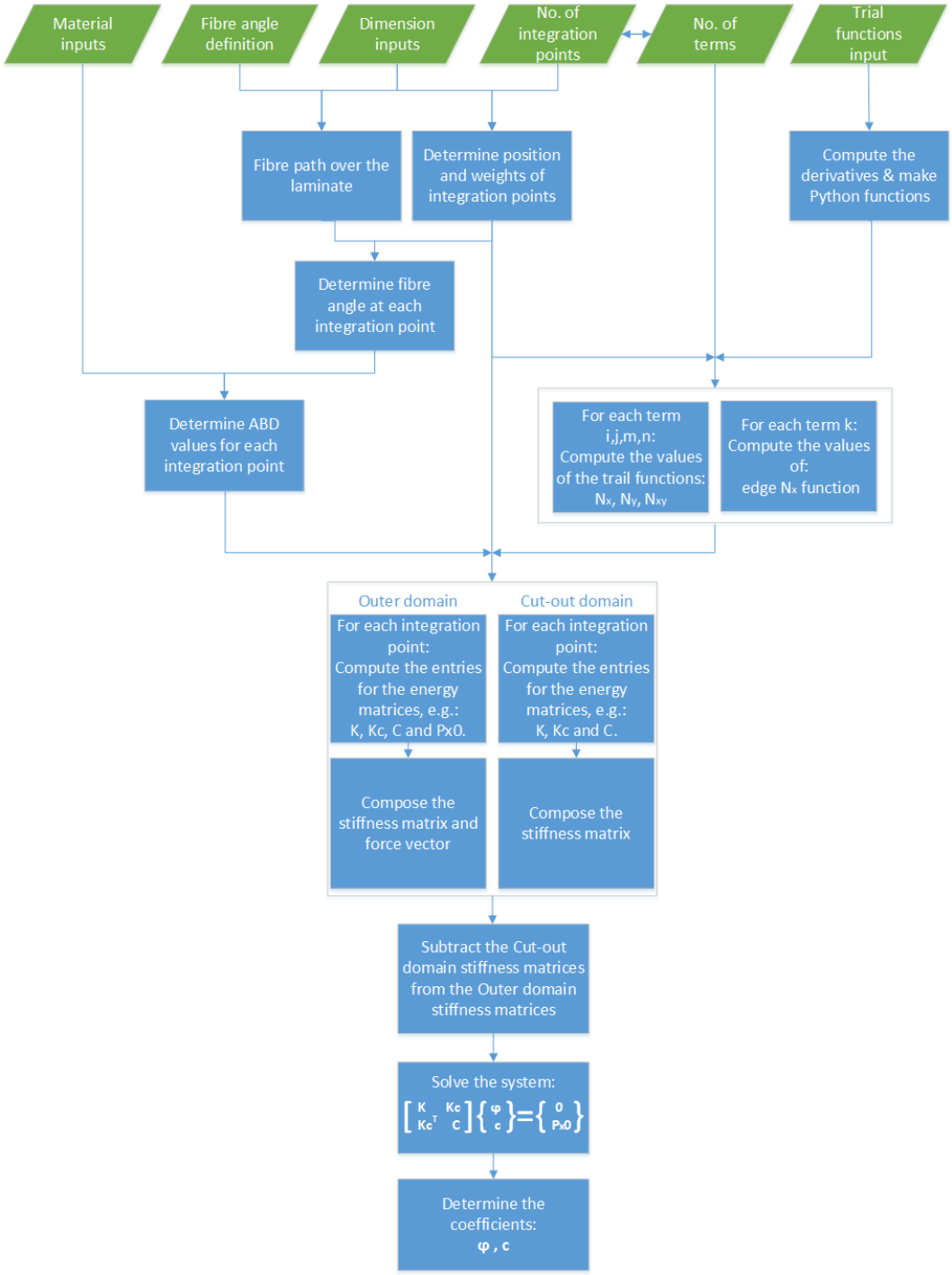

Figure 5.3: Flowchart describing the processes taken in the Python model, each process consists of an implementation of the theory.

5.4 Results

In this section the results will be shown for the in-plane loads. As a means of verification, results from previous authors will be recreated using the model developed in this thesis. First, this considers the case by Kassapoglou [5], where a straight fibre composite with concentric layups is analysed. Second, the case by Wu et al. where a VAT laminate is analysed is recreated. Finally, a cut-out is introduced and analysed for an isotropic plate.

5.4.1 Composite Laminate: Concentric Layups

The results obtained by Kassapoglou [5] are recreated as a means of verification of the numerical method for the in-plane stress-state. In the work, a laminate with concentric layups is considered under uniform applied compressive load. Hence, the analysis as described using a compressive displacement is not yet considered here. A formulation based on the TCE was used, with separate trial functions for N_x, N_y and N_{xy} while still complying to the in-plane equilibrium conditions. Here, the results from Fig. 2.6 are recreated using the same trial functions as Kassapoglou, as shown in Eq. 2.8, repeated below for convenience. The definitions for ξ and η in the formulations is slightly different, ranging from $[0; 1]$ rather than $[-1; 1]$, as can be seen from the definitions below.

$$\xi = \frac{x}{a}; \quad \eta = \frac{y}{b}$$

$$N_x = \overline{N_x} + \sum_{m=1}^{M}\sum_{n=1}^{N} H_{mn}\ \{cos(2m\pi\xi) - 1\}\ cos(2n\pi\eta)$$

$$N_y = \frac{b^2}{a^2}\sum_{m=1}^{M}\sum_{n=1}^{N} \frac{m^2}{n^2} H_{mn}\ cos(2m\pi\xi)\ \{cos(2n\pi\eta) - 1\}$$

$$N_{xy} = \frac{b}{a}\sum_{m=1}^{M}\sum_{n=1}^{N} \frac{m}{n} H_{mn}\ sin(2m\pi\xi)\ sin(2n\pi\eta)$$

The set-up is similar to that shown in Fig. 2.5, considering a square plate with outer dimensions of 508×508 [mm] and three different center patch dimensions 50.8×50.8 [mm], 102×102 [mm] and 254×254 [mm]. The material properties are taken from the reference literature and consist of a plain weave fabric with $E_1 = E_2 = 67.5$ [GPa], $G_{12} = 4.48$ [GPa] and $\nu_{12} = 0.05$. The center layup consisted of layers $[(\pm 45)_5/(0/90)_2/(\pm 45)_5]$ and the perimeter layup of layers $[(\pm 45)/(0/90)_2/(\pm 45)]$.

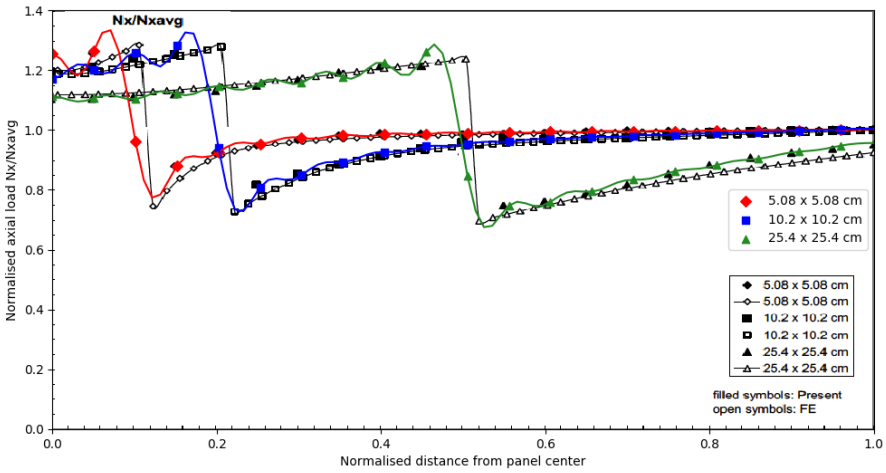

Figure 5.4: Results from [5] including the recreation of the results using the semi-analytical model developed in this thesis. For the number of terms taken in this analysis, $M = N = 30$.

In Fig. 5.4 the results from the present model are plotted on top of the results by Kassapoglou in Fig. 2.6. Good agreement can be seen between the present model and the data markers by Kassapoglou, as is to be expected as the same trial functions are used. Oscillations can be seen close to the edge where the center and perimeter sections meet. This is a consequence of the trial functions being based on trigonometric series. As this may cloud the agreement somewhat, it is believed this is the reason why only marker points are used in the original results presented by Kassapoglou.

These results provided a basis for the model developed in this thesis. The numerical integration methods, described in Section 3.3.2, are used to reshape the rectangular insert to a circular insert, thus acting as a circular stiffer insert. These results are compared to results from FEM and also used to compare the convergence of the trial functions in Eq. 2.8 and those proposed in this thesis in Eqs. 4.4 through 4.6. For the results regarding the stiffened insert, the trial functions proposed in this thesis obtained similar results while using $\approx 30\%$ less terms when compared to the trial functions used in the work by Kassapoglou. Finally, the work is continued further by reducing the stiffness of the circular insert to zero, effectively creating a cut-out. This final result will be elaborated more in section 5.4.3.
Detailed results of the analysis of the square insert, circular insert and comparison of the trial functions in Eq. 2.8 and Eqs. 5.9 to 5.11 are presented in Appendix C.

5.4.2 VAT Laminate: Pristine Plate

In this section work from literature regarding VAT laminates will be recreated as a further means of verification. The work performed by Wu et al. considering a pristine VAT laminate loaded via a uniform compressive displacement is recreated here [9]. Referring back to the trial functions used in this chapter, only the Φ_0 and Φ_1 will be used as there is no discontinuity.

According to the Airy stress function, the expressions for N_x, N_y and N_{xy} will become those in Eq. 5.13.

$$\begin{aligned} N_x &= \Phi_{0,yy} + \Phi_{1,yy} = \sum_{k=0}^{K} c_k \cdot L_k + \sum_{i,j=0}^{IJ} A_{ij} \cdot X_i \cdot Y_{j,yy} \\ N_y &= \Phi_{1,xx} = \sum_{i,j=0}^{IJ} A_{ij} \cdot X_{i,xx} \cdot Y_j \\ N_{xy} &= -\Phi_{1,xy} = -1 \cdot \sum_{i,j=0}^{IJ} A_{ij} \cdot X_{i,x} \cdot Y_{j,y} \end{aligned} \tag{5.13}$$

With these expressions the entries for Eq. 5.12 can be calculated and the problem can be solved. The laminate under consideration is the same as in Section 4.4.2 with a linear fibrepath definition, using the expression from Eq. 2.1 with $T_0 = 45°$ and $T_1 = 0°$. The material properties used are again $E_1 = 181$ [GPa], $E_2 = 10.273$ [GPa], $G_{12} = 7.1705$ [GPa], $\nu_{12} = 0.28$ and the lamina thickness $t = 0.127$ [mm]. The laminate has dimensions $a = b = 254$ [mm] and is loaded by a unit compressive displacement $\Delta_x = 1$ [mm]. To ensure the VAT laminate is symmetric and balanced, it is composed of four layers $[\pm\phi(x, y)]_s$.
With the laminate defined the results for the load distributions N_x, N_y and N_{xy} can be determined. In Fig. 5.5, the results from the semi-analytical model are shown. The verification results from ABAQUS use the double symmetry property of the laminate to increase the node density in the model. For the semi-analytical model this is an unneccessary step, as the degrees of freedom depend on the number of trial functions, rather than the laminate dimensions and nodes, which is one of the benefits of the method. The N_x and N_y plots from ABAQUS and the semi-analytical model are compared in Figs. 5.6 and 5.7. For these results, the equations from Eq. 5.13 are used with $I = J = K = 8$, for a total of 90 degrees of freedom.

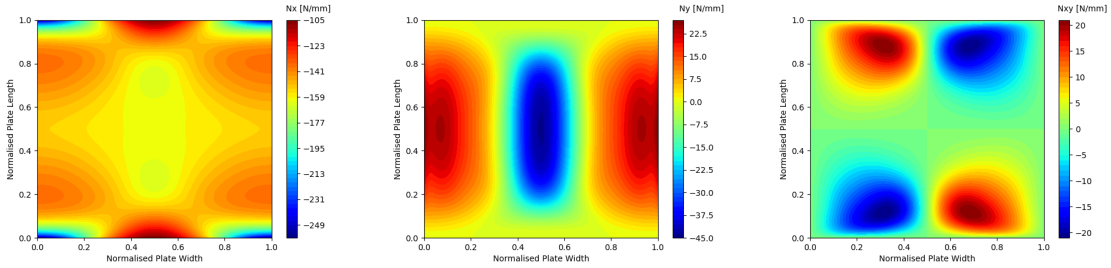

(a) N_x **(b)** N_y **(c)** N_{xy}

Figure 5.5: The load distribution for the VAT laminate under a uniform compressive displacement, $\Delta_x = 1$ [mm]. Obtained using the present semi-analytical model.

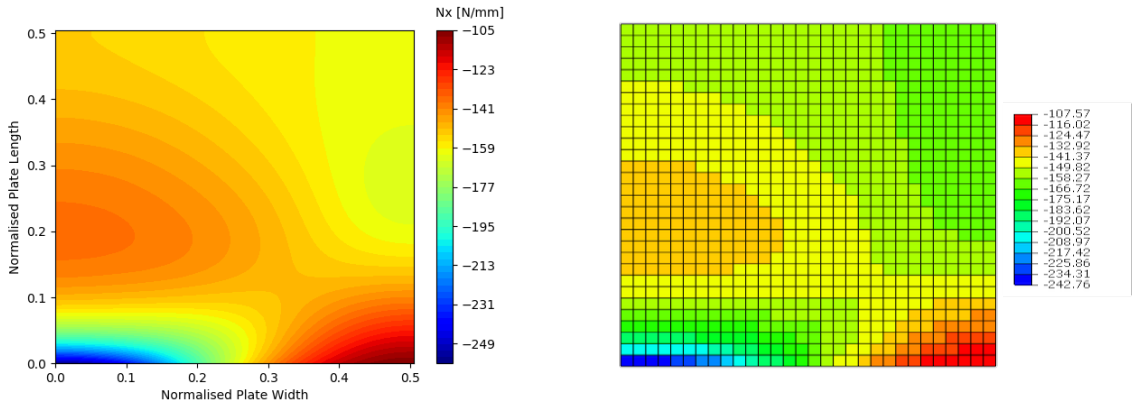

(a) Semi-Analytical **(b)** ABAQUS

Figure 5.6: The N_x distribution of the VAT laminate, semi-analytical results vs. ABAQUS using double symmetry of the laminate

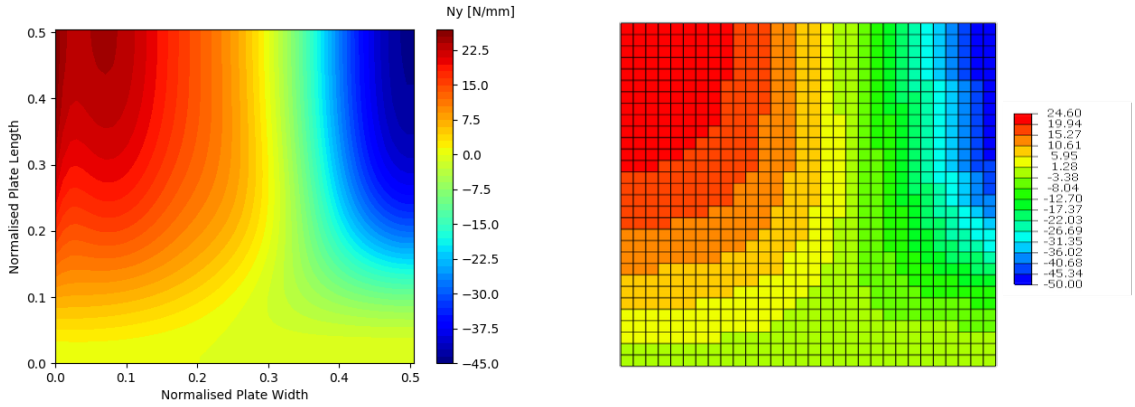

(a) Semi-Analytical **(b)** ABAQUS

Figure 5.7: The N_y distribution of the VAT laminate, semi-analytical results vs. ABAQUS using double symmetry of the laminate

As can be seen from Figs. 5.6 and 5.7, the ABAQUS model shows a discrete distribution of the in-plane loads, as it determines the loads from the displacements between nodes. To improve this, more nodes are required. However, in the ABAQUS student edition a limit of 1000 nodes applies. In the results shown a grid of 31×31 nodes is created for a total of 961 nodes. With 5 degrees of freedom per node, 4805 degrees of freedom are already used. The results shown using the semi-analytical model are obtained using 90 degrees of freedom, or $1,87\%$ compared to the FE number of degrees of freedom.

5.4.3 Isotropic Plate: Including Cut-Out

The next case covers the same plate as in Section 4.4.3, an isotropic plate with a central located circular cut-out. The approach is analogous to that discussed at the end of Section

5.4.1 where the stiffness of the central located patch is reduced to zero. However when doing so, the results did not match those obtained from FEM.
In Section 5.2 it was mentioned that the trial functions must comply also with the stress-state at the cut-out boundaries. While this is not the case for the trial functions introduced in Sections 5.2.1 and 5.2.2, the subject of reducing the thickness of the cut-out region has been introduced in Section 5.2. As mentioned, the thickness of the cut-out region will be reduced in order to force the numerical model to comly with the equilibrium conditions. The thickness value of the cut-out region is expressed as a percentage of the perimeter thickness and named the residual thickness. A comparison is made for the results when varying the residual thickness of the cut-out region. This comparison study is shown in Appendix E. The final value for the residual thickness is 2% of the perimeter thickness.

For the analysis, the material properties and plate dimensions are again $E = 71$ [GPa], $\nu = 0.33$, $t = 1$ [mm], $a = b = 254$ [mm] and $R = 25$ [mm]. The trial functions include all functions described in the previous sections, Eqs. 5.7, 5.9, 5.10 and 5.11 with $I = J = K = 8$, $M = 39$ and $N = 5$ yielding a total of 524 terms, or degrees of freedom.
The in-plane load distribution N_x, N_y and N_{xy} are shown in Figs. 5.8 to 5.10.

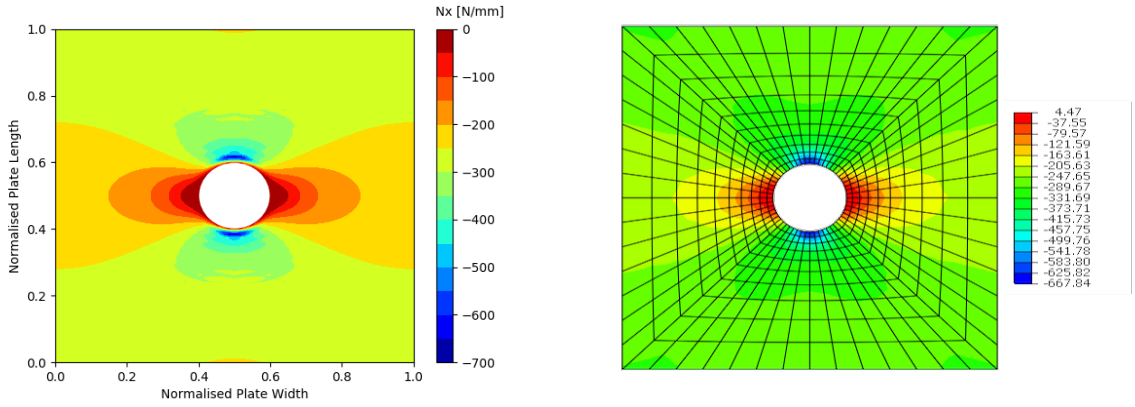

(a) Semi-Analytical **(b)** ABAQUS

Figure 5.8: N_x load distribution for the isotropic plate with a cut-out. Semi-analytical vs. ABAQUS.

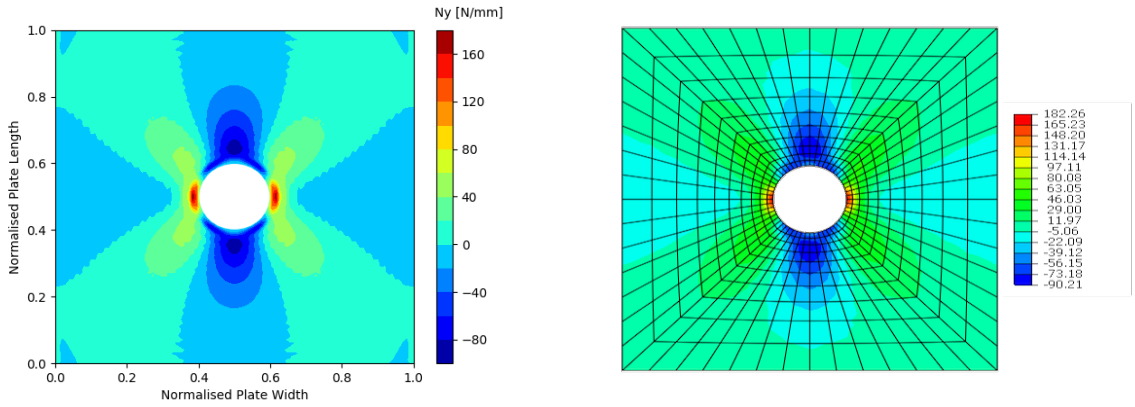

(a) Semi-Analytical **(b)** ABAQUS

Figure 5.9: N_y load distribution for the isotropic plate with a cut-out. Semi-analytical vs. ABAQUS.

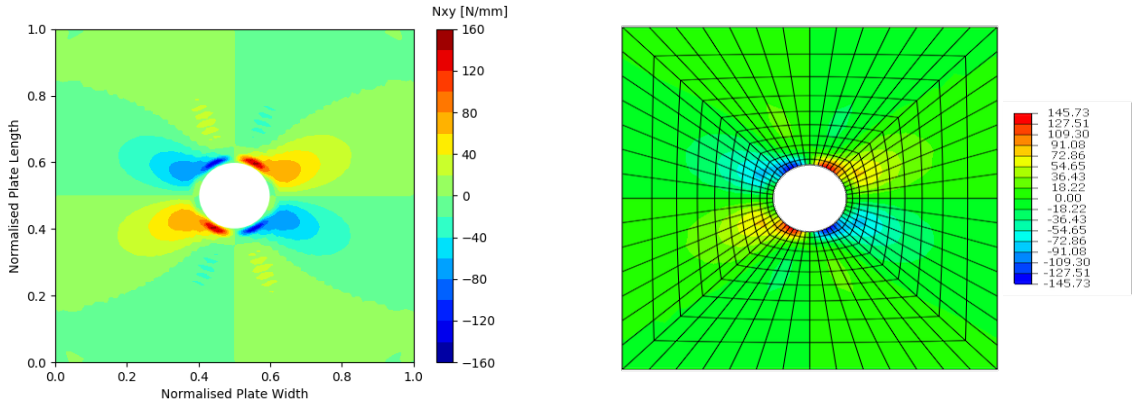

(a) Semi-Analytical **(b)** ABAQUS

Figure 5.10: N_{xy} load distribution for the isotropic plate with a cut-out. Semi-analytical vs. ABAQUS.

The loads along different paths on the laminate are plotted in 2D to illustrate the agreement and differences between the finite element and semi-analytical results. The paths are plotted alongside the plots for convenience.

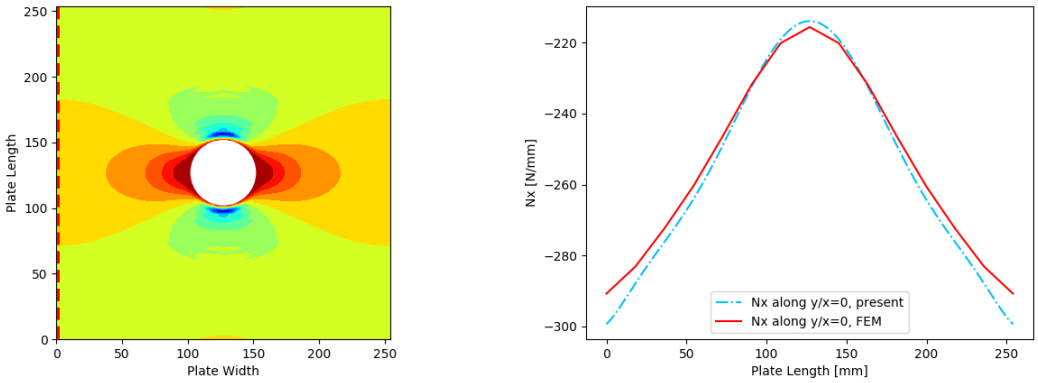

Figure 5.11: The N_x distribution along y at $x = 0$, results from the semi-analytical model vs. ABAQUS finite element results.

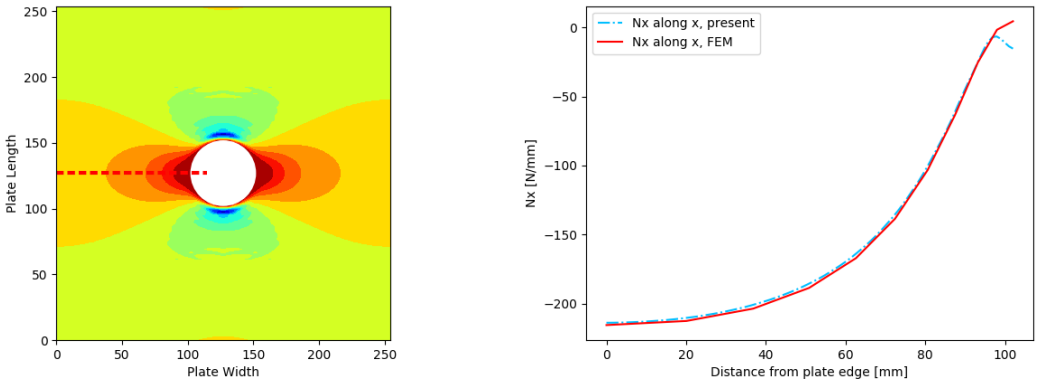

Figure 5.12: The N_x distribution along x at $y = b/2$, results from the semi-analytical model vs. ABAQUS finite element results.

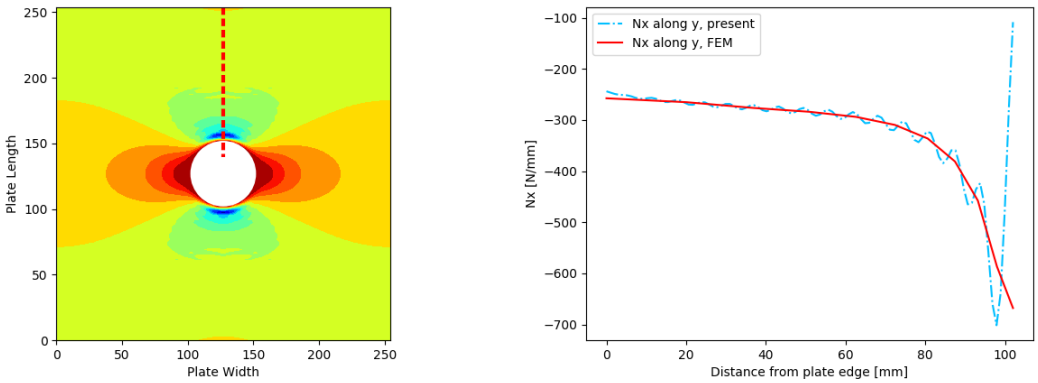

Figure 5.13: The N_x distribution along y at $x = a/2$, results from the semi-analytical model vs. ABAQUS finite element results.

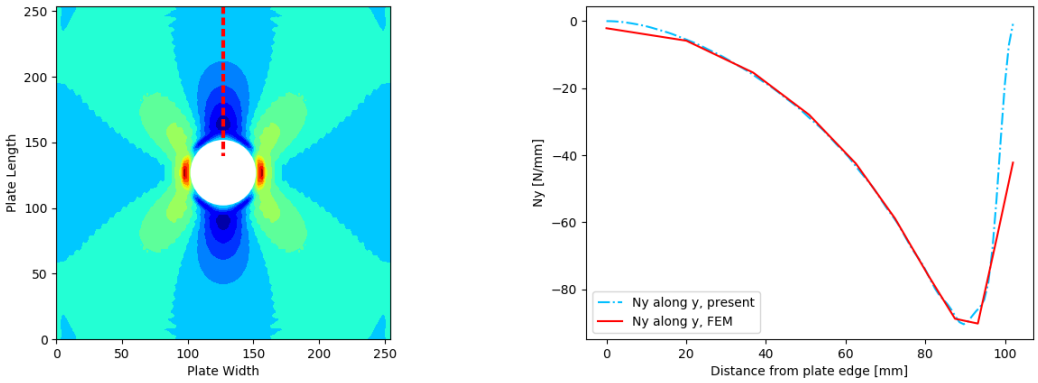

Figure 5.14: The N_y distribution along y at $x = a/2$, results from the semi-analytical model vs. ABAQUS finite element results.

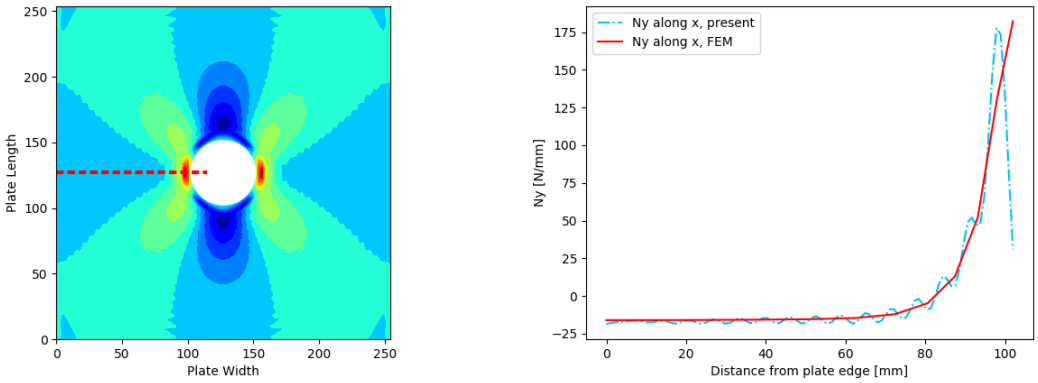

Figure 5.15: The N_y distribution along x at $y = b/2$, results from the semi-analytical model vs. ABAQUS finite element results.

From the figures, the consequence of the residual thickness can be seen. Due to the residual material, the method will show zero loads inside the cut-out area. Where the loads tend to agree with this statement, i.e. Fig. 5.12 and Fig. 5.14, the lines are in good agreement. However close to the cut-out edge where the loads are not zero, i.e. Fig. 5.13 and Fig. 5.15, oscillations can be seen similar to those in the analysis by Kassapoglou in Fig. 5.4. This is a consequence of the trigonometric trial functions that will approach zero for the region inside the cut-out. The results however give a good approximation of the stress concentrations at those locations and are deemed accurate enough to continue with a buckling analysis, as for buckling the in-plane stress fields only have an average influence on the buckling analysis [9]. The convergence behaviour of the results in Figs. 5.11 through 5.14 is shown in Appendix A.2.

As a comparative study the results from above are also obtained using the trial functions from Eq. 2.8. From this comparison it was concluded that the trial functions proposed in this thesis give a more accurate representation of the stress-state while using less terms. For

the present model the results showed above are used with 524 terms of degrees of freedom, compared to 909 terms for the trial functions from Eq. 2.8. The comparison is presented in more detail in Appendix C.4.

Chapter 6

Buckling

In this chapter, the buckling analysis will be performed. This entails the coupling of the out-of-plane and in-plane behaviour, discussed in Chapters 4 and 5 respectively, to obtain the stability behaviour of various laminates. For the buckling analysis, first the relevant equations will be discussed in Section 6.1. The procedure is visualised again using a flowchart in Section 6.2 before finally showing results in Section 6.3. The applications under consideration are a pristine VAT laminate and an isotropic plate with a circular cut-out.

6.1 Governing Equations

In Chapter 3 it was explained that the linear strain equations are taken and as a consequence the in-plane behaviour and out-of-plane behaviour are decoupled. In this chapter this coupled behaviour is investigated, and thus the linear mid-plane strain equations for ϵ_{x0}, ϵ_{y0} and γ_{xy0}, presented in Eq. 3.32, are not sufficient. The non-linear mid-plane strain equations are required, which are derived in the textbook by Kassapoglou when deriving the Von Karman equations for large deflections of plates [1]. These non-linear strain equations are shown in Eq. 6.1 and will provide the required coupling between the in-plane loads and out-of-plane deflection. The expressions for the curvatures κ_x, κ_y and κ_{xy} of the plate will remain the same.

$$\begin{aligned} \epsilon_{x0} &= \frac{\partial u}{\partial x} + \frac{1}{2}\left(\frac{\partial w}{\partial x}\right)^2 \\ \epsilon_{y0} &= \frac{\partial v}{\partial y} + \frac{1}{2}\left(\frac{\partial w}{\partial y}\right)^2 \\ \gamma_{xy0} &= \frac{\partial u}{\partial y} + \frac{\partial v}{\partial x} + \left(\frac{\partial w}{\partial x}\right)\left(\frac{\partial w}{\partial y}\right) \end{aligned} \tag{6.1}$$

During buckling, it is assumed that there is no stretching or shearing of the mid-plane of the plate. This yields zero mid-plane strains, ϵ_{x0}, ϵ_{y0} and γ_{xy0}. Furthermore, it is assumed that

up to the buckling point, the in-plane displacements u and v are negligible and thus zero. When these assumptions are input into Eq. 3.31, they yield that the strain energy expression remains the same with respect to that of the out-of-plane model, in Eq. 4.1.

$$U = \frac{1}{2}\iint_{\Omega} \begin{Bmatrix} D_{11}\left(\frac{\partial^2 w}{\partial x^2}\right)^2 + 2D_{12}\,\frac{\partial^2 w}{\partial x^2}\frac{\partial^2 w}{\partial y^2} + 4D_{16}\,\frac{\partial^2 w}{\partial x^2}\frac{\partial^2 w}{\partial x \partial y} \\ +D_{22}\left(\frac{\partial^2 w}{\partial y^2}\right)^2 + 4D_{26}\frac{\partial^2 w}{\partial y^2}\frac{\partial^2 w}{\partial x \partial y} + 4D_{66}\left(\frac{\partial^2 w}{\partial x \partial y}\right)^2 \end{Bmatrix} dx\ dy$$

In Chapter 5, the potential energy was taken as the applied force multiplied with the edge displacement. Here it is assumed that the edge displacement is negligible upon the buckling point and this would yield zero as a result. Looking at the complete expression for the potential energy in Eq. 3.34, repeated here for convenience, the second and third terms in this equation are related to the edge displacements and will yield zero.

$$\begin{aligned} V = &-\iint_{\Omega} \{p_x u + p_y v + p_z w\}\ dx\ dy \\ &-\int_0^b \left[N_x u + N_{xy} v + Q_x w - M_x\left(\frac{\partial w}{\partial x}\right)\right]_{x=0}^{x=a} dy \\ &-\int_0^a \left[N_{xy} u + N_y v + Q_y w - M_y\left(\frac{\partial w}{\partial y}\right)\right]_{y=0}^{y=b} dx \end{aligned}$$

The first term in the expression is the summation of the displacement over the entire domain and is examined more closely. With the thin-plate and plane stress assumptions still valid, thus $p_z = 0$, only p_x and p_y remain. Following the procedure by Kassapoglou, the equilibrium equations in Eq. 2.4 can be substituted for p_x and p_y [1].

$$\iint_{\Omega} \{p_x u + p_y v\}\, dx\ dy = \iint_{\Omega} \left\{\left(-\frac{\partial N_x}{\partial x} - \frac{\partial N_{xy}}{\partial y}\right) u + \left(-\frac{\partial N_{xy}}{\partial x} - \frac{\partial N_y}{\partial y}\right) v\right\} dx\ dy$$

The RHS of this equation can be integrated by parts.

$$\begin{aligned} \iint_{\Omega} \{p_x u + p_y v\}\, dxdy &= \int_0^b \left\{[-N_x u - N_{xy} v]_{x=0}^{x=a} + \int_0^a \left[N_x \frac{\partial u}{\partial x} + N_{xy}\frac{\partial v}{\partial x}\right] dx\right\} dy \\ &+ \int_0^a \left\{[-N_{xy} u - N_y v]_{y=0}^{y=b} + \int_0^b \left[N_{xy}\frac{\partial u}{\partial y} + N_y \frac{\partial v}{\partial y}\right] dy\right\} dx \\ &= \int_0^a [-N_{xy} u - N_y v]_{y=0}^{y=b}\, dx + \int_0^b [-N_x u - N_{xy} v]_{x=0}^{x=a}\, dy \\ &+ \iint_{\Omega} \left[N_x \frac{\partial u}{\partial x} + N_{xy}\frac{\partial v}{\partial x} + N_{xy}\frac{\partial u}{\partial y} + N_y \frac{\partial v}{\partial y}\right] dx\ dy \end{aligned} \tag{6.2}$$

In the first two terms in Eq. 6.2 the edge loads and displacements are recovered, while in the third term the load distribution over the entire plate area is shown, which is multiplied with

the derivative of their respective displacement. The first two terms are thus neglected, as the assumption still holds that the edge displacements are negligible. Eq. 6.1 is then used to relate the derivatives of the in-plane displacements u and v to the out-of-plane displacement w. As the assumption is made that the mid-plane strains remain zero during buckling, the expressions in Eq. 6.1 are equal to zero, leading to the relations in Eq. 6.3.

$$\begin{aligned} \frac{\partial u}{\partial x} &= -\frac{1}{2}\left(\frac{\partial w}{\partial x}\right)^2 \\ \frac{\partial v}{\partial y} &= -\frac{1}{2}\left(\frac{\partial w}{\partial y}\right)^2 \\ \frac{\partial u}{\partial y} + \frac{\partial v}{\partial x} &= -\left(\frac{\partial w}{\partial x}\right)\left(\frac{\partial w}{\partial y}\right) \end{aligned} \tag{6.3}$$

Combining the last term in Eq. 6.2 with Eq. 6.3 and Eq. 3.34, assuming only in-plane loads N_x, N_y and N_{xy} leads to the final expression for the potential energy in Eq. 6.4.

$$V = \frac{1}{2}\iint_{\Omega}\left\{N_x\left(\frac{\partial w}{\partial x}\right)^2 + N_y\left(\frac{\partial w}{\partial y}\right)^2 + 2N_{xy}\left(\frac{\partial w}{\partial x}\right)\left(\frac{\partial w}{\partial y}\right)\right\} dx\ dy \tag{6.4}$$

Minimising the potential energy with respect to the unknown coefficients in the trial functions for w will result in a matrix rather than a vector compared to the out-of-plane deflection case, as the potential energy is related to the derivatives of the deflection w squared. This will result in an eigenvalue problem as defined in Eq. 6.5.

$$[\mathbf{K} + \lambda\mathbf{F}]\{c\} = 0 \tag{6.5}$$

In Eq. 6.5 the parameter λ denotes the eigenvalues, $\boldsymbol{K}$ is the stiffness matrix resulting from the minimisation of strain energy Eq. 4.1 and $\boldsymbol{F}$ is the matrix resulting from the minimisation of the potential energy in Eq. 6.4. The inputs for N_x, N_y and N_{xy} in the potential energy are obtained from the in-plane load distribution discussed in Chapter 5. As the eigenvalues λ are in relation to the applied loading, they resemble the applied compressive displacement required for buckling in this analysis.

6.2 Code Architecture & Flowchart

In the flowchart in Fig. 6.1, the process is illustrated. It can be seen that the in-plane load distributions are obtained from the in-plane model and input into the potential energy calculations. The procedure regarding the strain energy are similar to that in the out-of-plane procedure, but here the problem yields an eigenvalue problem. In the Python implementation the eigenvalue problem is solved using the $scipy - linalg$ package.

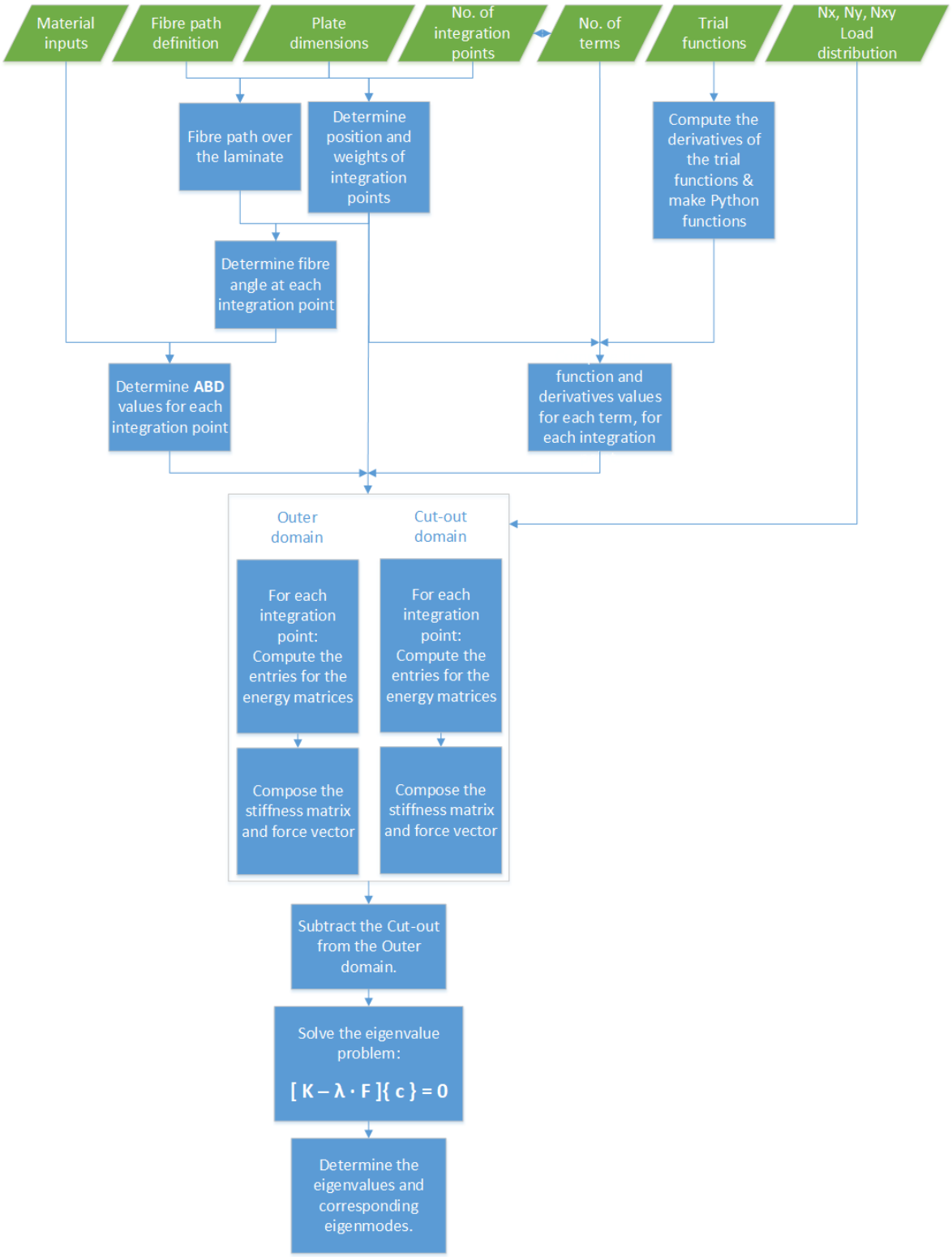

Figure 6.1: Flowchart describing the processes taken in the Python model, each process consists of an implementation of the theory.

6.3 Results

Here the buckling results will be presented. Both the eigenvalues and eigenmodes for several types of plates/laminates are shown. Again, as a means of verification, VAT laminates are considered without cut-outs. Then the isotropic plate with a cut-out will be analysed using the present semi-analytical model and compared to ABAQUS finite element results.

6.3.1 VAT Laminate: Pristine Plate

The VAT laminate previously analysed in Chapters 4 and 5 is considered once more, the material and laminate properties thus remain the same. The in-plane loads are obtained from Chapter 5 and the deflection functions from Chapter 4. For this case, as there is no cut-out, only the standard solution functions Eq. 4.4 are used with $I = J = 15$. The number of terms taken is higher than in Chapter 4 as here multiple eigenmodes are computed which can have more complex shapes. The first five eigenmodes are shown in Figs. 6.2 to 6.6. From the figures, the importance of including the D_{16} and D_{26} is clear as the eigenmodes are asymmetric. The corresponding eigenvalues are shown in Tab. 6.1.

Table 6.1: Eigenvalues for solid VAT laminate with $T_0 = 45°$ and $T_1 = 0°$ under uniform compressive displacement.

Mode no.	Eigenvalues		Difference [%]
	Semi-Analytical	ABAQUS	
1	0.00228	0.00228	0.00
2	0.00540	0.00544	0.74
3	0.00893	0.00903	1.11
4	0.00924	0.00929	0.54
5	0.01284	0.01310	1.98

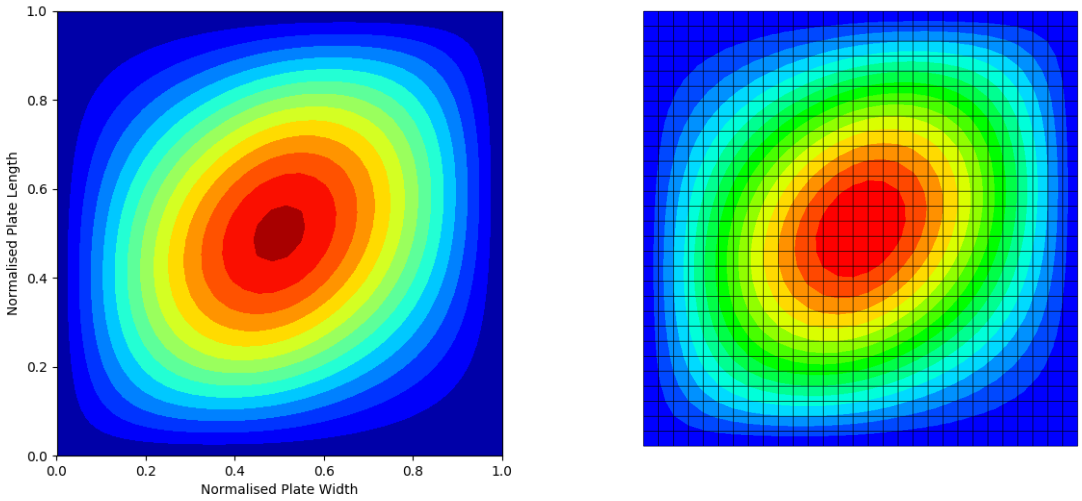

(a) Semi-Analytical **(b)** ABAQUS

Figure 6.2: Eigenmode no. 1 for the solid VAT laminate. Semi-analytical vs. ABAQUS.

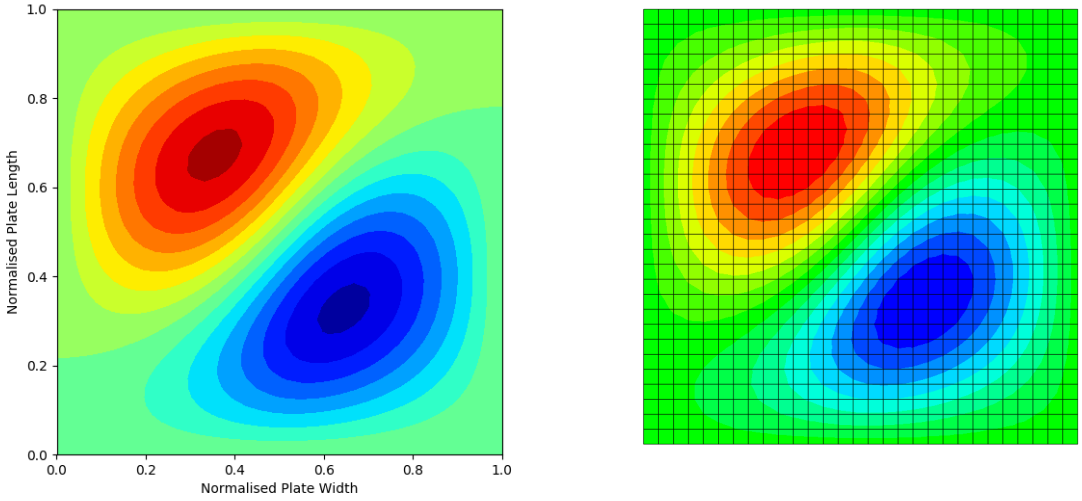

(a) Semi-Analytical **(b)** ABAQUS

Figure 6.3: Eigenmode no. 2 for the solid VAT laminate. Semi-analytical vs. ABAQUS.

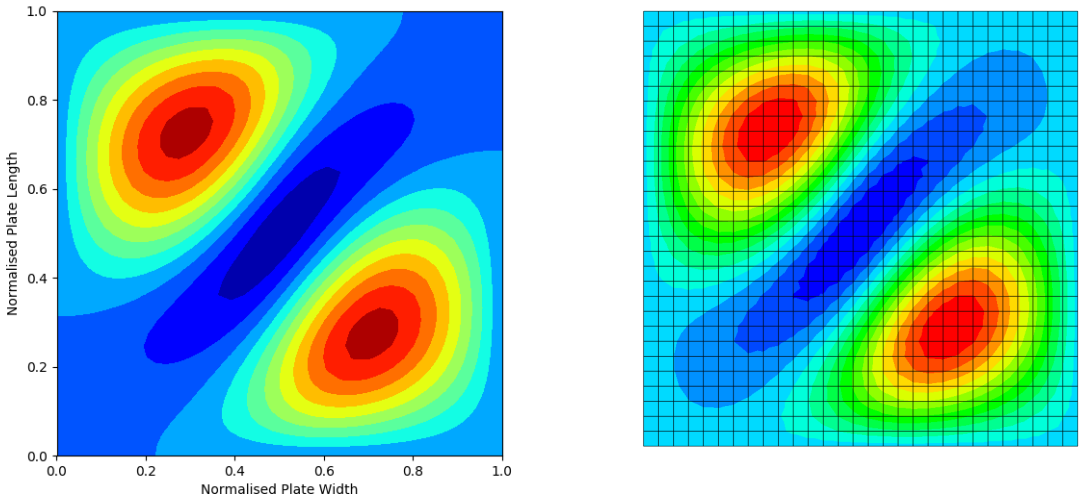

(a) Semi-Analytical **(b)** ABAQUS

Figure 6.4: Eigenmode no. 3 for the solid VAT laminate. Semi-analytical vs. ABAQUS.

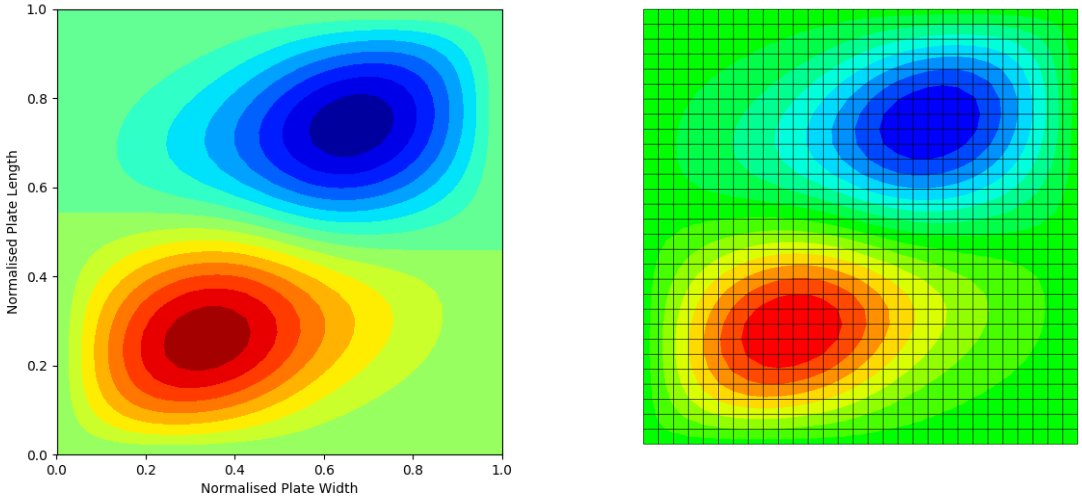

(a) Semi-Analytical **(b)** ABAQUS

Figure 6.5: Eigenmode no. 4 for the solid VAT laminate. Semi-analytical vs. ABAQUS.

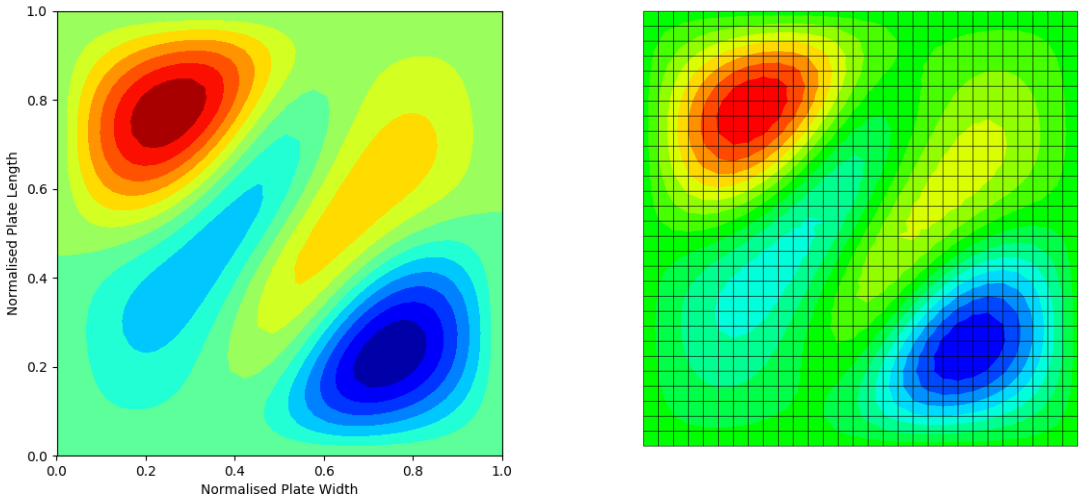

(a) Semi-Analytical **(b)** ABAQUS

Figure 6.6: Eigenmode no. 5 for the solid VAT laminate. Semi-analytical vs. ABAQUS.

The results can be seen to be in good agreement, which is to be expected as the method is obtained from literature and thus the present semi-analytical model can be deemed verified for buckling of solid VAT laminates.

6.3.2 Isotropic Plate: Including Cut-Out

Here the isotropic plate containing a central located circular cut-out is analysed for buckling. The in-plane loads are obtained from Chapter 5 and the deflection functions from Chapter 4. Similar to the previous results, more terms are included with respect to the out-of-plane results in Chapter 4 to account for the buckling shapes of higher order buckling modes. While for the deflection in Chapter 4 only radial terms were sufficient, for buckling the circumferential terms are also important for the higher order mode shapes, as they contain fluctuations around the circumference of the cut-out. The total number of terms taken for the analysis below are $I = J = 6$ and $M = N = 10$ for a total number of 246 terms. The first five eigenmodes are shown in Figs. 6.7 to 6.11. The corresponding eigenvalues are shown in Tab. 6.2.

Table 6.2: Eigenvalues for isotropic plate containing a cut-out under uniform compressive displacement.

Mode no.	Eigenvalues		Difference [%]
	Semi-Analytical	ABAQUS	
1	0.01448	0.01427	1.47
2	0.02676	0.02630	1.75
3	0.04318	0.04302	0.37
4	0.05729	0.05742	0.23
5	0.06156	0.06098	0.95

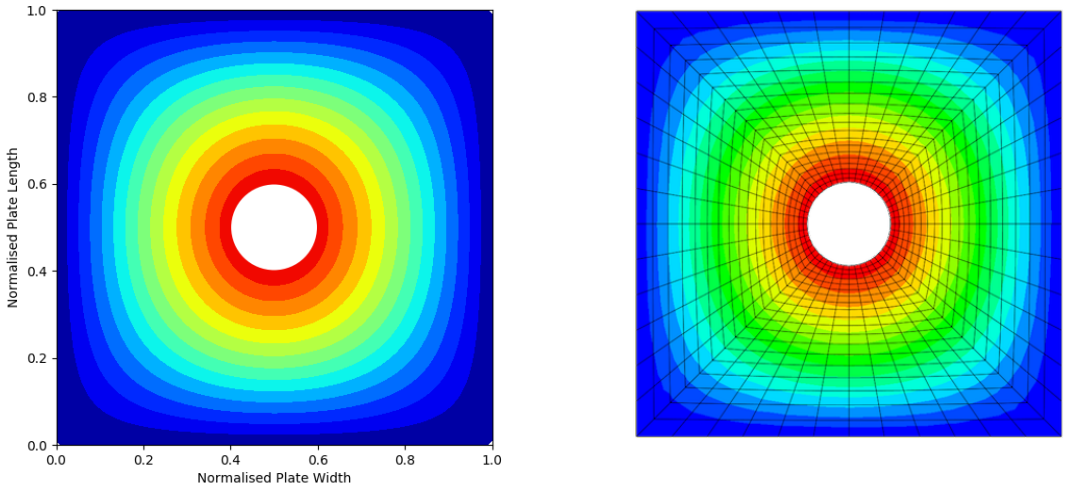

(a) Semi-Analytical **(b)** ABAQUS

Figure 6.7: Eigenmode no. 1 for the isotropic plate with cut-out. Semi-analytical vs. ABAQUS.

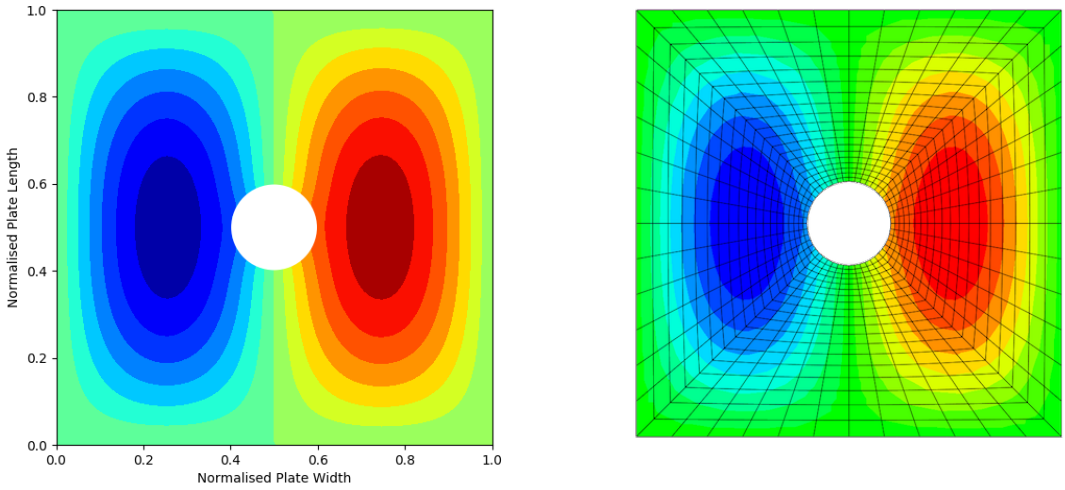

(a) Semi-Analytical **(b)** ABAQUS

Figure 6.8: Eigenmode no. 2 for the isotropic plate with cut-out. Semi-analytical vs. ABAQUS.

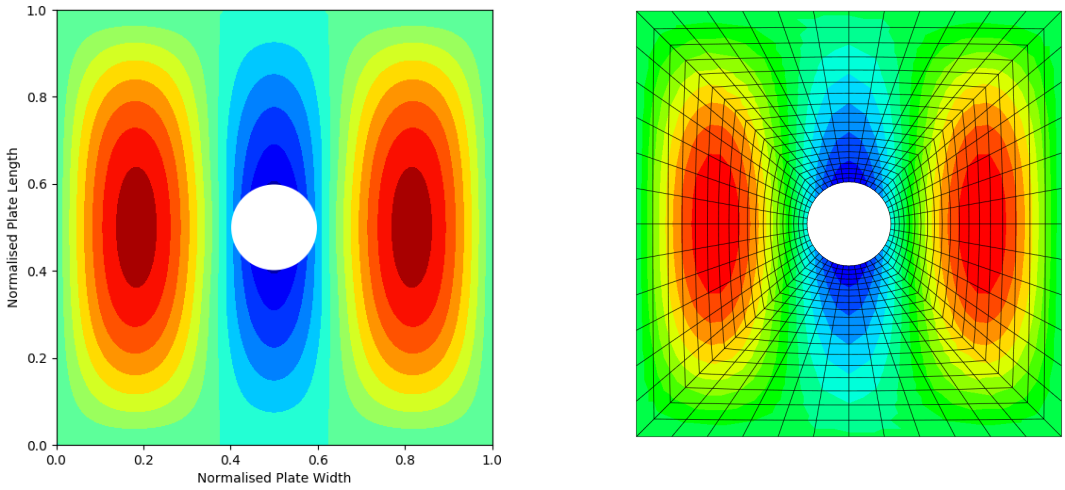

(a) Semi-Analytical **(b)** ABAQUS

Figure 6.9: Eigenmode no. 3 for the isotropic plate with cut-out. Semi-analytical vs. ABAQUS.

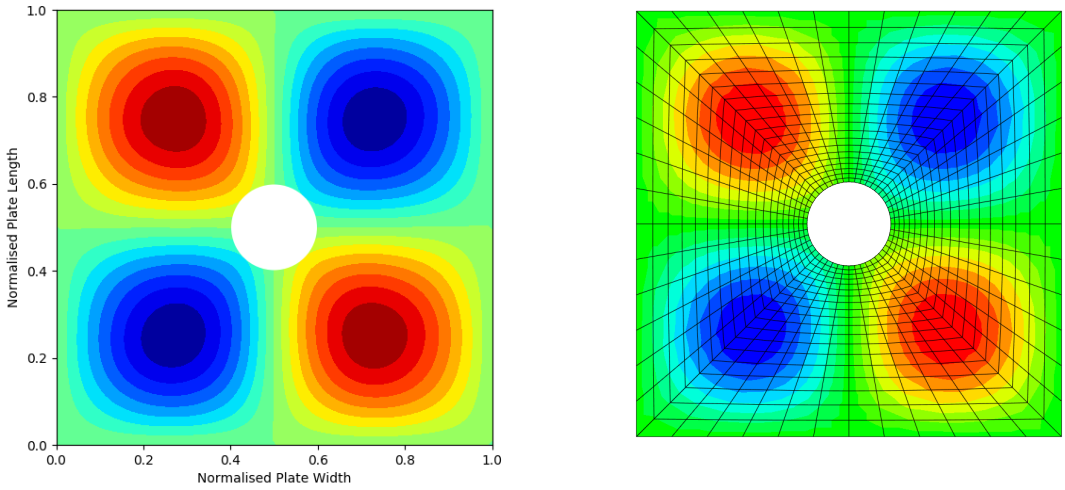

(a) Semi-Analytical **(b)** ABAQUS

Figure 6.10: Eigenmode no. 4 for the isotropic plate with cut-out. Semi-analytical vs. ABAQUS.

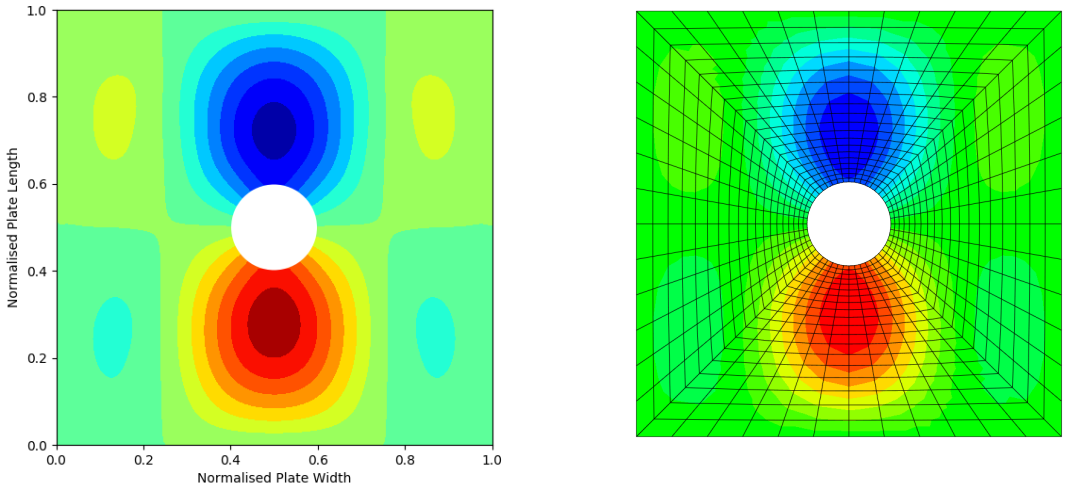

(a) Semi-Analytical **(b)** ABAQUS

Figure 6.11: Eigenmode no. 5 for the isotropic plate with cut-out. Semi-analytical vs. ABAQUS.

From the the table and the figures, the results can be seen to be in good agreement. This illustrates that the semi-analytical model is able to predict the buckling behaviour very well. Furthermore, it confirms that the oscillations seen in the stress-field in Chapter 5 do not cause large discrepancies in the buckling results, confirming the statement that they are considered in an average sense. This is also confirmed in the sensitivity study in Appendix E where the buckling eigenvalues are given for the various residual thickness' considered where more oscillations are present. The convergence behaviour of the buckling values with respect to the number of terms taken is shown in Appendix A.3.

Chapter 7

VAT Design

In this chapter, a design case will be discussed that illustrates both the capabilities of the model presented and of VAT laminates with cut-outs. The design is chosen such that the in-plane loads are distributed away from the cut-out, thus reducing stress concentrations. This is also done in an effort to reduce the decrease in buckling load once a cut-out is introduced. The laminate under consideration is a square laminate with a linear fibre orientation distribution. First in Section 7.1 the fibre path orientation is discussed, then in Section 7.2 the in-plane load distribution is determined based on a compressive displacement. Finally, in Section 7.3 the buckling results are presented.

7.1 VAT Laminate Design

Based on the knowledge obtained from literature, a smart choice can be made with respect to the fibre orientation. It is known that loads tend to follow stiffness in a structure. It is also known that beyond the buckling point, the in-plane loads tend to shift towards the edges of the laminate. This is confirmed by the designs found in literature in Chapter 2 such as the design by Biggers & Srinivasan [2]. The research by Hyer & Lee also confirm this, and subsequently shows having stiffness away from the hole edge and more towards the laminate edge increases the buckling load for a laminate with a cut-out, see Figs. 2.11b and 2.12 [8]. With this information, a fibre orientation can be chosen to fulfil these criteria. For convenience the linear fibre orientation is used and the orientation is rotated by 90° with respect to the examples used until now. This is noted as $[90\pm < T_0|T_1 >]$. A layup of $[90\pm < 0|75 >]_s$ is chosen for the laminate. The material properties and laminea thickness are the same as used before for VAT laminates. The fibre path are shown in Fig. 7.1.

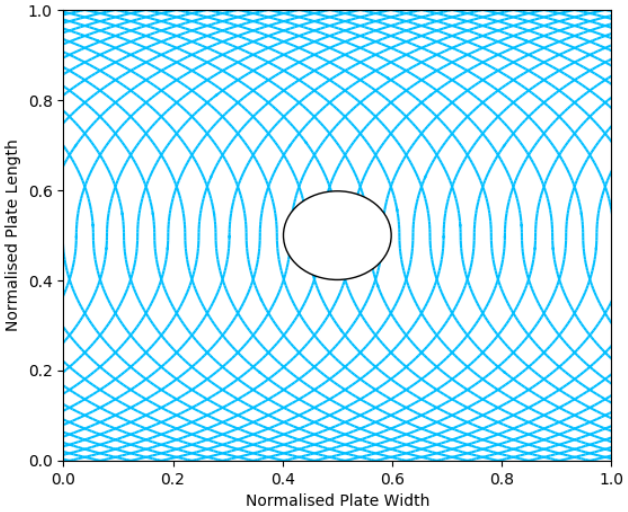

Figure 7.1: Fibrepath for the laminate using Eq. 2.1 for layup $[90\pm < 0|75 >]_s$.

7.2 In-Plane Results

Using the model from Chapter 5, the in-plane load distribution is determined for the VAT laminate under a uniform compressive displacement, $\Delta_x = 1$ [mm]. For the analysis, the same number of terms are taken compared to the analysis in Chapter 5, $I = J = K = 8$, $M = 39$ and $N = 5$. The load distributions for the entire plate determined with the present model are shown in Figs. 7.2 to 7.4.

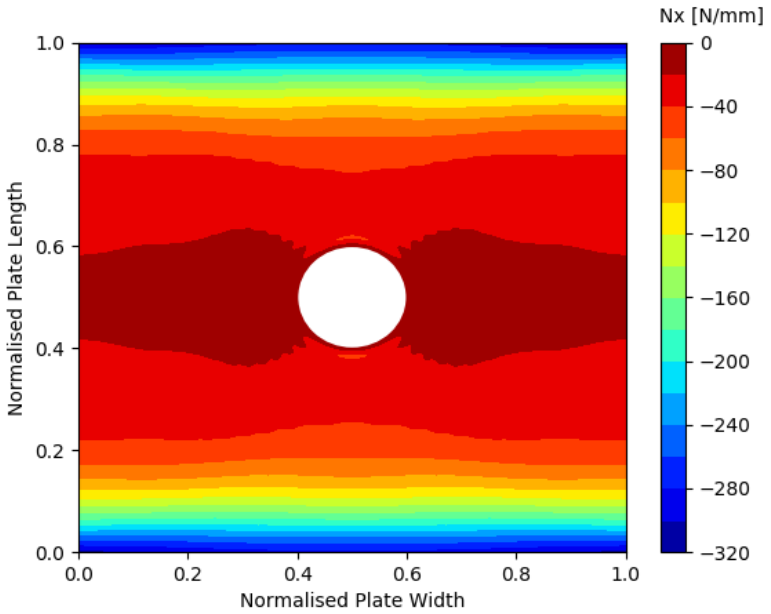

Figure 7.2: N_x distribution for the $[90\pm < 0|75 >]_s$ VAT laminate, under uniform compressive displacement.

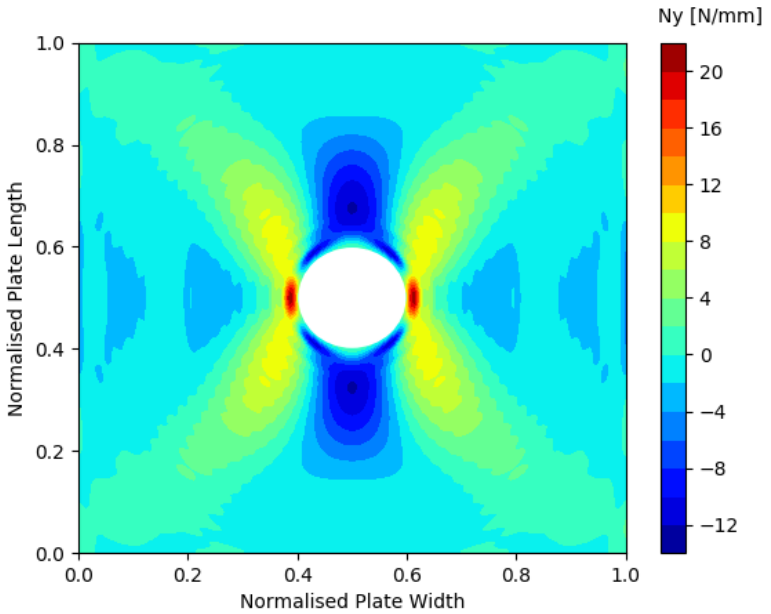

Figure 7.3: N_y distribution for the $[90\pm < 0|75 >]_s$ VAT laminate, under uniform compressive displacement.

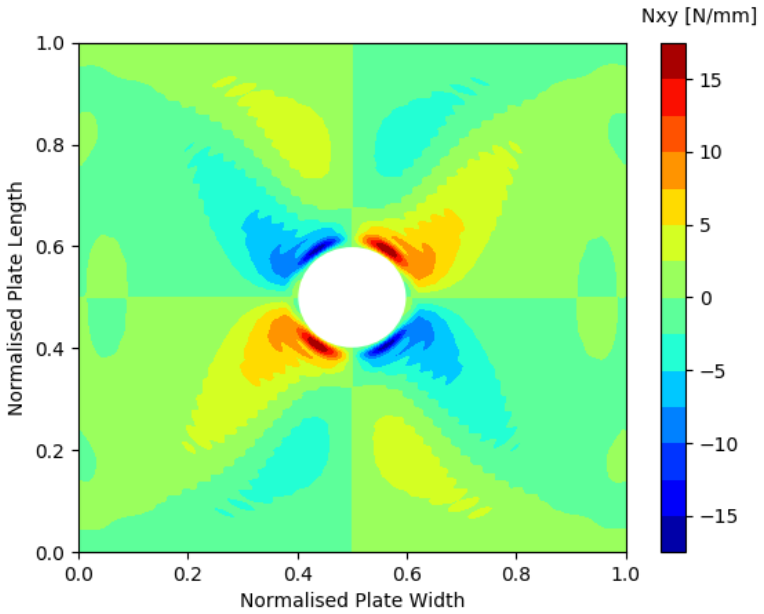

Figure 7.4: N_{xy} distribution for the $[90\pm < 0|75 >]_s$ VAT laminate, under uniform compressive displacement.

To compare with FE results, the double symmetry is again used. These results are shown side-by-side in Figs. 7.5 to 7.7. The FE model is composed using a university ABAQUS license, allowing more nodes, in this model 3600 nodes are used. Due to the variable stiffness of every element in the mesh, a input generation file is used which was only able to consider rectangular shaped elements. Because of this, the FE results are rather coarse near the cut-out edge. Furthermore, the FE input file could not exclude the elements inside the cut-out region. The approach in ABAQUS is thus to decrease the thickness and stiffness of the cut-out elements such that they do not contribute to the in-plane load carrying capability. This occasionally does lead to high stress peaks in the elements near the cut-out edge.

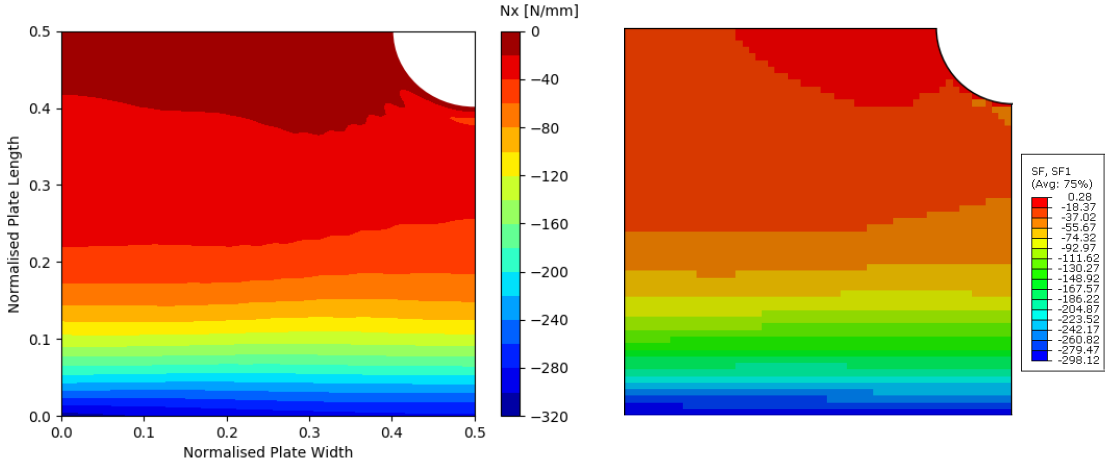

(a) Semi-Analytic **(b)** ABAQUS

Figure 7.5: Comparison of N_x load distribution, semi-analytical vs. ABAQUS.

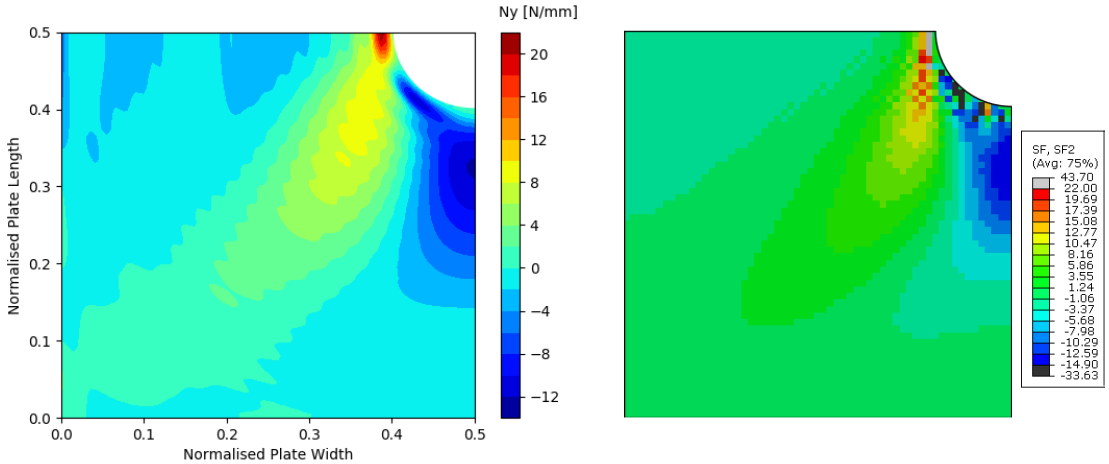

(a) Semi-Analytic **(b)** ABAQUS

Figure 7.6: Comparison of N_y load distribution, semi-analytical vs. ABAQUS.

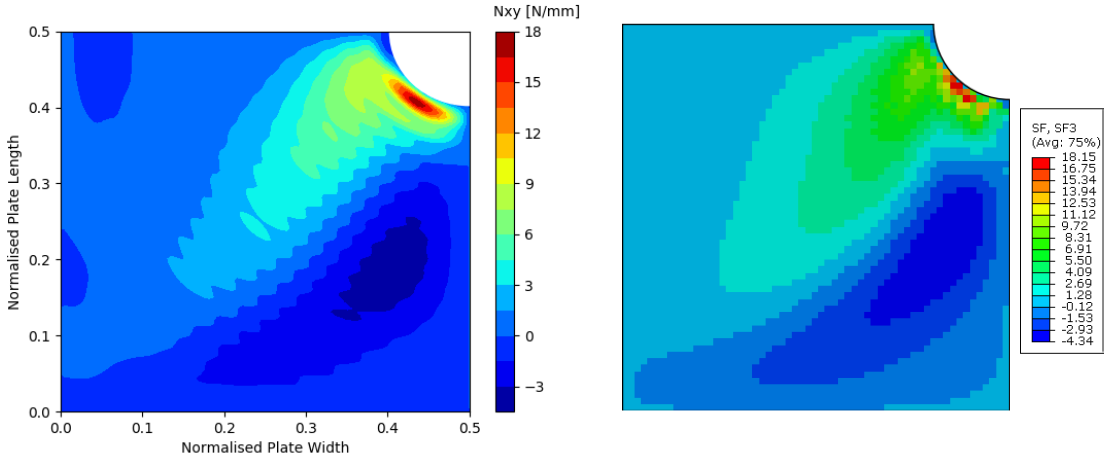

(a) Semi-Analytic **(b)** ABAQUS

Figure 7.7: Comparison of N_{xy} load distribution, semi-analytical vs. ABAQUS.

For a more detailed comparison, the N_x and N_y distributions along different paths is plotted in 2D similar to Chapter 5. These results are shown in Figs. 7.8 to 7.12.

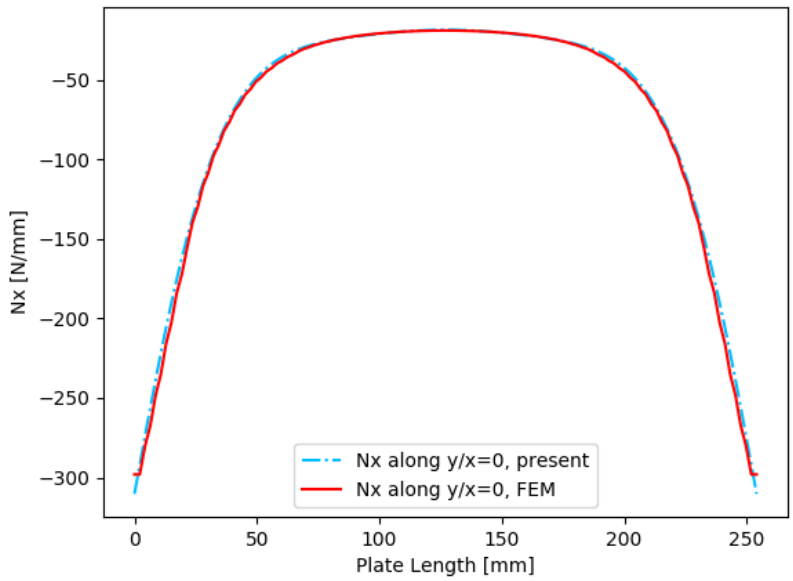

Figure 7.8: N_x distribution along y, $x = 0$ for the $[90\pm < 0|75 >]_s$ VAT laminate, under uniform compressive displacement

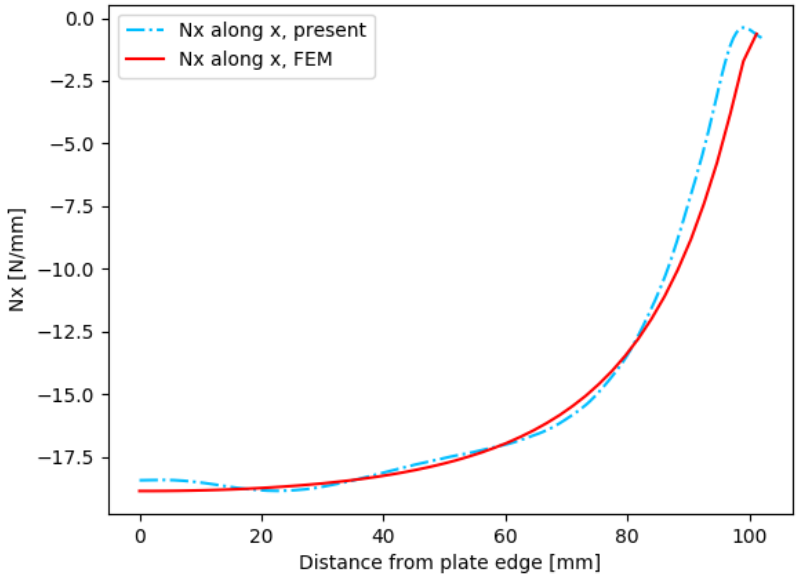

Figure 7.9: N_x distribution along x, $y = b/2$ for the $[90\pm < 0|75 >]_s$ VAT laminate, under uniform compressive displacement

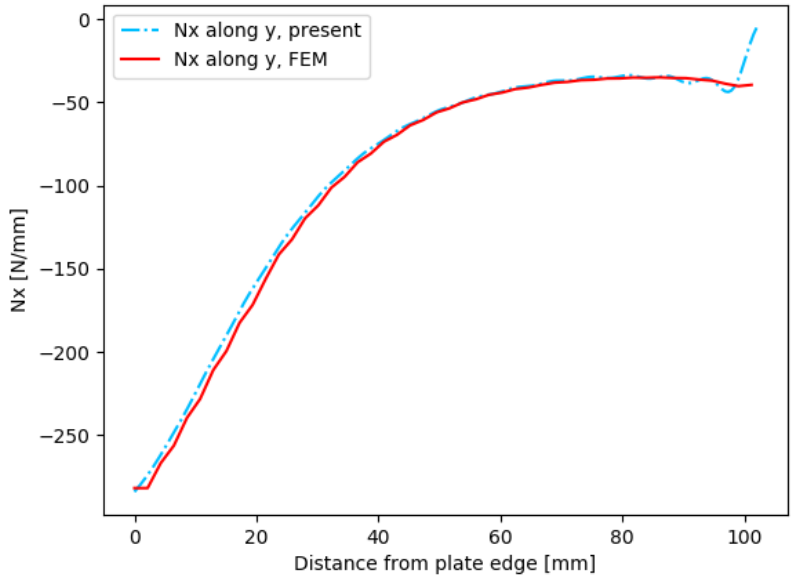

Figure 7.10: N_x distribution along y, $x = a/2$ for the $[90\pm < 0|75 >]_s$ VAT laminate, under uniform compressive displacement

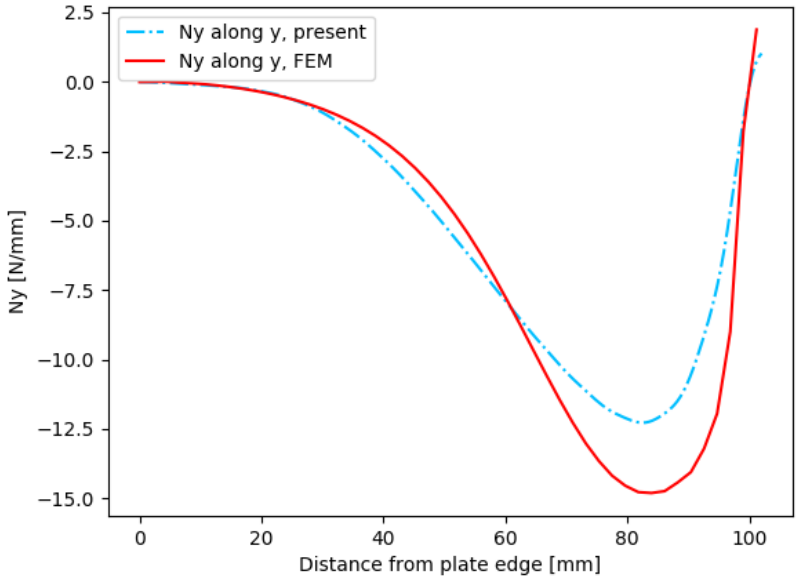

Figure 7.11: N_y distribution along y, $x = a/2$ for the $[90\pm < 0|75 >]_s$ VAT laminate, under uniform compressive displacement

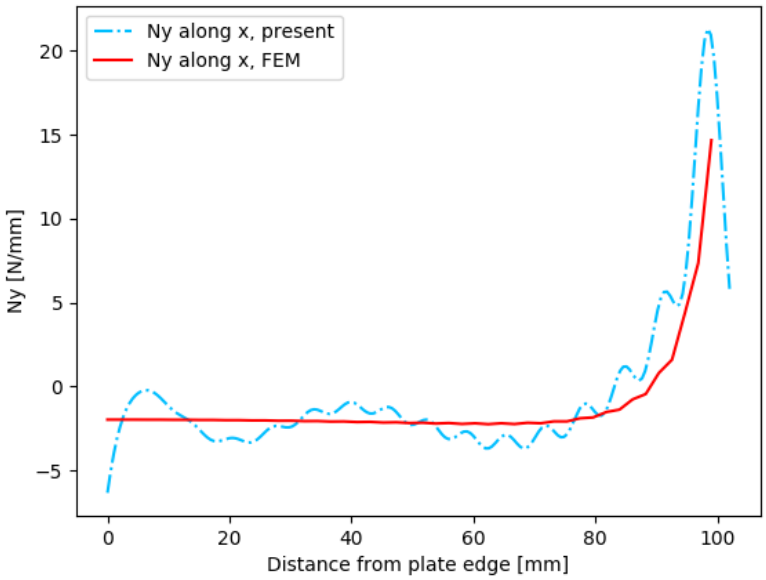

Figure 7.12: N_y distribution along x, $y = b/2$ for the $[90\pm < 0|75 >]_s$ VAT laminate, under uniform compressive displacement

From Figs. 7.8 to 7.12, the results can be seen to be in good agreement. Only the N_y distribution shows some discrepancy in both Fig. 7.11 and 7.12. It is not directly clear why

this is the case. From Fig. 7.12, the oscillations might hint towards a lack of convergence, but the analysis was also done using more terms yielding the same results. Furthermore, the results in Fig. 7.11 also show discrepancies, while they show a similar trend. Again, it is not directly clear why this is the case. The analysis including more terms provided the same result for the semi-analytical model. It is clear however, that for both the semi-analytical and FE model, the N_y results provided deviations and seems to have trouble capturing the load distribution, while this is not the case for the N_x and N_{xy} distributions. For the FE model, this is likely due to the mesh size and distribution near the cut-out edge. For the semi-analytical model, it is likely due to the choice of trial functions, the use of a stress-based approach with the Airy-stress function and the increasing complexity of the material properties when analysing VAT laminates.

7.3 Buckling Results

In this section, the buckling results are presented. The out-of-plane procedure from Chapters 4 and 6 are used, combined with the in-plane load distributions calculated in the previous section. The eigenvalues are again determined in terms of compressive displacement in [mm] and are presented in Table 7.1 for the first 5 eigenmodes of the laminate. For verification of these results, the ABAQUS model could not be used due to the residual thickness in the cut-out section elements. The eigenmodes calculated by ABAQUS were all related to the element inside the cut-out, which are of very low stiffness, and not relevant for comparison in this section. Instead, the buckling values are compared to those for a VAT laminate of the same layup, but without cut-out. The results for the VAT laminate without cut-out have been verified with ABAQUS and should provide a good comparison for the buckling values of the VAT laminate with a cut-out. Furthermore, they can provide a good insight into the decrease in buckling load compared to a pristine laminate, and thus the advantage of VAT laminates when considering cut-outs. The eigenvalues are presented in Table 7.1. The buckling modes are obtained using the trial functions from Chapter 4 with $I = J = 15$ and $M = N = 10$.

Table 7.1: Eigenvalues for the VAT laminate both with and without cutout.

Mode no.	Eigenvalues	
	Pristine	Cut-Out
1	0.01262	0.01196
2	0.01300	0.01370
3	0.01790	0.01824
4	0.02441	0.02472
5	0.02668	0.02596

From Table 7.1, it can be seen that some buckling eigenvalues are greater than those of the pristine VAT laminate. This is noteworthy, as removing material does not seem an efficient way to increase the buckling load. A possible explanation for this is the load distribution for N_x. Due to the fibre orientation, the load is shifted more towards the outer edges of the laminate. However, when introducing the cut-out, the load is re-distributed to these outer edges even more. From the literature cases, it was observed that this increased load

distribution towards the outer edges increases the buckling load. The N_x distribution for the VAT laminate with and without cut-out is shown in Fig. 7.13.

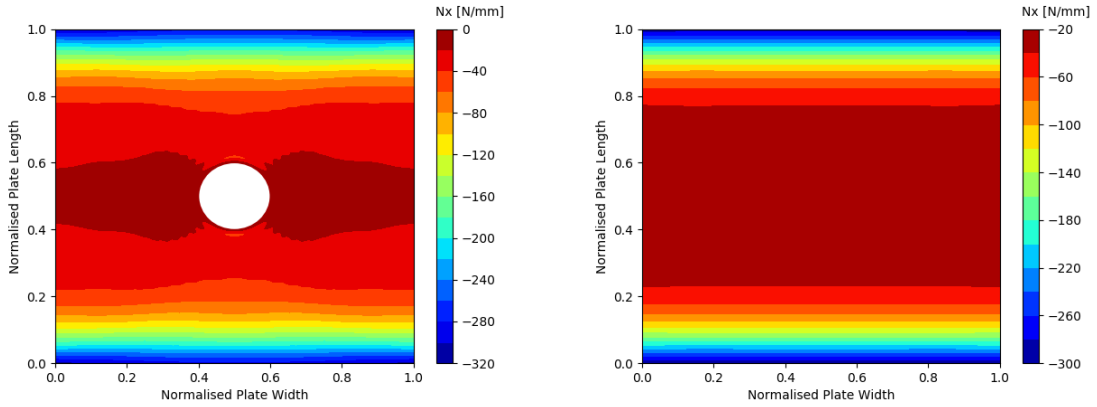

Figure 7.13: Comparison of the N_x distribution for the VAT laminate with and without cut-out.

The eigenmodes for the VAT laminate both with and without cut-out are shown side-by-side in Figs. 7.14 through 7.18. It can be seen that the rough shape of the eigenmodes remains the same, with slight changes due to the cut-out.

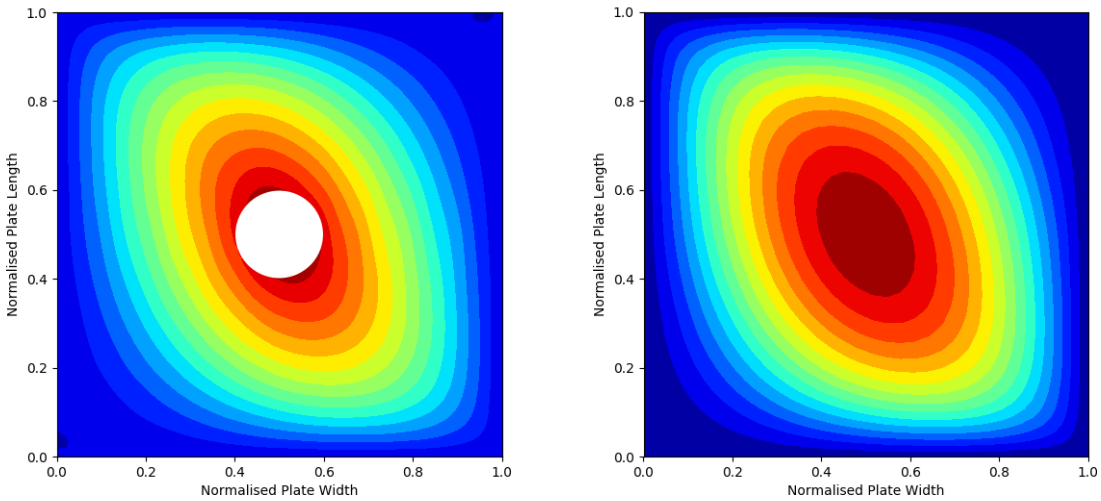

Figure 7.14: Comparison of buckling mode no. 1, with and without cut-out obtained with semi-analytical model.

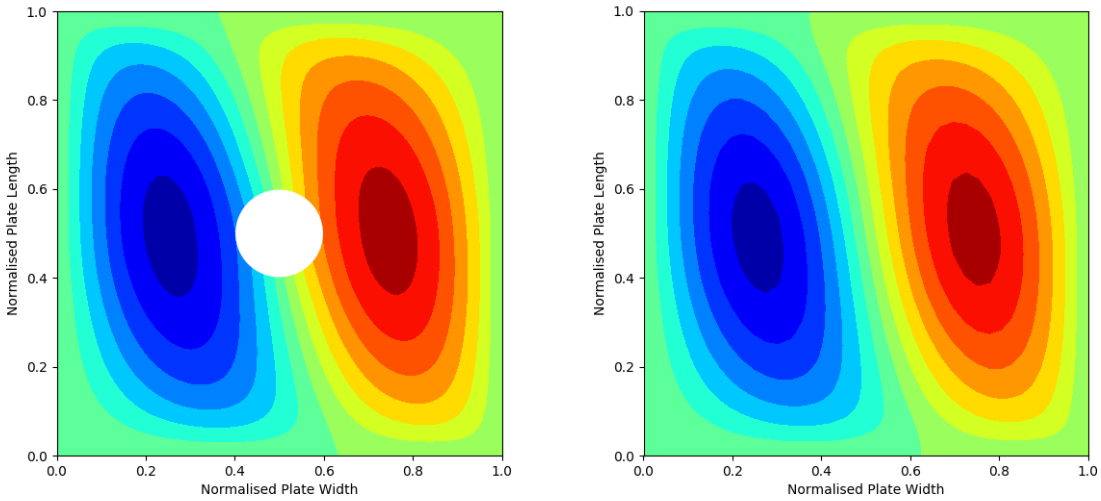

Figure 7.15: Comparison of buckling mode no. 2, with and without cut-out obtained with semi-analytical model.

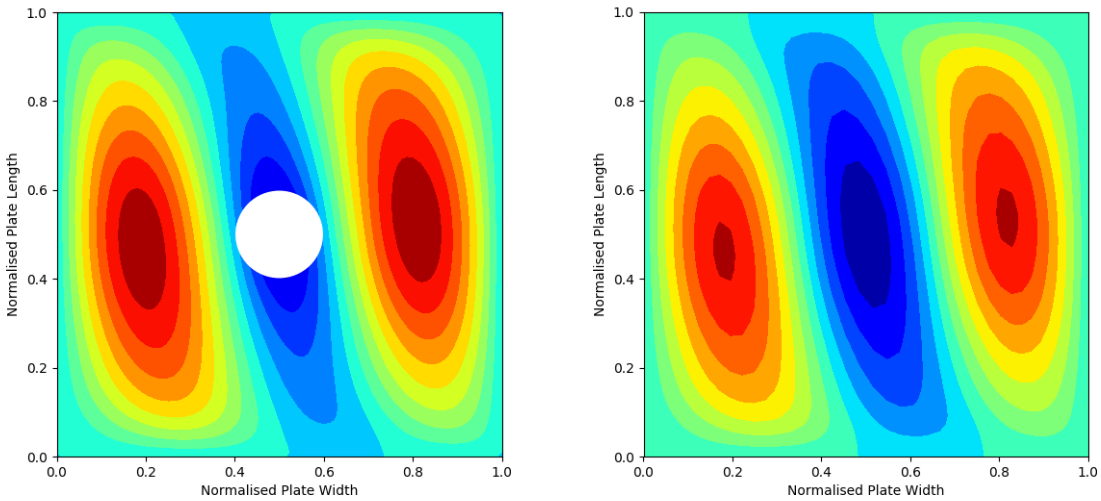

Figure 7.16: Comparison of buckling mode no. 3, with and without cut-out obtained with semi-analytical model.

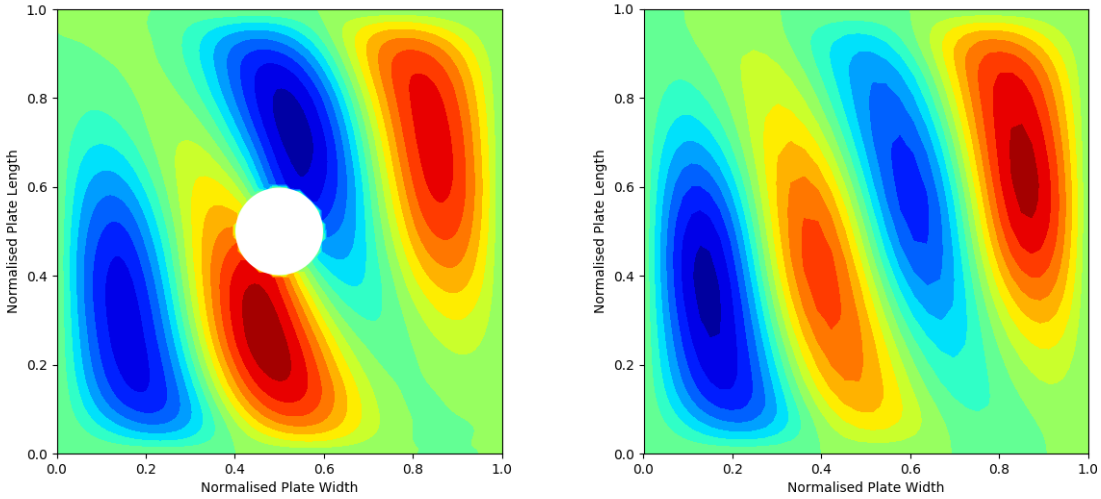

Figure 7.17: Comparison of buckling mode no. 4, with and without cut-out obtained with semi-analytical model.

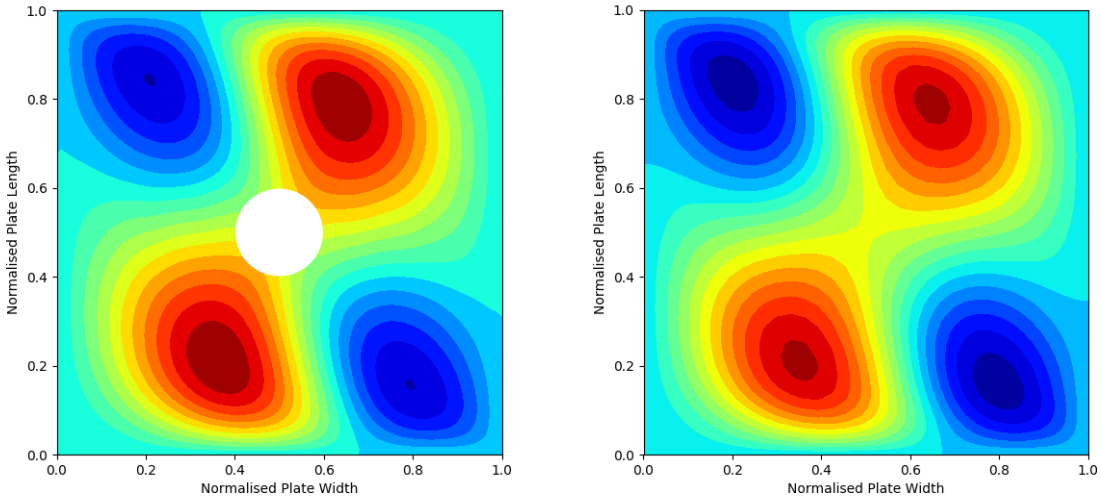

Figure 7.18: Comparison of buckling mode no. 5, with and without cut-out obtained with semi-analytical model.

Chapter 8

Discussion & Recommendations

In this chapter, some notes that can be placed with the work done in this thesis are discussed. This includes the choice for the numerical integration scheme, the trial functions chosen for the in-plane loads, and finally the thickness effects and manufacturing constraints that are present when manufacturing VAT laminates. For each of these discussion points, recommendations will be made for future development.

8.1 Numerical Integration Scheme

The numerical integration scheme presented in this thesis is the Gauss-Legendre Quadrature. This method has proven to be very accurate and has the potential to cover very high order polynomials due to the possibility to increase the amount of integration points. While this method thus lends itself well to this thesis, according to literature it is best used for polynomial functions, whereas in this thesis mainly trigonometric functions are used. Furthermore, the trial functions to integrate are defined in the r and θ coordinate system where the perimeter domain integration was defined in the x and y domain. This increased complexity has not proven to be a problem, as r and θ are also a function of x and y, however the relations do require a higher number of integration points in all dimensions for the results to converge to the correct answer. It is however not researched whether other numerical integration methods would be better suited. The convenience of the Gauss-Legendre Quadrature integration method was the deciding factor for its use.
An additional note to the numerical integration method is the computational cost. With the increasing number of integration points the computational steps increase simultaneously. For each integration point, the local material properties must be determined, which can increase the computational time rapidly. While it is considered the technique used in this thesis can be improved, no additional attention was given to this, as more priority was given to the development of the numerical integration model and trial functions.
As a recommendation, other numerical integration techniques should be considered to determine if the Gauss-Legendre Quadrature is indeed as adequate as it is convenient. With increasing

number of integration points, the density of the points varies widely across the laminate, while this may not be necessary at each point of the laminate. In other words, the higher-order functions to determine the behaviour close to the cut-out edge do not influence the laminate close the outer edge, but do influence the number of integrations points at those regions. Subdomain integration could provide more efficient methods, but is not considered in this thesis.

8.2 Trial Functions

For the analysis concerning the out-of-plane displacement, w, the trial functions are displacement-based where the trial functions for the in-plane analysis are stress-based using the Airy stress function. The stress-based approach was taken in order to reduce the number of unknown functions in the energy functionals, but yielded the need for additional boundary conditions on the edges of the cut-out. The boundary conditions along the free edge of the cut-out, as defined in Appendix D, were not incorporated into the trial functions in this thesis. The main reason for this is the dependency of the different sets of trial functions on x, y, r and θ, while the boundary conditions are defined in either x and y along the outer edges or r and θ along the edge of the cut-out. Effort was made to incorporate the learnings of the method by Lekhnitskiy [21], however the use of complex coordinates made the transfer to the present trial functions difficult before it was finally abandoned in order to not delay the thesis further. A logical follow-up study would be to perform the in-plane analysis using displacement-based trial functions. Rather than using the Airy stress function, trial functions for the in-plane displacements u and v could be taken. This increases the number of unknowns, but could lead to less terms required for each unknown set as the trial functions can describe the behaviour "directly" rather than describing the behaviour using a twice differentiated function, i.e. the Airy stress function. Furthermore, when using trial functions for the displacements rather than stresses, the issues encountered at the free edges for the cut-out will be disappear. This approach was used in the work by Alhajahmad for VAT laminates without cut-outs [19]. While the work by Alhajahmad did not account for cut-outs, the non-linear strain equations are used to determine the in-plane and out-of-plane behaviour simultaneously rather than decoupling them by using the linear strain equations. In that case, a single non-linear equation is obtained and complicated algorithms are used in order to find a solution for pristine VAT laminates [19].

8.3 Thickness Effects

When manufacturing VAT laminates according to the fibre orientation definitions in Eq. 2.1 and Eq. 2.2, the tows of fibres will overlap or leave gaps depending on the alignment and angle distribution. This is illustrated nicely by Peeters et al. in Fig. 8.1 [10].

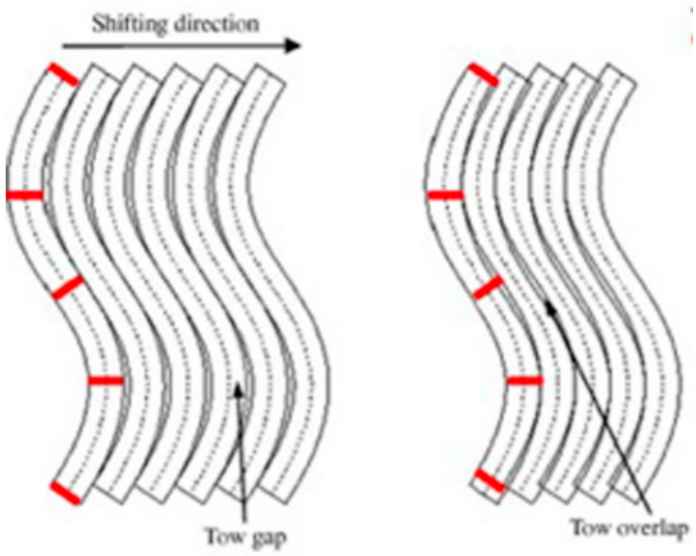

Figure 8.1: Ply overlaps or gaps depending on the tow shift. Image from [10].

Thusfar in this thesis this thickness variation is neglected, as is it in most reference literature. However in some it has been presented, such as in the study by Tatting & Gürdal when manufacturing and testing VAT laminates [11]. The manufactured laminate by Tatting & Gürdal shows the thickness variation due to overlaps in Fig. 8.2.

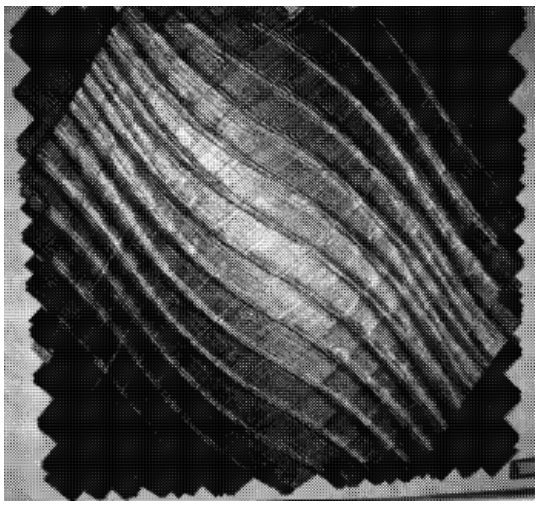

Figure 8.2: The laminate manufactured by Tatting & Gürdal showing thickness variation due to ply overlaps. Image from [11].

While this variation in thickness has a discrete character over the domain, where there either is or isn't an overlap, Castro et al. [12] proposed a smeared thickness approach, where a relation between the width and angle of the tows is shown and an approximate continuous relation between the laminate thickness and tow orientation is derived, reviewed here briefly. At the edge of the plate, $x = 0$, the tows are assumed to be aligned side-by-side with no overlaps. Then at the center of the plate, $x = a/2$, due to the fibre orientation angle, φ,

the effective tow width, w_e, has increased w.r.t. w_{tow} and there are overlaps in the tows as a consequence, this is visualised in Fig. 8.3a. From Fig. 8.3b, a relation can be deduced between the effective tow width, w_e, and the tow width, w_{tow}, this relation has been proposed by Blom et al. [27] and is shown in Eq. 8.1.

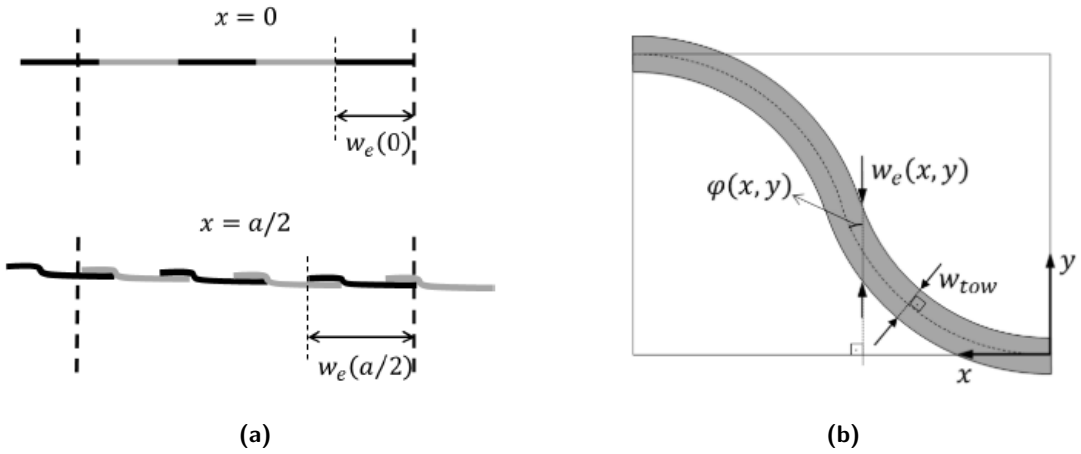

(a) **(b)**

Figure 8.3: Figures showing (a) the overlaps of the tows and (b) the tow orientation. Images from [12].

$$w_e \approx \frac{w_{tow}}{sin\varphi(x,y)} \tag{8.1}$$

At $x = 0$, there are n_{tow} tows, each with width w_{tow}, thus to total width, b, is equal to $b = n_{tow} \cdot w_{tow}$. The cross-sectional area, A, is equal to $A = n_{tow} \cdot h_{tow} \cdot w_e$. Then defining a smeared thickness, h_e, the cross-sectional area can be defined as $A_e = h_e \cdot b$. Setting $A = A_e$ results in the same material volume across the cross-section for both the smeared thickness as discrete thickness variational laminate. Using Eq. 8.1, an function can be derived for the smeared thickness, h_e, shown in Eq. 8.2.

$$\begin{aligned} A &= A_e \\ n_{tow} \cdot h_{tow} \cdot w_e &= h_e \cdot n_{tow} \cdot w_{tow} \\ h_{tow} \cdot w_e &= h_e \cdot w_{tow} \\ h_e &\approx \frac{h_{tow}}{sin\varphi} \end{aligned} \tag{8.2}$$

In order to derive this expression, the assumption has been made that the tows start in a side-by-side fashion at the edge of the laminate, with no overlaps.

In this thesis, these thickness effects are neglected for several reasons. For isotropic plates with cut-outs, for which most verification cases are defined, this effect is not present, thus the model was not set up for this initially. When considering the VAT laminate with $T_0 = 45°$ and $T_1 = 0°$, according to Eq. 8.2 the thickness in the laminate center is 1.41 times thicker. However, as the VAT applications in Chapters 4, 5 and 6 served as verification cases from literature, the thickness effects were not incorporated in the semi-analytical or ABAQUS model. Furthermore, by designing a panel such that there are equal number of gaps as overlaps

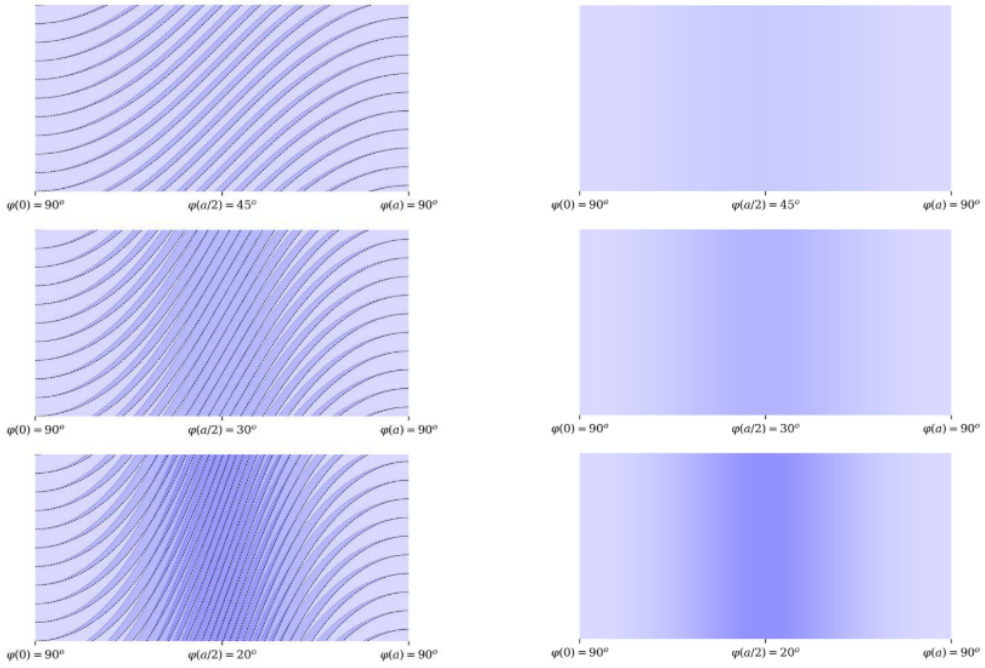

Figure 8.4: The concept of smeared thickness visualised with (a) fibre path including overlaps and (b) thickness distribution visualised with colour gradient. Images from [12].

and allowing ply drops inside the laminate domain, the thickness effects of a laminate can be reduced. This is illustrated by Peeters et al. for a VAT design without cut-outs, where the thickness is relatively constant with the exception of some waviness due to the various tow starts / stops in the laminate [10].
In future work, efforts can be made to incorporate these thickness effects into the model. This would affect the local material properties of the laminate. While this is possible to the current model with little modifications, certain effects must be considered. Varying the thickness according to the fibre path increases the function-order of the material properties, yielding a higher number of integration points required. As mentioned before, determining the local material properties can be computationally expensive.

8.4 Manufacturing Considerations

Finally, in this thesis no manufacturing constraints are posed. When considering VAT laminates the curvature of the tows must be within certain limits. According to Peeters et al., this is due to two reasons. First, because the fibre placement machine must be able to apply the tows without encountering tow wrinkling due to excessive curvature. Second, the curvatures of the tows should not be too small or to large to avoid excessive overlaps or gaps [10]. These manufacturing constraints are usually posted as a minimum radius of the tows. As the minimum radius is dependent on the process conditions during manufacturing

and this thesis was more focussed on the development of the semi-analytical model, it is not taken into consideration.

8.5 Expanding to Non-Linear Fibre Paths

So far, in this thesis, only linearly varying fibre paths are used. More variation in fibre paths can be used when including fibre paths defined by the non-linear equation from Eq. 2.2. With this fibre path definition paths can be created such as the one created by Yau and Chou in Fig. 2.8 where the fibres "flow" around the cut-out. More designs can be created and analysed using the model from this thesis to expand the results. However, creating fibre paths with these definitions, the fibre path definition polynomial order is dependant on the number of reference points taken. While this increases the amount of design possibilities, it also increases the number of integration points required for the analysis. As mentioned before, this can have a significant effect on the analysis time required.

8.6 Expanding the Cut-Out Shapes and Locations

So far, the only cases analysed in this thesis are those regarding an empty circular hole, or cut-out, located in the center of the plate or laminate. The model is capable however, to expand the results with respect to these design properties.
The definition of the location of the integration points for the cut-out are with respect to a zero position in the derivation in Section 3.3.2. This zero position can be altered to locate the cut-out at any location on the laminate. Note, that the choice of trial functions in this thesis has been verified for central located holes and not for holes at other laminate locations. While the author has confidence the trial functions should be adequate, it is not verified.
In a similar recommendation, the shape of the hole as defined in Section 3.3.2 is limited to circular in this thesis. While verification work has been performed using a square stiffening insert in Chapter 5, it was not used in the cut-out analysis. A logical follow-up study would be to expand the results to cut-out shapes other than circular. The definitions from Section 3.3.2 could be rewritten to provide an elliptically shaped cut-out. Another option would be to combine the circular, elliptical and rectangular shapes to form new shapes, such as a window for example.

8.7 Expanding to Filled Hole Compression / Joint Analysis

A different approach using the method from this thesis is not to examine a presence of a cut-out, but to examine the presence of a stiffening element. This is touched upon in the research by Kassapoglou in Chapter 5, but besides verification it is not further used in this thesis. It is an interesting case however, where a stiffening circular section could represent a bolt or rivet in a jointed piece of material. This allows for the analysis of filled hole compression or tension

analyses' and could be used in the analyses' of laminate joining when riveting. In these cases the fibre paths would need to be designed not to alleviate the stiffness/stresses around the section, as this will reduce the strength, but adding more stiffness around the section would likely be beneficial. This topic is not covered in this thesis as it was not the main topic, but it is recognised to be an interesting case to investigate using the present model.

Chapter 9

Conclusion

Looking back at the research question posed in the introduction.

Can an efficient model be developed to predict the mechanical behaviour of (VAT) laminates containing discontinuities such as cut-outs?

In order to find an answer, first, a literature study was performed where the design and analysis aspects of VAT laminates are considered and literature where cut-outs are the main research topic was reviewed. Using the linear strain equations, the in-plane and out-of-plane behaviour of the laminates were decoupled, allowing the two behaviours to be solved separately.

Using the knowledge from literature, a semi-analytical model was developed to describe the out-of-plane deflection behaviour based on energy methods with approximation functions. This model was verified using known solutions for isotropic plates without cut-outs before introducing a cut-out and adding the enriching functions to the approximations. After successfully verifying these results, the semi-analytical method including enriching functions was applied to describe in-plane pre-buckling behaviours.

To determine the pre-buckling behaviour, a slightly different approach was taken. The Total Complementary Energy was combined with the Airy stress function in order to reduce the number of unknowns in the system. This implies a stress-based approach rather than displacement-based. A consequence for the trial functions is that they must comply with the natural boundary conditions for free edges along the cut-out. This problem was not encountered with the Total Potential Energy as the displacement-based method only considers the geometric boundary conditions. To overcome the problem, the residual thickness was introduced for the cut-out. This yielded good results for the in-plane stress-state, however a consequence of the method was shown to be stress fluctuations near the free edge of the cut-out due to the presence of the residual thickness.

In order to obtain the buckling behaviour, the out-of-plane and in-plane models are coupled using the non-linear strain equations. The approximations for the out-of-plane and in-plane

behaviours were used to determine the buckling results within 2% for solid VAT laminates and 2% for isotropic plates with cut-outs, compared to ABAQUS FE results.

Finally, the model is applied to a design case of a VAT laminate with a linear fibre orientation. Again, the model showed good agreement for the in-plane load distributions apart from some discrepancies. The in-plane stress state was used to determine the buckling for a VAT laminate with cut-out and while it could not be verified directly, the results compared to that of a similar VAT laminate without cut-out provided confidence in the results.

The answer to the research question thus is yes, it is possible. The results showed good agreement with those obtained from FEM while using far less degrees of freedom. The number of degrees of freedom are even lower when comparing to reference literature which used different trial functions. With increased complexity, e.g. more intricate VAT designs, the model does require increased number of integration points which influences the computational cost considerably, however it is believed this efficiency can be improved by those with more advanced programming skills than those of the author.

A result of the decision to use stress-based approximations for the pre-buckling analysis is the presence of oscillations in the stresses surrounding the cut-out. This is due to the stress-based boundary conditions at the cut-out edge and the use of the residual thickness for the analysis. This could likely be avoided by using displacement based approximations and is recommended for further research.

Even though the pre-buckling stress-state shows oscillations due to the trigonometric approximation functions, the results give a good impression of the stress field and stress concentrations. Furthermore, the semi-analytical model in this thesis has proven to be accurate for the determination of deflection and buckling of (VAT) laminates.

Appendix A

Convergence Behaviour

In this appendix, the convergence of the trial functions introduced in this thesis is presented. First, the out-of-plane results are shown before showing the in-plane convergence results. Finally, a table of the buckling eigenvalues is shown with increasing number of terms.

A.1 Out of Plane

In Fig. A.1, the deflection results for the isotropic plate with a cut-out are shown with all intermediate steps. In total, 10 radial terms are included, which can be seen to be increasingly close to the result obtained from the finite element model.

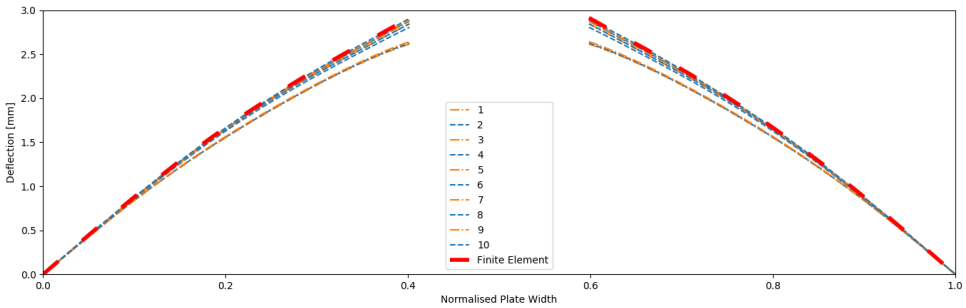

Figure A.1: Visualisation of the convergence of the model with increasing terms for M in the functions $w_2(x, y)$.

A.2 In-Plane

The plots shown in Chapter 5 for the N_x and N_y loads along paths are repeated here with intermediate results also shown.

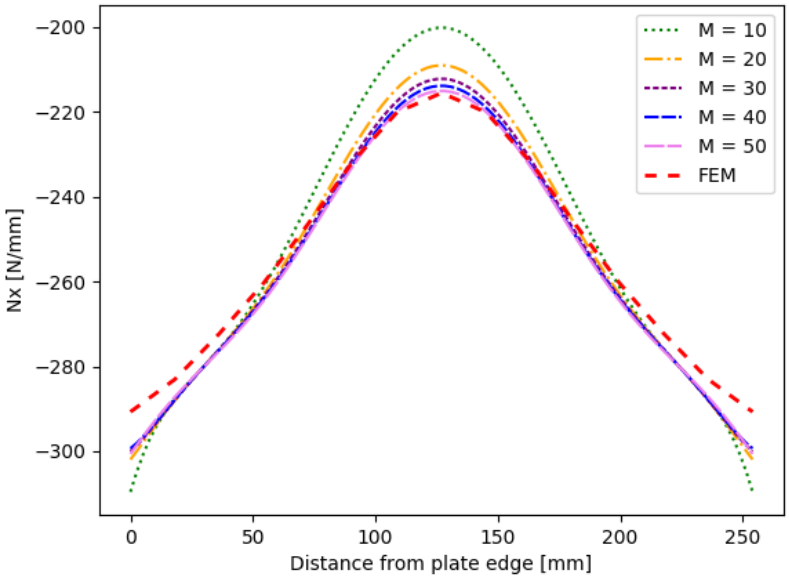

Figure A.2: N_{x0} Results for various number of radial terms, $M = 10, 20, 30, 40, 50$.

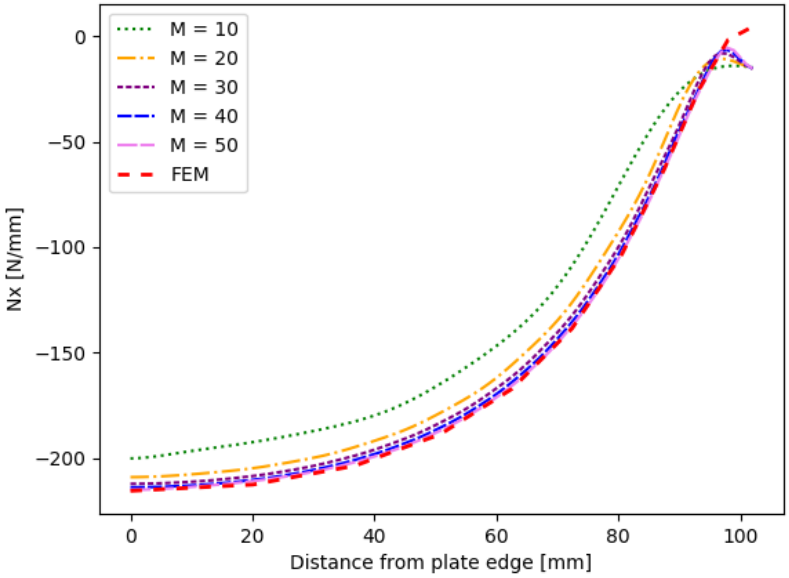

Figure A.3: N_x Along x results for various number of radial terms, $M = 10, 20, 30, 40, 50$.

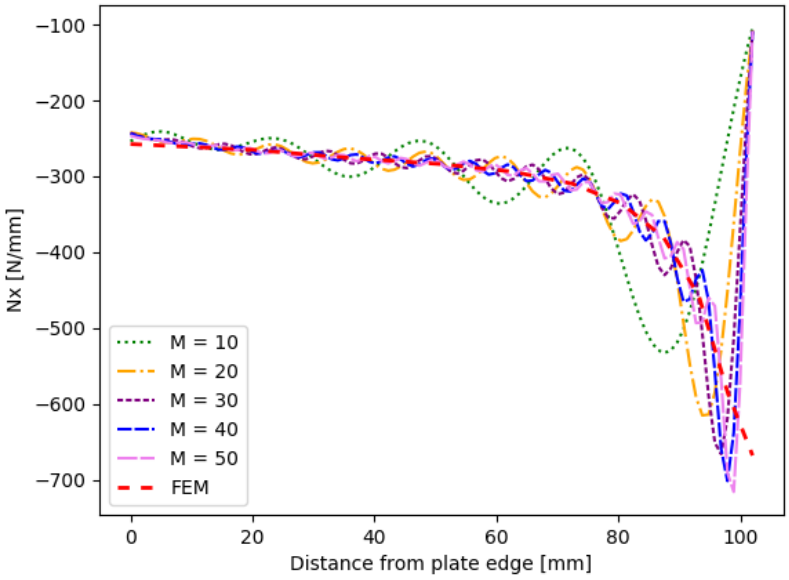

Figure A.4: N_x Along y results for various number of radial terms, $M = 10, 20, 30, 40, 50$.

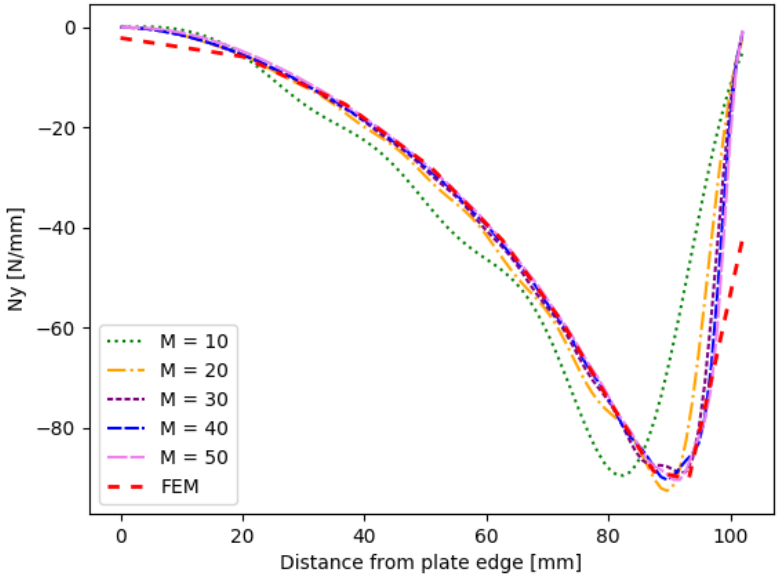

Figure A.5: N_y Along y results for various number of radial terms, $M = 10, 20, 30, 40, 50$.

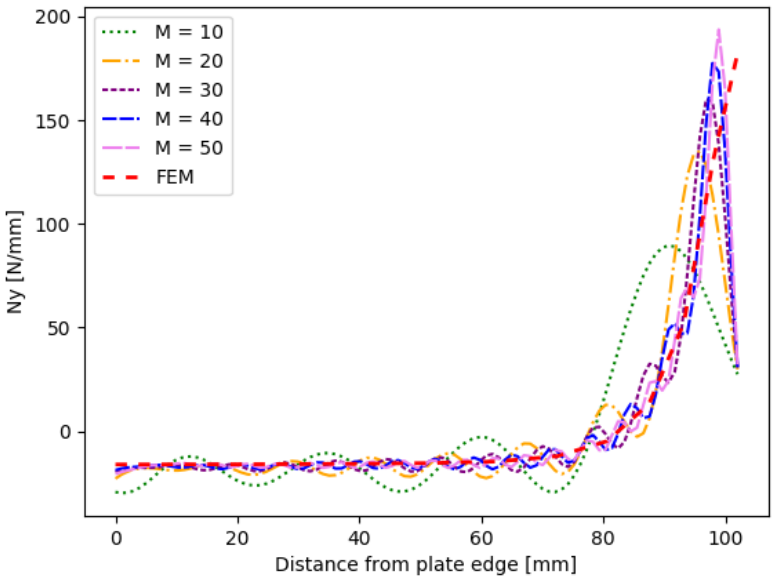

Figure A.6: N_y Along x results for various number of radial terms, $M = 10, 20, 30, 40, 50$.

From the plots , it can be seen that both the amplitude and location of the stress concentrations move more towards to the edge of the cut-out.

A.3 Buckling

In Section 5.4.3, the convergence of the in-plane load distributions is shown. Here, the buckling eigenvalues with respect to these various amount of terms is shown. The results are shown in Table A.1.

Table A.1: Eigenvalues for various in-plane load distributions, calculated with varying number of radial terms.

Mode no.	No. of radial terms, M					ABAQUS
	10	20	30	40	50	
1	0.01528	0.01478	0.01461	0.01448	0.01448	0.01427
2	0.02810	0.02721	0.02690	0.02676	0.02666	0.02630
3	0.04524	0.04389	0.04342	0.04318	0.04304	0.04302
4	0.05798	0.05752	0.05736	0.05729	0.05723	0.05742
5	0.06188	0.06174	0.06159	0.06156	0.06152	0.06098

Appendix B

Energy Matrix Entries

In Section 5.2 the problem is given in Eq. 5.12. Here the entries for the matrix are derived and shown in more detail for reference.

$$\begin{bmatrix} \mathbf{K} & \mathbf{K_C} \\ \mathbf{K_C}^T & \mathbf{C} \end{bmatrix} \begin{Bmatrix} \varphi \\ \mathbf{c} \end{Bmatrix} = \begin{Bmatrix} \mathbf{0} \\ \mathbf{Px0} \end{Bmatrix}$$

B.1 Strain Energy Formulation

The strain energy formulation is given in Eq. B.1, where a_{16} and a_{26} have already been left out with respect to Eq. 5.1 due to the symmetric and balanced layup assumption.

$$U = \frac{1}{2} \iint_{\Omega} \left(a_{11} N_x^2 + a_{22} N_y^2 + 2 a_{12} N_x N_y + a_{66} N_{xy}^2 \right) d\Omega \tag{B.1}$$

Using the Airy stress formulation, and the trial functions for the Airy stress functions, this expression can be expanded.

$$N_x = \frac{\partial^2 \Phi}{\partial y^2} \qquad N_y = \frac{\partial^2 \Phi}{\partial x^2} \qquad N_{xy} = -\frac{\partial^2 \Phi}{\partial x \partial y}$$

$$\Phi = \Phi_0(y) + \Phi_1(x,y) + \Phi_2(x,y) + \Phi_3(x,y)$$

The dependency on (x, y) is from hereon omitted for legibility.

$$\begin{aligned} U = \frac{1}{2} \iint_{\Omega} \Big\{ & a_{11} \left(\Phi_{0,yy} + \Phi_{1,yy} + \Phi_{2,yy} + \Phi_{3,yy} \right)^2 \\ & + a_{22} \left(\Phi_{0,xx} + \Phi_{1,xx} + \Phi_{2,xx} + \Phi_{3,xx} \right)^2 \\ & + a_{12} \left(\Phi_{0,yy} + \Phi_{1,yy} + \Phi_{2,yy} + \Phi_{3,yy} \right) \left(\Phi_{0,xx} + \Phi_{1,xx} + \Phi_{2,xx} + \Phi_{3,xx} \right) \\ & + a_{66} \left(-\Phi_{0,xy} - \Phi_{1,xy} - \Phi_{2,xy} - \Phi_{3,xy} \right)^2 \Big\} \, d\Omega \end{aligned}$$

As Φ_0 is the edge load function, it only has a value for N_x, so $\Phi_{0,xx} = \Phi_{0,xy} = 0$. Expanding the equation further yields:

$$U = \frac{1}{2}\iint_\Omega \Big\{ a_{11}\left(\Phi_{0,yy}^2 + \Phi_{1,yy}^2 + \Phi_{2,yy}^2 + \Phi_{3,yy}^2 + 2\Phi_{0,yy}\Phi_{1,yy}\right.$$
$$+2\Phi_{0,yy}\Phi_{2,yy} + 2\Phi_{0,yy}\Phi_{3,yy} + 2\Phi_{1,yy}\Phi_{2,yy} + 2\Phi_{1,yy}\Phi_{3,yy} + 2\Phi_{2,yy}\Phi_{3,yy})$$
$$+a_{22}\left(\Phi_{1,xx}^2 + \Phi_{2,xx}^2 + \Phi_{3,xx}^2 + 2\Phi_{1,xx}\Phi_{2,xx} + 2\Phi_{1,xx}\Phi_{3,xx} + 2\Phi_{2,xx}\Phi_{3,xx}\right)$$
$$+2a_{12}\left(\Phi_{0,yy}\Phi_{1,xx} + \Phi_{0,yy}\Phi_{2,xx} + \Phi_{0,yy}\Phi_{3,xx} + \Phi_{1,yy}\Phi_{1,xx} + \Phi_{1,yy}\Phi_{2,xx} + \Phi_{1,yy}\Phi_{3,xx}\right.$$
$$+\Phi_{2,yy}\Phi_{1,xx} + \Phi_{2,yy}\Phi_{2,xx} + \Phi_{2,yy}\Phi_{3,xx} + \Phi_{3,yy}\Phi_{1,xx} + \Phi_{3,yy}\Phi_{2,xx} + \Phi_{3,yy}\Phi_{3,xx})$$
$$\left. + a_{66}\left(\Phi_{1,xy}^2 + \Phi_{2,xy}^2 + \Phi_{3,xy}^2 + 2\Phi_{1,xy}\Phi_{2,xy} + 2\Phi_{1,xy}\Phi_{3,xy} + 2\Phi_{2,xy}\Phi_{3,xy}\right)\Big\}\, d\Omega$$

Collecting terms which correspond to the coupling between the various sets of trial functions will then give the energy expressions which will lead to the corresponding matrix entry.

$$U_{00} = \frac{1}{2}\iint_\Omega \left(a_{11}\Phi_{0,yy}^2\right) d\Omega$$
$$U_{11} = \frac{1}{2}\iint_\Omega \left(a_{11}\Phi_{1,yy}^2 + a_{22}\Phi_{1,xx}^2 + a_{66}\Phi_{1,xy}^2 + 2a_{12}\Phi_{1,yy}\Phi_{1,xx}\right) d\Omega$$
$$U_{22} = \frac{1}{2}\iint_\Omega \left(a_{11}\Phi_{2,yy}^2 + a_{22}\Phi_{2,xx}^2 + a_{66}\Phi_{2,xy}^2 + 2a_{12}\Phi_{2,yy}\Phi_{2,xx}\right) d\Omega$$
$$U_{33} = \frac{1}{2}\iint_\Omega \left(a_{11}\Phi_{3,yy}^2 + a_{22}\Phi_{3,xx}^2 + a_{66}\Phi_{3,xy}^2 + 2a_{12}\Phi_{3,yy}\Phi_{3,xx}\right) d\Omega$$
$$U_{01} = \iint_\Omega \left(a_{11}\Phi_{0,yy}\Phi_{1,yy} + a_{12}\Phi_{0,yy}\Phi_{1,xx}\right) d\Omega$$
$$U_{02} = \iint_\Omega \left(a_{11}\Phi_{0,yy}\Phi_{2,yy} + a_{12}\Phi_{0,yy}\Phi_{2,xx}\right) d\Omega$$
$$U_{03} = \iint_\Omega \left(a_{11}\Phi_{0,yy}\Phi_{3,yy} + a_{12}\Phi_{0,yy}\Phi_{3,xx}\right) d\Omega$$
$$U_{12} = \iint_\Omega \left(a_{11}\Phi_{1,yy}\Phi_{2,yy} + a_{22}\Phi_{1,xx}\Phi_{2,xx} + a_{66}\Phi_{1,xy}\Phi_{2,xy} + a_{12}\left[\Phi_{1,yy}\Phi_{2,xx} + \Phi_{1,xx}\Phi_{2,yy}\right]\right) d\Omega$$
$$U_{13} = \iint_\Omega \left(a_{11}\Phi_{1,yy}\Phi_{3,yy} + a_{22}\Phi_{1,xx}\Phi_{3,xx} + a_{66}\Phi_{1,xy}\Phi_{3,xy} + a_{12}\left[\Phi_{1,yy}\Phi_{3,xx} + \Phi_{1,xx}\Phi_{3,yy}\right]\right) d\Omega$$
$$U_{23} = \iint_\Omega \left(a_{11}\Phi_{2,yy}\Phi_{3,yy} + a_{22}\Phi_{2,xx}\Phi_{3,xx} + a_{66}\Phi_{2,xy}\Phi_{3,xy} + a_{12}\left[\Phi_{2,yy}\Phi_{3,xx} + \Phi_{2,xx}\Phi_{3,yy}\right]\right) d\Omega$$

The entries for the matrices $\mathbf{K}, \mathbf{Kc}$ and $\mathbf{C}$ are obtained by minimising the energy expressions above with their respective unknown coefficient.

$$[\mathbf{K}]\{\varphi\} = \begin{bmatrix} \frac{\partial U_{11}}{\partial A_{ij}} & \frac{\partial U_{12}}{\partial A_{ij}} & \frac{\partial U_{13}}{\partial A_{ij}} \\ \frac{\partial U_{12}}{\partial B_{mn}} & \frac{\partial U_{22}}{\partial B_{mn}} & \frac{\partial U_{23}}{\partial B_{mn}} \\ \frac{\partial U_{13}}{\partial C_{mn}} & \frac{\partial U_{23}}{\partial C_{mn}} & \frac{\partial U_{33}}{\partial C_{mn}} \end{bmatrix}$$

$$[\mathbf{Kc}]\{\mathbf{c}\} = \begin{Bmatrix} \frac{\partial U_{01}}{\partial A_{ij}} \\ \frac{\partial U_{02}}{\partial B_{mn}} \\ \frac{\partial U_{03}}{\partial C_{mn}} \end{Bmatrix}$$

$$[\mathbf{C}]\{\mathbf{c}\} = \begin{bmatrix} \frac{\partial U_{00}}{\partial c_k} \end{bmatrix}$$

The computations of these entries has been covered in Chapter 3.

B.2 Potential Energy Formulation

The potential energy is stated in Eq. 5.4 and repeated here in Eq. B.2. It is given as the edge displacement u times the edge load N_x at both vertical edges, integrated along this vertical edge.

$$V = -\int_0^b [\Phi_{,yy} u]_{x=0}^{x=a} \, dy \tag{B.2}$$

For N_x the expression for the Airy trail functions can be input.

$$V = -\int_0^b [u\,(\Phi_{0,yy} + \Phi_{1,yy} + \Phi_{2,yy} + \Phi_{3,yy})]_{x=0}^{x=a} \, dy$$

According to the boundary condition forcing function, the trial functions $\Phi_{1,yy}, \Phi_{2,yy}$ and $\Phi_{3,yy}$ have a zero value at the vertical edges and can thus be dropped. Furthermore, the displacement u at both edges is considered. Considering one end of the plate fixed its displacement will be zero and the compressive displacement at the other end will be indicated with Δ_x. The formulation then becomes:

$$V = -\int_0^b \Delta_x \Phi_{0,yy} \, dy$$

Where Δ_x is twice the value of the edge displacement u, also indicated in Fig. 5.1. Under uniform compressive displacement loading, this Δ_x is a constant and can be taken out of the integral.

$$V = -\Delta_x \int_0^b \Phi_{0,yy} \, dy$$

$$V = -\Delta_x \int_0^b \sum_{k=0}^{K} c_k \cdot L_k(y) \, dy$$

In Eq. 5.7 it is given that the trial functions for $\Phi_{0,yy}$ are Legendre polynomials transformed onto the $[0; b]$ domain rather than $[-1; 1]$, in which the Legendre polynomials are defined. A

convenient property of the Legendre polynomials is that the integral on the domain $[-1;1]$ is 2 for the first Legendre function, which is the constant function $L_0 = 1$. For all other Legendre functions, L_n when $n > 0$, the integral is equal to zero. Transformed to the $[0;b]$ domain, this yields that the integral of the first Legendre function is equal to b, the height of the vertical edge, while all other values will yield zero.
To obtain **Px0**, the potential energy V is minimised with respect to the coefficients c_k and will yield the following.

$$\mathbf{Px0} = -\Delta_x \begin{bmatrix} b & (k{=}0) \\ 0 & (k{=}1) \\ \vdots & \vdots \\ 0 & (k{=}K) \end{bmatrix}$$

Appendix C

Continuation on Literature

In this Appendix, the detailed results are presented for the in-plane analysis related to the work by Kassapoglou [5]. First the detailed results for the verification case of the square stiffened insert are presented where the semi-analytical model is used to recreate results. Then the results are shown when the insert shape is changed to circular and compared to the FE results. Furthermore, the results for the circular insert are compared when using the trial functions from this thesis versus those presented by Kassapoglou. Finally, this comparison between the sets of trial functions is also made for the case of a plate with a cut-out. In the first sections, the applied loading is the same as in the reference work, e.g. an applied uniform load $\overline{N}_x = 1$ [N/mm]. In the comparison with respect to the cut-out, the applied loading is changed to the applied displacement, Δ_x, as it was also used to obtain the results in Chapter 5.

C.1 Square Concentric Insert

More expanded results than those showed in Section 5.4.1 can be found here. The N_x distribution obtained from the semi-analytical model has also been compared to that obtained from the ABAQUS finite element software, shown in Fig. C.1. The result in this figure is that for the concentric layup with dimensions 254×254 [mm].

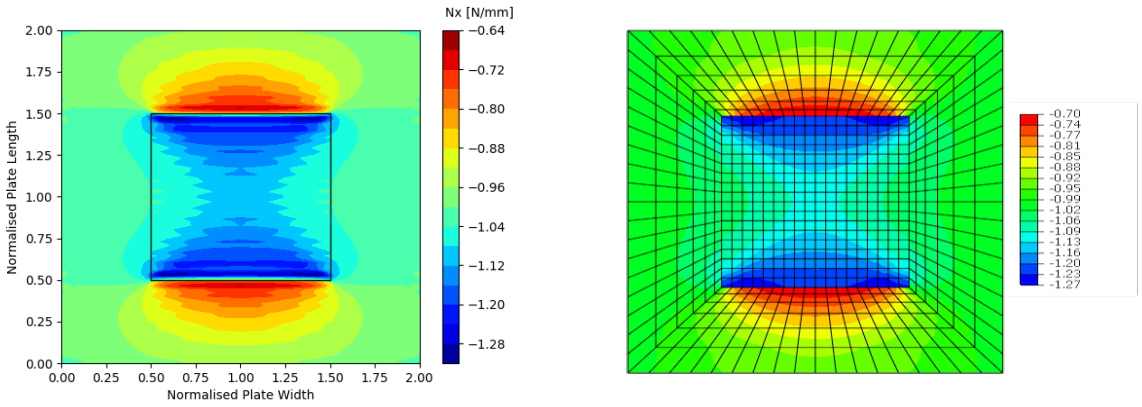

(a) Semi-Analytical **(b)** ABAQUS

Figure C.1: N_x distribution for the square concentric layups. Semi-analytic vs. ABAQUS.

C.2 Circular Concentric Insert

The next step in the approach was to reshape the central patch from a square to a circle using the method described in Section 3.3.2. In this analysis, the central patch is of the same composition as in the work by Kassapoglou, i.e. a stiff insert with respect to the perimeter layup. Again for this approach the trial functions as introduced by Kassapoglou are used, shown in Eq. 2.8, and subsequently compared to results obtained from ABAQUS.

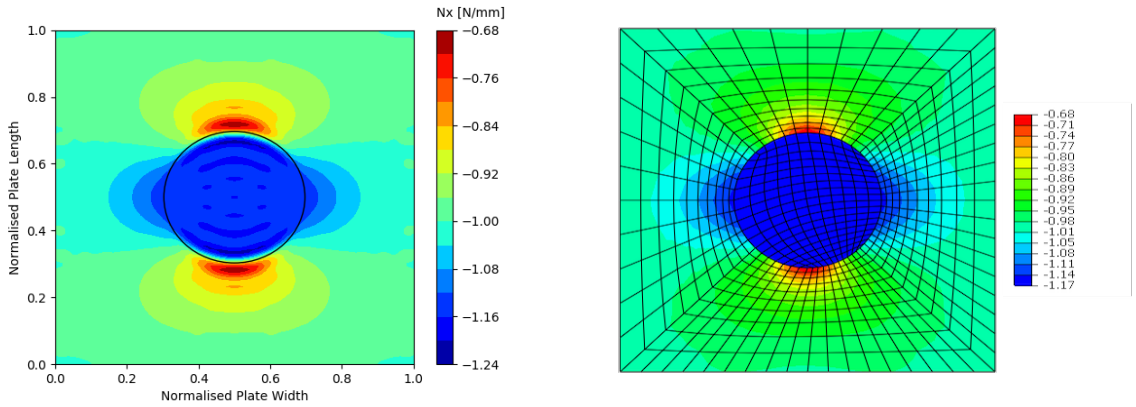

(a) Semi-Analytical **(b)** ABAQUS

Figure C.2: N_x distribution for the circular central patch. Semi-analytic using Eq. 2.8 vs. ABAQUS.

C.3 DOF Comparison: Stiffened Insert

The next step is to compare the convergence behaviour of the two sets of trial functions. For this purpose, a result is found that is similar to that in Section C.2 while using the trial

functions introduced in this thesis. The results are shown in Fig. C.3

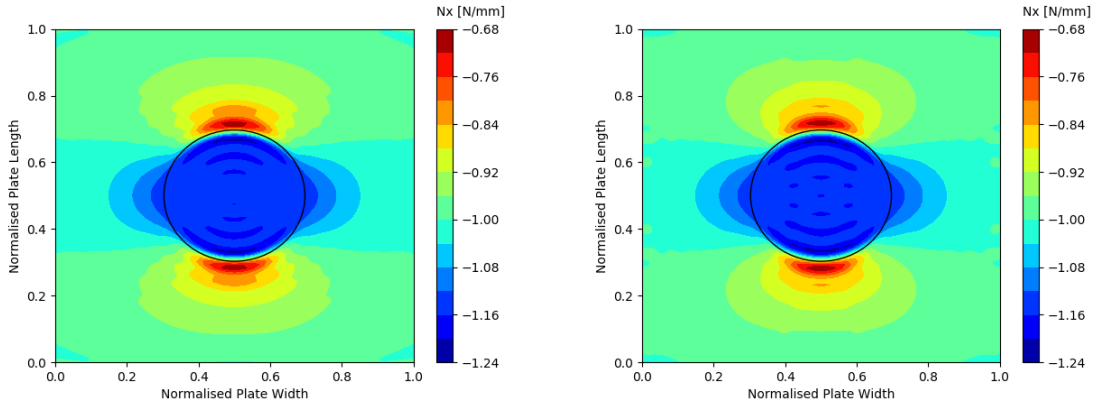

(a) Present functions: 288 terms

(b) Kassapoglou functions: 400 terms

Figure C.3: Comparison of results with respect to no. of degrees of freedom.

The results show that both sets of trial functions provide a good solution for the case of the central stiffened patch, however it seems the functions introduced in this thesis provide faster convergence. This is even more true for the case where the central patch is empty, i.e. a cut-out, which will the topic of the next section.

C.4 DOF Comparison: Cut-Out

Finally, the results obtained using the different trial functions are compared also for the plate with a cut-out. Here the loading is an applied displacement, $\Delta_x = 1$ [mm]. For the trial functions from the work by Kassapoglou, Eq. 2.8, this means they are adapted to include the Φ_0 functions for the approximation of N_{x0}. The same procedure will be taken compared to Section C.3, but now the insert will be considered a cut-out. The results are shown in Fig. C.4 through C.6. For the trial functions introduced in this thesis, the terms are taken for $I = J = K = 8$, $M = 39$ and $N = 5$ for a total of 524 terms. For the analysis using functions Eq. 2.8 the terms are taken for $K = 8$ and $M = N = 30$ for a total of 909 terms.

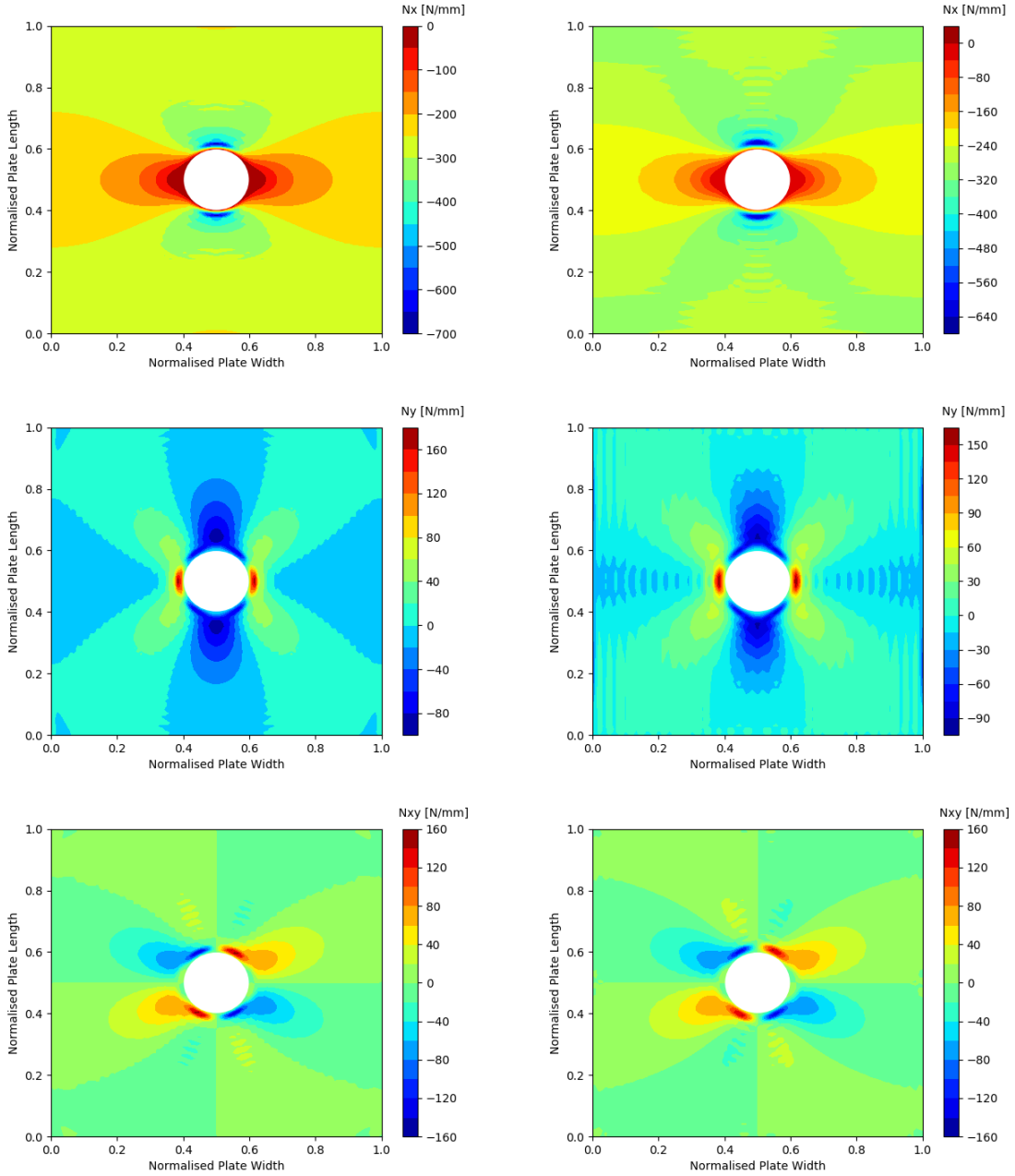

Figure C.4: Comparison of trial functions from Eq. 2.8 vs. trial functions introduced in this thesis $(1/3)$. *Left column:* Functions from this thesis, 524 terms. *Right column:* Functions from Eq. 2.8, 909 terms.

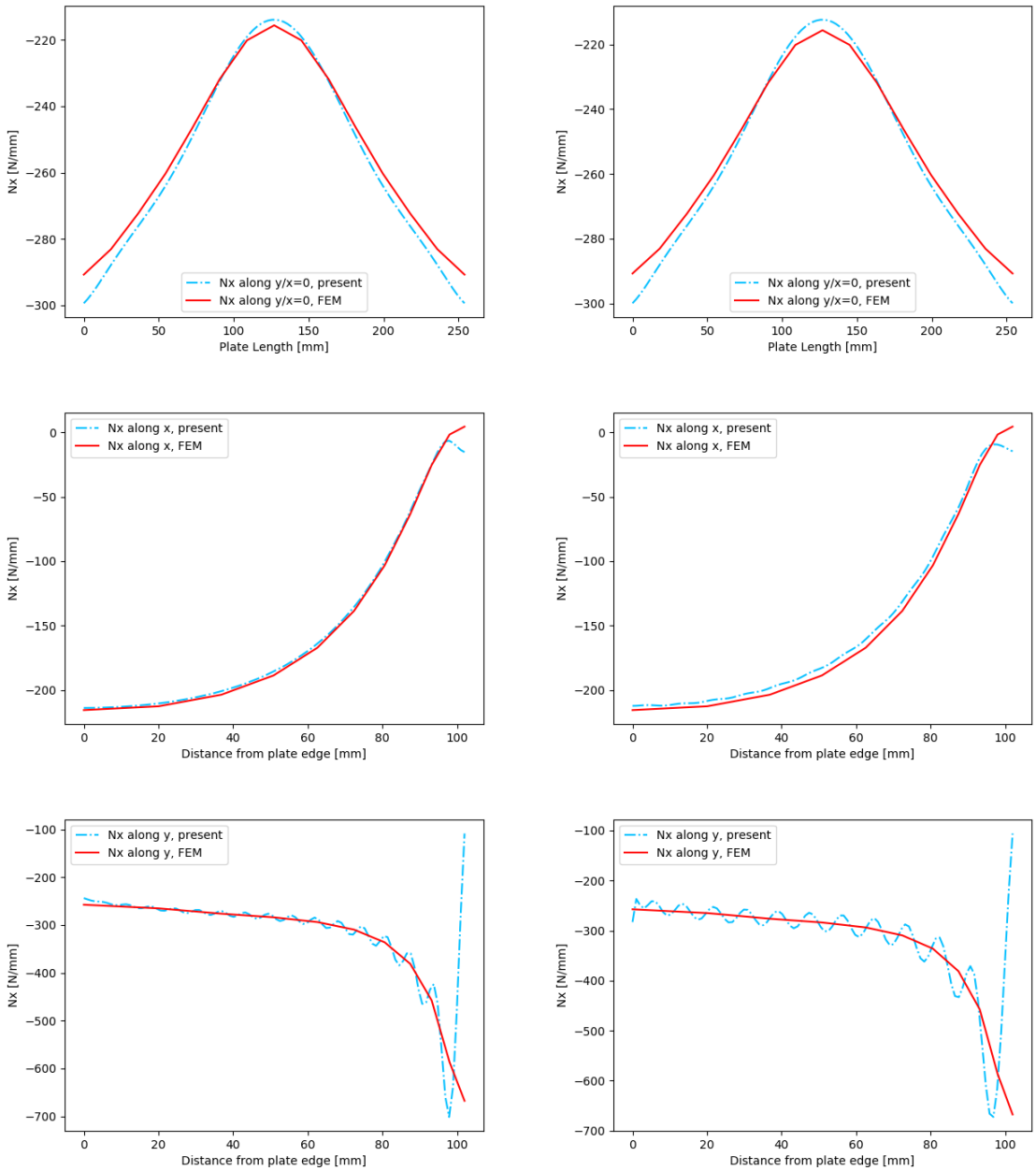

Figure C.5: Comparison of trial functions from Eq. 2.8 vs. trial functions introduced in this thesis $(2/3)$. *Left column:* Functions from this thesis, 524 terms. *Right column:* Functions from Eq. 2.8, 909 terms.

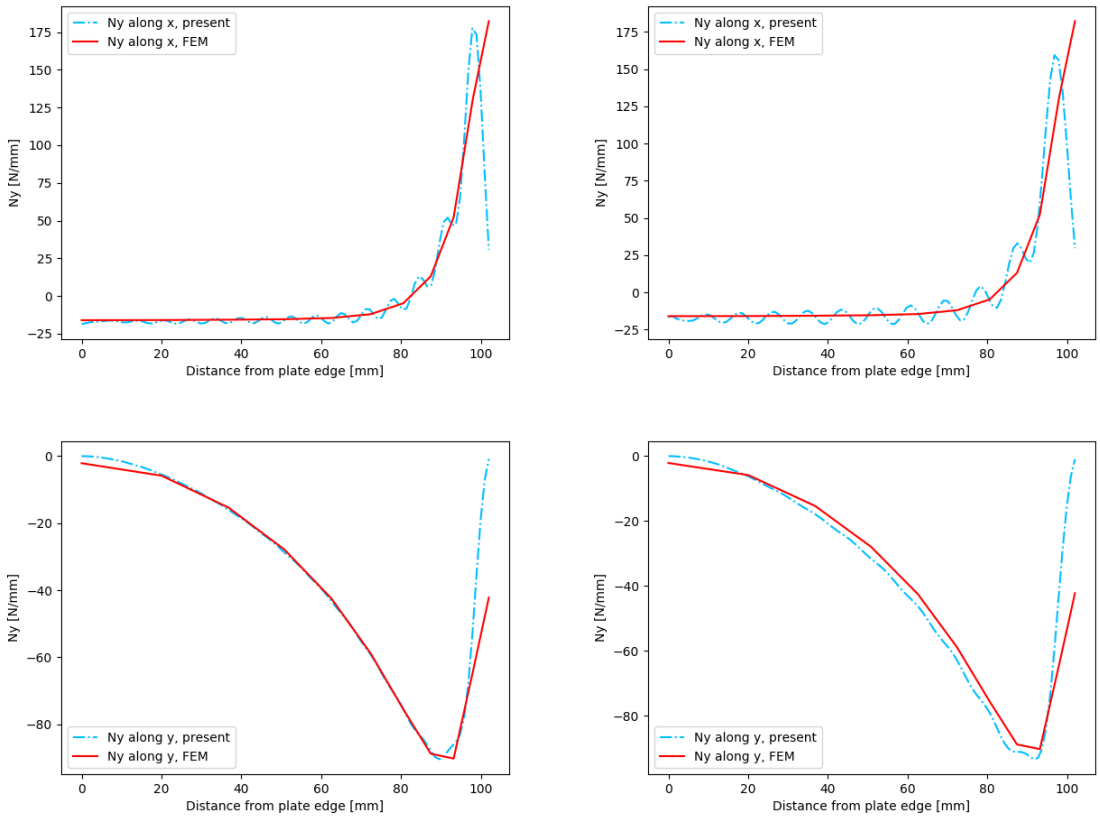

Figure C.6: Comparison of trial functions from Eq. 2.8 vs. trial functions introduced in this thesis $(3/3)$. *Left column:* Functions from this thesis, 524 terms. *Right column:* Functions from Eq. 2.8, 909 terms.

Further investigation with respect to the buckling values of these different trial functions was not done, as the effect of more waviness in the trial functions is considered reasonably covered by the convergence results in Appendix A.3.

Appendix D

Boundary Conditions at the Cut-out Edge

When introducing a cut-out, or hole, in the laminate the trial functions must also consider the boundary conditions at the free edge of the hole. In this Appendix these boundary conditions are addressed via two ways. Both rely on the Cauchy stress tensor, but are decomposed into differently oriented vectors.

D.1 Normal Loads w.r.t. Hole Edge

When zooming in on an elemental part of the plate, considering a triangle where the long side represents the free edge of the cut-out, as seen in Fig. D.1. The normal loads on the hole edge, N_r and $N_{r\theta}$ must be zero at this free edge. They are expressed in terms of N_x, N_y and N_{xy} first.

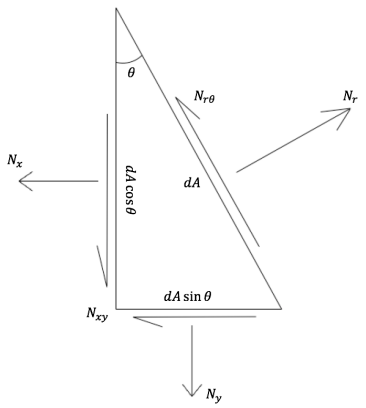

Figure D.1: Transformation of the in-plane loads to the cut-out edge normal loads.

$$N_r \cdot dA = (N_y\ dA\ cos\theta)cos\theta + (N_{xy}\ dA\ cos\theta)sin\theta + (N_x\ dA\ sin\theta)sin\theta + (N_{xy}\ dA\ sin\theta)cos\theta$$

$$N_{r\theta} \cdot dA = (N_{xy}\ dA\ cos\theta)cos\theta + (N_y\ dA\ sin\theta)cos\theta - (N_x\ dA\ cos\theta)sin\theta - (N_{xy}\ dA\ sin\theta)sin\theta$$

$$N_r = N_x\ cos^2\theta + N_y\ sin^2\theta + N_{xy}\ (2sin\theta cos\theta)$$

$$N_{r\theta} = -N_x\ cos\theta sin\theta + N_y\ cos\theta sin\theta + N_{xy}\ (cos^2\theta - sin^2\theta)$$

At the hole boundary, $r = R_{hole}$, these equations must equal zero. Furthermore, the in-plane loads can be replaced by the Airy stress function.

$$\begin{aligned} 0 &= \Phi_{,yy}\ cos^2\theta + \Phi_{,xx}\ sin^2\theta - \Phi_{,xy}\ (2sin\theta cos\theta) \\ 0 &= -\Phi_{,yy}\ cos\theta sin\theta + \Phi_{,xx}\ cos\theta sin\theta - \Phi_{,xy}\ (cos^2\theta - sin^2\theta) \end{aligned} \tag{D.1}$$

D.2 Contour Integral

In this section, again the triangle element is taken, but now rather than taking the normal loads, the loads are decomposed in X and Y as seen Fig. D.2. The expressions for X and Y can then be determined.

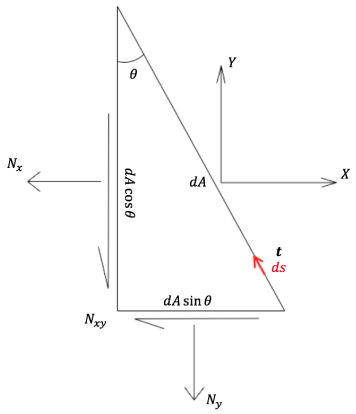

Figure D.2: Transformation of the in-plane loads to the cut-out edge loads X and Y.

$$\begin{aligned} X - N_x\ cos\theta - N_{xy}\ sin\theta = 0 \\ Y - N_y\ sin\theta - N_{xy}\ cos\theta = 0 \end{aligned} \tag{D.2}$$

When taking an infinitesimal step $\mathbf{t}$ along the edge of the cut-out in a clockwise manner with magnitude ds, the vector for $\mathbf{t}$ can be defined as:

$$\mathbf{t} = \begin{Bmatrix} \frac{dx}{ds} \\ \frac{dy}{ds} \end{Bmatrix} = \begin{Bmatrix} -sin\theta \\ cos\theta \end{Bmatrix}$$

Using the above expressions and the Airy stress function, they can be input into Eq. D.2.

$$\Phi_{,yy} \cdot \left(\frac{dy}{ds}\right) + (-\Phi_{,xy}) \left(-\frac{dx}{ds}\right) = X$$
$$\Phi_{,xx} \cdot \left(-\frac{dx}{ds}\right) + (-\Phi_{,xy}) \left(\frac{dy}{ds}\right) = Y$$

Rewriting, this becomes:

$$X = \begin{Bmatrix} \Phi_{,xy} & \Phi_{,yy} \end{Bmatrix} \cdot \begin{Bmatrix} \frac{dx}{ds} \\ \frac{dy}{ds} \end{Bmatrix} = \nabla \Phi_{,y} \cdot \mathbf{t} = \frac{d\Phi_{,y}}{ds}$$
$$Y = \begin{Bmatrix} -\Phi_{,xx} & -\Phi_{,xy} \end{Bmatrix} \cdot \begin{Bmatrix} \frac{dx}{ds} \\ \frac{dy}{ds} \end{Bmatrix} = -\nabla \Phi_{,x} \cdot \mathbf{t} = -\frac{d\Phi_{,x}}{ds}$$

Integrating these expression with respect to s along the entire cut-out boundary yields:

$$\begin{aligned} \Phi_{,y} &= \oint X ds \\ -\Phi_{,x} &= \oint Y ds \end{aligned} \tag{D.3}$$

Note that these expressions are valid only for the cut-out boundary. As a result of the free edges of the cut-out, the integrals on the RHS of Eq. D.3 are equal to zero.
Thus, the trial functions must comply with the boundary condition as follows:

$$\begin{aligned} \Phi_{,y} &= 0 \qquad \text{At the hole boundary} \\ \Phi_{,x} &= 0 \qquad \text{At the hole boundary} \end{aligned} \tag{D.4}$$

For both conditions, Eq. D.1 and Eq. D.4, no suitable set of trial functions or boundary conditions forcing function was found.

Appendix E

Effect of the Cut-Out Residual Thickness

In this Appendix, the sensitivity of the in-plane load distribution with respect to the residual cut-out thickness is discussed. In Section 5.4.3, a residual thickness of 2% is used as it showed the best agreement with the ABAQUS results. More residual thickness' were investigated and their results will be shown here. All results are obtained for the plate described in Section 5.4.3 with a uniform compressive displacement $\Delta_x = 1$ [mm]. First, the influence on the in-plane load distribution will be shown in a similar manner as used in Section 5.4.3. Afterwards, the influence of these varying load distributions on the buckling values will be shown.

E.1 In-Plane Loading vs. Residual Thickness

For the various residual thickness' as a percentage of the perimeter thickness, $10\%, 5\%, 2\%, 1\%$ and 0.1%, the same results are shown in Figs. E.1 and E.2. As a main observation, when the residual thickness becomes very small the oscillations at the cut-out edge become more severe and show higher frequencies. While the higher residual thickness' show less severe oscillations, they are often not quite capable of capturing the in-plane load distribution very accurately.

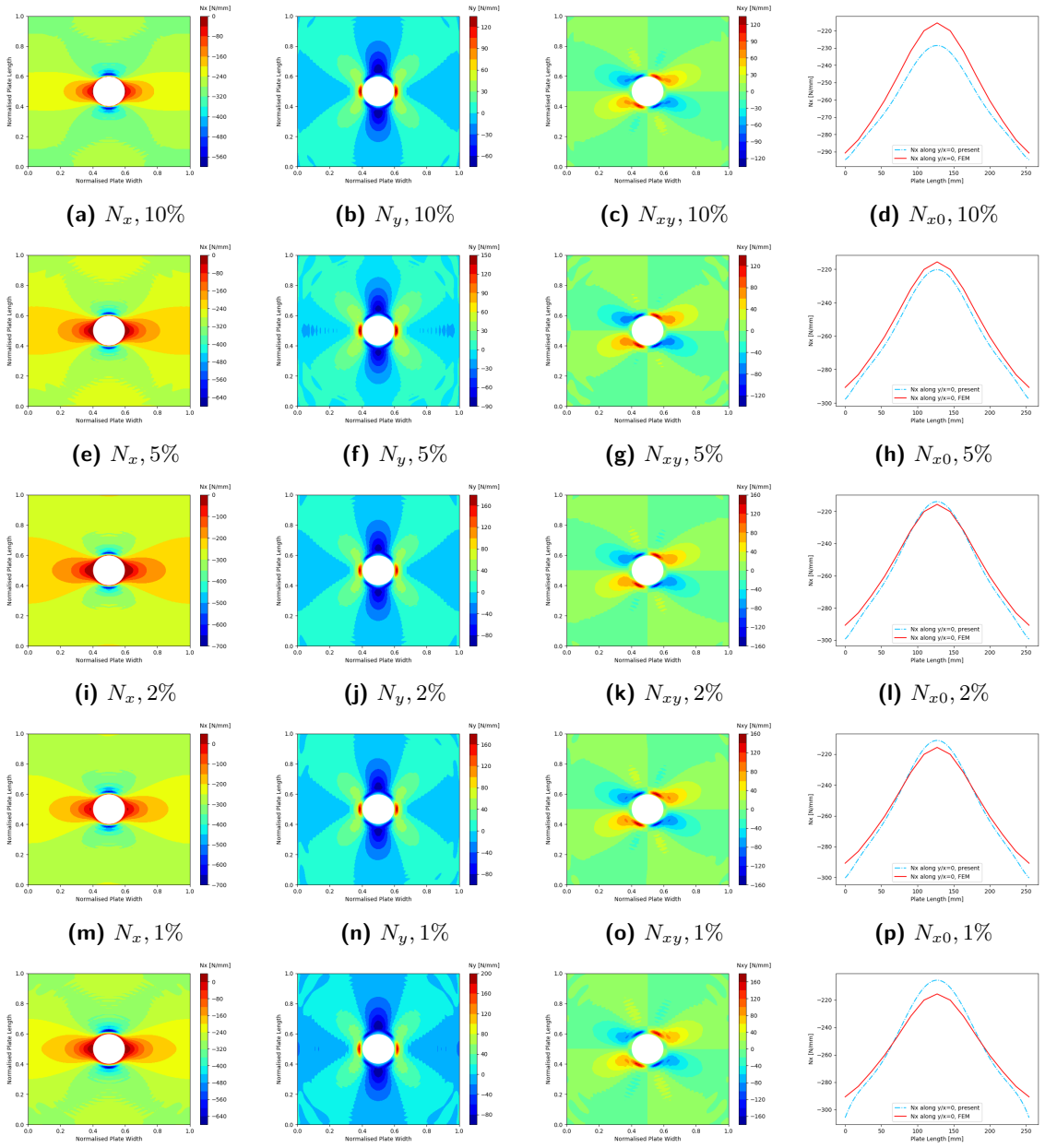

(a) $N_x, 10\%$ **(b)** $N_y, 10\%$ **(c)** $N_{xy}, 10\%$ **(d)** $N_{x0}, 10\%$

(e) $N_x, 5\%$ **(f)** $N_y, 5\%$ **(g)** $N_{xy}, 5\%$ **(h)** $N_{x0}, 5\%$

(i) $N_x, 2\%$ **(j)** $N_y, 2\%$ **(k)** $N_{xy}, 2\%$ **(l)** $N_{x0}, 2\%$

(m) $N_x, 1\%$ **(n)** $N_y, 1\%$ **(o)** $N_{xy}, 1\%$ **(p)** $N_{x0}, 1\%$

(q) $N_x, 0.1\%$ **(r)** $N_y, 0.1\%$ **(s)** $N_{xy}, 0.1\%$ **(t)** $N_{x0}, 0.1\%$

Figure E.1: Overview of load distributions for various residual thickness', indicated as percentage of perimeter plate thickness, $(1/2)$.

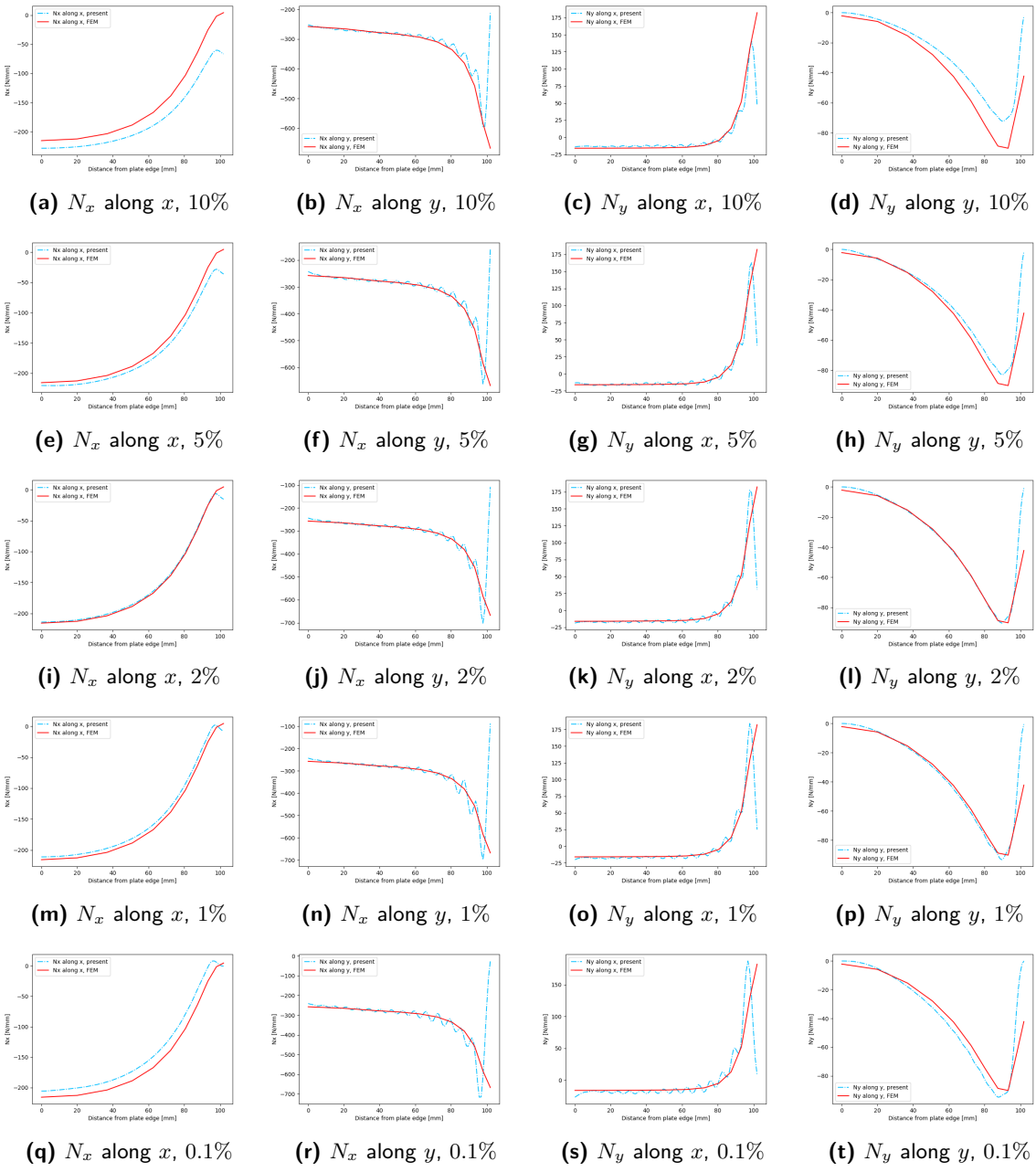

(a) N_x along x, 10% **(b)** N_x along y, 10% **(c)** N_y along x, 10% **(d)** N_y along y, 10%

(e) N_x along x, 5% **(f)** N_x along y, 5% **(g)** N_y along x, 5% **(h)** N_y along y, 5%

(i) N_x along x, 2% **(j)** N_x along y, 2% **(k)** N_y along x, 2% **(l)** N_y along y, 2%

(m) N_x along x, 1% **(n)** N_x along y, 1% **(o)** N_y along x, 1% **(p)** N_y along y, 1%

(q) N_x along x, 0.1% **(r)** N_x along y, 0.1% **(s)** N_y along x, 0.1% **(t)** N_y along y, 0.1%

Figure E.2: Overview of load distributions for various residual thickness', indicated as percentage of perimeter plate thickness, $(2/2)$.

E.2 Buckling Values vs. Residual Thickness

The various in-plane load distributions for the different residual thickness' are used to determine the buckling eigenvalues to determine the influence of the distribution. The buckling eigenvalues for the various in-plane distributions are shown in Table E.1.

Table E.1: Eigenvalues for various in-plane distributions, calculated with varying residual thickness'.

Mode no.	Residual Thickness					ABAQUS
	10%	5%	2%	1%	0.1%	
1	0.01383	0.01421	0.01448	0.01467	0.01494	0.01427
2	0.02635	0.02655	0.02676	0.02687	0.02727	0.02630
3	0.04148	0.04243	0.04318	0.04352	0.04428	0.04302
4	0.05713	0.05721	0.05729	0.05733	0.05753	0.05742
5	0.06218	0.06181	0.06156	0.06139	0.06136	0.06098

According to Table E.1, some thickness' yield closer buckling values than those obtained for the residual thickness taken as 2% in this thesis. The decision to take this value of 2% is based on the in-plane loads distribution agreement, and it is thought that these minor differences in the buckling agreement are due to the fluctuations around the cut-out region of the trigonometric functions.

References

[1] Christos Kassapoglou. *Design and Analysis of Composite Structures*. John Wiley & Sons, 2010. ISBN 9780470972632. doi: 10.1002/9780470972700.

[2] S. B. Biggers and S. Srinivasan. Compression Buckling Response of Tailored Rectangular Composite Plates. *AIAA Journal*, 1993. ISSN 00011452. doi: 10.2514/3.61543.

[3] Zafer Gürdal and Reynaldo Olmedo. In-plane response of laminates with spatially varying fiber orientations - Variable stiffness concept. *AIAA Journal*, 31(4, April):751–758, 1993. ISSN 0001-1452. doi: 10.2514/3.11613.

[4] Thiago A. Guimaraes, Saullo G. Castro, Domingos A. Rade, and Carlos E. Cesnik. Panel Flutter Analysis and Optimization of Composite Tow Steered Plates. *58th AIAA/ASCE/AHS/ASC Structures, Structural Dynamics, and Materials Conference*, (January), 2017.

[5] Christos Kassapoglou. Composite plates with two concentric layups under compression. *Composites Part A: Applied Science and Manufacturing*, 39(1):104–112, 2008. ISSN 1359835X. doi: 10.1016/j.compositesa.2007.08.024.

[6] Lampros Papadopoulos and Christos Kassapoglou. Shear Buckling of Rectangular Composite Plates with Two Concentric Layups. *Journal of Reinforced Plastics and Composites*, 23(1):5–16, 2004. ISSN 07316844. doi: 10.1177/0731684404028698.

[7] S.S Yau and Chou. Strength of Woven-Fabric Composites with Drilled and Molded Holes. *Composite Materials: Testing and Design*, 8:423–437, 1988.

[8] M. W. Hyer and H. H. Lee. The use of curvilinear fiber format to improve buckling resistance of composite plates with central circular holes. *Composite Structures*, 18(3): 239–261, 1991. ISSN 02638223. doi: 10.1016/0263-8223(91)90035-W.

[9] Zhangming Wu, Paul M. Weaver, Gangadharan Raju, Byung Chul Kim, and Byung Chul Kim. Buckling analysis and optimisation of variable angle tow composite plates. *Thin-Walled Structures*, 2012. ISSN 02638231. doi: 10.1016/j.tws.2012.07.008.

[10] Daniël M.J. Peeters, François-Xavier Irisarri, Chris Groenendijk, and Roman Růžek. Optimal design , manufacturing and testing of non-conventional laminates. *Composite Structures*, 210(November 2018):29–40, 2018. ISSN 02638223. doi: 10.1016/j.compstruct.2018.10.062.

[11] B. F.Tatting and Z. Guerdal. Design and Manufacture of Elastically Tailored Tow Placed Plates. *Nasa archive*, (August), 2002.

[12] Saullo G. P. Castro, Maurício V. Donadon, and Thiago A. M. Guimarães. ES-PIM applied to buckling of variable angle tow laminates. *Composite Structures*, Manuscript, 2018.

[13] Boeing aero magazine, issue qtr 04, 2006. URL http://www.boeing.com/commercial/aeromagazine/articles. Accessed on 20/10/2018.

[14] A. W. Leissa and A. F. Martin. Vibration and buckling of rectangular composite plates with variable fiber spacing. *Composite Structures*, 1990. ISSN 02638223. doi: 10.1016/0263-8223(90)90014-6.

[15] Hugo Borges de Quadros and José Antonio Hernandes. A lagrange parametrization for the design of variable stiffness laminates. *Structural and Multidisciplinary Optimization*, 58(1):129–137, 2018. ISSN 16151488.

[16] Shahriar Setoodeh, Mostafa M. Abdalla, and Zafer Gürdal. Design of variable-stiffness laminates using lamination parameters. *Composites Part B: Engineering*, 2006. ISSN 13598368. doi: 10.1016/j.compositesb.2005.12.001.

[17] Shahriar Setoodeh, Adriana Blom, Mostafa Abdalla, and Zafer Gürdal. Generating Curvilinear Fiber Paths from Lamination Parameters Distribution. In *47th AIAA/ASME/ASCE/AHS/ASC Structures, Structural Dynamics, and Materials Conference
 14th AIAA/ASME/AHS Adaptive Structures Conference
 7th*, 2006. ISBN 978-1-62410-040-6. doi: 10.2514/6.2006-1875.

[18] A. Khani, S. T. Ijsselmuiden, M. M. Abdalla, and Z. Gürdal. Design of variable stiffness panels for maximum strength using lamination parameters. *Composites Part B: Engineering*, 42(3):546–552, 2011. ISSN 13598368. doi: 10.1016/j.compositesb.2010.11.005.

[19] A. Alhajahmad, M. M. Abdalla, and Z. Gürdal. *Design Tailoring for Pressure Pillowing Using Tow-Placed Steered Fibers*. PhD thesis, 2008.

[20] A. Khani, M. M. Abdalla, Z. Gürdal, J. Sinke, A. Buitenhuis, and M. J.L. Van Tooren. Design, manufacturing and testing of a fibre steered panel with a large cut-out. *Composite Structures*, 180:821–830, 2017. ISSN 02638223. doi: 10.1016/j.compstruct.2017.07.086.

[21] S. G. Lekhnitskiy. Anisotropic Plates. *Gordon and Breach Science*, page 477, 1969. doi: 0677206704.

[22] M. W. Hyer and R. F. Charette. Use of curvilinear fiber format in composite structure design. *AIAA journal*, 29(6):1011–1015, 1991. ISSN 00011452. doi: 10.2514/3.10697.

[23] T H G Megson. *Aircraft Structures for Engineering Students*. Elsevier, 2007. ISBN 9780750667395. doi: http://dx.doi.org/10.1016/B978-0-08-096905-3.00065-6.

[24] C. S. Huang, A. W. Leissa, and R. S. Li. Accurate vibration analysis of thick, cracked rectangular plates. *Journal of Sound and Vibration*, 330(9):2079–2093, 2011. ISSN 0022460X.

[25] A. Milazzo, I. Benedetti, and V. Gulizzi. An extended Ritz formulation for buckling and post-buckling analysis of cracked multilayered plates. *Composite Structures*, 201(June): 980–994, 2018. ISSN 02638223. doi: 10.1016/j.compstruct.2018.06.026.

[26] K. T. Shivaram. Gauss Legendre quadrature over a unit circle. *International Journal of Engineering and Technical Research*, 2(9, September), 2013.

[27] Adriana W. Blom, Patrick B. Stickler, and Zafer Gürdal. Optimization of a composite cylinder under bending by tailoring stiffness properties in circumferential direction. *Composites Part B: Engineering*, 41(2):157–165, 2010. ISSN 13598368. doi: 10.1016/j.compositesb.2009.10.004.